EXPLORING THE INFLUENCE OF A THREE-BODY INTERACTION ADDED TO THE GRAVITATIONAL POTENTIAL FUNCTION IN THE CIRCULAR RESTRICTED THREE-BODY PROBLEM: A NUMERICAL FREQUENCY ANALYSIS

A Thesis

Submitted to the Faculty

of

Purdue University

by

Natasha Bosanac

In Partial Fulfillment of the

Requirements for the Degree

of

Master of Science in Aeronautics and Astronautics

December 2012

Purdue University

West Lafayette, Indiana

ACKNOWLEDGMENTS

First and foremost, I would like to express my gratitude towards my family: Mum, Dad and Ben. I appreciate your endless support; even after my decision to continue my education on the other side of the world. Mum, I cannot express how grateful I am for everything that you have done for me, and everything that you have sacrificed. None of my achievements thus far would have been possible without your patience, encouragement and support.

Next, I have an incredible appreciation for my advisor, Professor Kathleen C. Howell. I cannot imagine a more perfect way to begin my academic career than by working with you. As your student, you continually challenge and support me; and as your teaching assistant, you have taught me so much about education. Furthermore, I am beyond grateful for the opportunity to continue learning from you: you never cease to inspire me.

I would also like to acknowledge Professor Ephraim Fischbach in the Physics department. Given his experience with many-body forces in nuclear physics, he first presented the idea of studying orbital dynamics under the influence of a three-body interaction to Professor Howell and me. Throughout this entire investigation, he has asked so many intriguing questions and challenged me to approach my research from many different perspectives. I look forward to continuing and extending our collaboration. I also wish to express my thanks to Professor James M. Longuski and Professor Martin J. Corless for serving on my committee.

Past and present members of the research group also deserve recognition. Even though we come from so many different places and backgrounds, the collaborative atmosphere within our research group fosters unique and interesting conversations. I am appreciative of your help, support and friendship, and I look forward to continuing to work with all of you.

Finally, I would like to thank the Computational Science and Engineering program for providing me with a Lynn Fellowship and the Department of Aeronautics and Astronautics for subsequently supporting me with a teaching assistantship. This research would not have been possible without either of their generosity, and I am incredibly grateful to have received financial support.

TABLE OF CONTENTS

LIST OF FIGURES

Figure Page

Figure Page

Figure Page

ABSTRACT

Bosanac, Natasha M.S.A.A, Purdue University, December 2012. Exploring the Influence of a Three-Body Interaction Added to the Gravitational Potential Function in the Circular Restricted Three-Body Problem: A Numerical Frequency Analysis. Major Professor: Kathleen C. Howell.

Many binary star systems (e.g., pulsar-white dwarf) are known to possess significantly smaller companions, such as an exoplanet, in large orbits about the binary. Given that binary star systems exist far from the Earth, the interactions comprising their dynamical environment are unknown. Fundamentally, the motion of the exoplanet may be modeled using pairwise point-mass gravitational contributions from each of the two stars, assumed to possess similar masses. In this investigation, however, a three-body interaction is also considered. This extra force contribution is selected to depend inversely upon the product of the distances between the three bodies. The resulting model is constructed to reduce to the well-known circular restricted three-body problem as the three-body interaction is scaled to zero. A numerical frequency analysis is employed to examine the properties and prevalence of retrograde periodic and quasi-periodic orbits in the exterior region in the circular restricted three-body problem for a large mass ratio. Using these results as a baseline, a similar analysis is completed for various constants scaling the three-body interaction. The influence of this additional contribution is explored using the computed fundamental frequencies, which reflect changes in the underlying ordered dynamics in the vicinity of the binary. Poincaré maps are employed to confirm and explore the results of the frequency analysis. The results from this preliminary investigation suggest that the dynamics of an exoplanet in a large orbit about a binary star system are significantly altered by the inclusion of a three-body interaction.

1. INTRODUCTION

Consider a binary star system (e.g., pulsar-white dwarf, pulsar-pulsar) with a significantly smaller companion, such as an exoplanet, in orbit about the binary. Given the lack of experimental data gathered within the vicinity of such a binary, it is possible that the gravitational field within this system may not be accurately modeled by purely pairwise gravitational forces. In this investigation, the presence of an additional three-body interaction is considered. Many-body forces are not an entirely new concept; in fact, the importance of three-body interactions in accurately modeling force fields on the atomic scale is well established within nuclear physics [1]. On a considerably larger scale, the motion of a small body orbiting a binary star system serves as a new and interesting application for exploring the characteristics of a three-body interaction.

Since binary star systems are located many light-years from the Earth, the characteristics of the binary, and any smaller companions, are determined from pulsar timing measurements. A pulsar in complete isolation would rotate about its spin axis with a constant angular velocity, emitting pulses of radiation at a constant rate. However, in the presence of additional bodies, the pulsar appears to rotate with a nonconstant angular velocity. The resulting Doppler shift in the timing of the pulses can be approximately fitted to the orbit of the pulsar, which can be correlated to the masses and orbits of any companions. These orbits are governed by a dynamical environment that may be modeled using various interactions, including those due to pairwise point-mass gravity, gravitational wave radiation, and magnetic fields.

Assuming that the exoplanet possesses a negligible mass in comparison to the binary, the complexity of the dynamical model may be reduced by considering only the pairwise, point-mass gravitational contributions from the two stars. This gravitational model is commonly labeled the restricted three-body problem. In this configu-

ration, the two stars comprising the binary are assumed to possess similar mass; while a large mass ratio reflects the physical configuration of many binary star systems, it is significantly larger than the mass ratios of objects considered within the solar system. Each star is assumed to follow conical paths about their barycenter. Further simplification of the problem results from an additional assumption that these conics are sufficiently close to circular that they are modeled with zero eccentricity. Using this model as a foundation, the effect of three-body interactions may be examined by comparing the motion of the exoplanet with and without this additional contribution.

The dynamical model for the motion of the exoplanet is derived based upon the circular restricted three-body problem (CR3BP), but extended to incorporate an additional term in the potential function. The subsequent set of differential equations comprises the framework for the modified circular restricted three-body problem (MCR3BP). While the notation and three-body configuration is consistent between the two systems, this new model accommodates the presence of a three-body interaction in addition to the inverse-square pairwise gravitational interactions. This additional contribution is assumed to depend inversely on the product of the distances between each body: the closer the bodies, the stronger the three-body interaction.

Given that many discovered binary star systems are postulated to possess one or more exoplanets in large orbits about both stars, this investigation of three-body interactions is currently limited to the study of trajectories far from the binary. For an exoplanet to be bound to the vicinity of the binary over a long period of time, it likely exhibits ordered motion that is not sensitive to perturbations. These orbits can be decomposed into the sum of multiple sinusoidal waves that are characterized by their fundamental frequencies. Monitoring the influence of a three-body interaction on any fundamental frequencies may represent the resulting changes to the possible behavior of an exoplanet. Thus, frequency analysis is employed to investigate the effect of the additional three-body contribution to the dynamical environment in the vicinity of a binary.

1.1 Previous Contributions

1.1.1 Many-Body Forces

The modeling of a three-body interaction within the context of orbital dynamics is inspired by analogous electromagnetic interactions in quantum physics. In 1948, Richard P. Feynman introduced Feynman diagrams. In nuclear physics, these graphical representations have been used to illustrate the possible combinations of interactions within a system of multiple particles [2]. Each configuration can be analyzed to recover certain properties of the system, including the potential function. For a sample system of two electrically-charged particles, Coulomb's inverse square law is recovered by modeling pairwise exchanges of photons [3].

If more than two particles are considered, many-body interactions may also be postulated using Feynman diagrams. The resulting hypotheses have lead to the explanation of physically observable phenemona in nuclear physics. One example is the inconsistency between the observed half life of Carbon-14 and the half-life computed using a two-body force model [4]. In this scenario, three-body forces contribute significantly to an otherwise underestimated quantity.

Analogously, the gravitational interactions in an orbital dynamics problem may also be modeled using Feynman diagrams. Representation of the possible interactions between three masses, such as those within a binary star system with a smaller companion, leads to the proposal of three-body interactions added to the inverse-square gravity force proposed by Sir Isaac Newton in 1687 in *Philosophiae Naturalis Principia Mathematica*. Using an appropriately constructed Feynman diagram, this additional potential contribution may be initially modeled as proportional to the product of the distances between the three bodies.

1.1.2 Dynamical Model

The MCR3BP is formulated to reduce to the CR3BP, with a decreasing magnitude of the three-body interaction, due to the extensive set of tools and techniques that have been developed to determine and visualize a solution for an assumed massless body. The configuration for the restricted three-body problem was first introduced by Leonhard Euler in 1772 in his second lunar theory [5]. In this work, Euler formulated the model with respect to a rotating coordinate system and demonstrated the existence of the collinear equilibrium points. During the same year, Joseph Louis Lagrange determined the location of the equilateral equilibrium points. Later, in 1836, Carl Gustav Jacob Jacobi contributed to the development of the CR3BP through the proposal of a single integral of the motion, labeled the Jacobi constant [6]. George Hill then used this knowledge in 1878 to prove the existence of the zero velocity curves that bound regions of allowable motion for the small, third body [7].

Significant contributions to the identification and visualization of particular solutions in the CR3BP originated with Henri Poincaré who conceived the basic foundational concept at the root of the Poincaré map, also labeled the first return map, in 1881 [5]. This invaluable tool yields a lower-dimensional representation of the dynamics in a continuous-time system. Using this work as a foundation, Poincaré explored the influence of particular solutions (including periodic and quasi-periodic orbits) on the dynamics in their vicinity, also identifying the presence of chaotic motion in the CR3BP. He published his preliminary findings in 1899 in *Les Méthodes Nouvelles de la Mécanique Céleste* [8]. The contributions of Poincaré have served as a framework for the development of the tools used today in dynamical systems theory. In fact, KAM theory was developed through the combined research of Andrey Kolmogorov, Vladimir Arnold and Jurgen Moser, and is based on the contributions of Poincaré [9] [10] [11]. KAM theory focuses on the persistence of quasi-periodic orbits, which can be described by their underlying fundamental frequencies.

1.1.3 Frequency Analysis

Frequency analysis involves a determination of the underlying frequencies of the solutions in a dynamical system. The resulting representation of a solution in the frequency domain can be used to obtain its properties. As implemented in this investigation, the frequency analysis process depends upon the Discrete Fourier Transform, named for Jean Baptiste Joseph Fourier. In his work in 1807, Fourier first proposed the representation of a periodic function as a trigonometric series [12]. Using this concept as a basis, various Fast Fourier Transform (FFT) algorithms have been developed to decompose a function into a set of sinusoidal waves. Carl Friedrich Gauss is now credited with the development of the first FFT algorithm in 1805 to describe trajectories in the problem of orbital motion. However, the most well-known algorithm was proposed by James William Cooley and John Wilder Tukey in 1965 [13].

In 1990, Jacques Laskar applied the process of frequency decomposition to the study of trajectories in a Hamiltonian system. Building upon the concepts developed by Fourier, Laskar constructed an algorithm called the Numerical Analysis of the Fundamental Frequency. Using this algorithm, Laskar decomposed quasi-periodic orbits into their fundamental frequencies with an accuracy higher than that achieved by the FFT [14]. Later, many researchers in celestial mechanics and astrophysics used this algorithm to study the motion of a body governed by a variety of potential fields [15] [16] [17]. In this investigation, Laskar's methodology is employed to monitor the frequencies of periodic and quasi-periodic motions under the influence of a three-body interaction.

1.2 Thesis Overview

This study is organized as follows:

- Chapter 2: The dynamical model is formulated to resemble the circular restricted three-body problem, augmented by a three-body interaction. Following derivation of the equations of motion, an integral of motion is identified. Par-

ticular solutions, in the form of equilibrium points and zero velocity curves, are explored and developed within the context of the circular restricted three-body problem as an indicator of the bounds on the motion.

- Chapter 3: Ordered, time-varying trajectories are explored, including periodic orbits and quasi-periodic orbits. The state transition matrix is then introduced and used to determine the stability of periodic orbits. Qualitative changes in the dynamics in the vicinity of a periodic orbit are classified as bifurcations and correlated to changes in the stability across a family of periodic orbits. A differential corrections scheme is also introduced to compute periodic orbits, given an initial guess. A single, periodic solution is then exploited to determine other members of its family using pseudo-arclength continuation.

- Chapter 4: Poincaré maps are employed to reduce the dimension of planar dynamics by transforming a system of continuous-time differential equations into a discrete mapping. To perform this transformation, the concept of a surface of section is introduced. Structures that emerge on a Poincaré map are analyzed, identified and correlated to time-varying trajectories.

- Chapter 5: Decomposition of a periodic or quasi-periodic function into its underlying frequencies is developed and explored. A derivation of the Discrete Fourier Transform is presented, along with aspects related to its numerical implementation. To reduce the error incurred during frequency decomposition, a numerical frequency refinement technique is explored. This technique, based on a differential corrections scheme, is applied to the frequency decomposition of trajectories in the circular restricted three-body problem. Representations of the resulting frequency information are developed and correlated to features that are visible on a Poincaré map.

- Chapter 6: The tools developed in the context of dynamical systems theory and frequency analysis are applied to the investigation of the influence of the

three-body potential term. The equilibrium points, for various values of the three-body potential coefficient, are computed and located. At the energy levels corresponding to these points, the zero velocity curves are plotted and compared with the CR3BP. Periodic and quasi-periodic solutions are then decomposed into their fundamental frequencies and represented over various energy levels. This analysis is used to determine the form and prevalence of orbits within the phase space.

- Chapter 7: A summary of the results of this investigation is presented, followed by recommendations for extending the analysis of the influence of a three-body potential term on the dynamics in the circular restricted three-body problem.

2. DYNAMICAL MODEL

The motivating problem for this investigation is a binary star system (e.g., pulsar-white dwarf, pulsar-pulsar) with a significantly smaller companion, such as an exo-planet, in orbit about the binary. This configuration is initially modeled in terms of the circular restricted three-body problem, a well-known formulation within the astrodynamics community. In this model, the two large bodies, assumed to be point masses, move in circular orbits about their barycenter. By Newton's law of universal gravitation, each of the point masses attracts the small companion with a force that is inversely proportional to the distance between them. The sum of these gravitational forces acts on the small companion as it orbits the binary. Many numerical techniques have been developed by past researchers to identify, visualize and characterize the behavior of this small companion body within the context of the CR3BP.

The model used here, henceforth labeled the modified circular restricted three-body problem, is formulated similar to the traditional CR3BP. While the notation and configuration are consistent between the two systems, the MCR3BP incorporates the presence of three-body interactions in addition to pairwise gravitational interactions. This extra contribution is assumed to depend inversely on the product of the distances between the three bodies: the closer the bodies, the stronger the three-body interaction. When the three-body interaction is negated, this model reduces to the CR3BP. The form of the augmented potential in the MCR3BP influences the equations of motion, yielding a model that still admits an integral of the motion. Particular solutions, in the form of equilibrium points and zero velocity curves, are also available in this augmented model and establish bounds on the motion.

2.1 Definition of Potential Function

Figure 2.1 depicts the configuration of three bodies in an inertial reference frame, $\hat{X}\hat{Y}\hat{Z}$, with a fixed origin at point O. By convention, the body of interest, P_3, moves in the vicinity of the larger and smaller primaries, P_1 and P_2, each body P_i possessing a mass M_i. The position vector locating P_3 with respect to the origin is denoted $\bar{R}_3 = X\hat{X} + Y\hat{Y} + Z\hat{Z}$, while P_1 and P_2 are, respectively, located using the vectors $\bar{R}_1 = X_1\hat{X} + Y_1\hat{Y} + Z_1\hat{Z}$ and $\bar{R}_2 = X_2\hat{X} + Y_2\hat{Y} + Z_2\hat{Z}$. Also appearing in Figure 2.1 are the relative position vectors $\bar{R}_{ij} = (X_j - X_i)\hat{X} + (Y_j - Y_i)\hat{Y} + (Z_j - Z_i)\hat{Z}$ which locate body P_j with respect to body P_i. In this investigation, an overbar identifies a vector, while the notation $\hat{(.)}$ represents a unit vector.

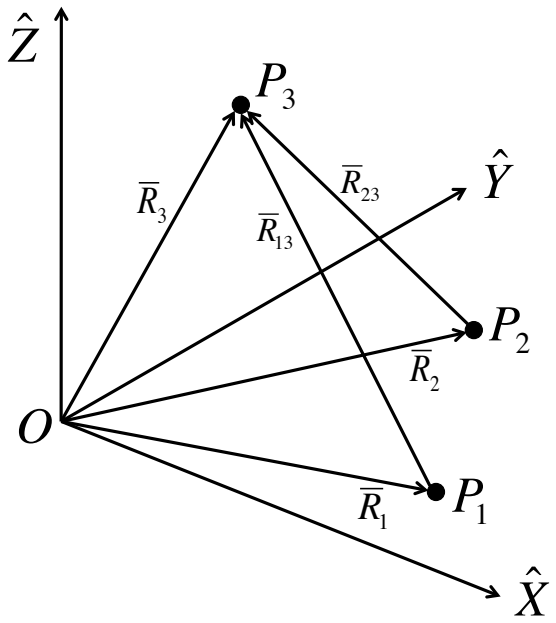

Figure 2.1. Definition of the inertial coordinate frame and the position vectors locating each of the bodies in the MCR3BP.

Given this system configuration, derivation of the differential equations governing the motion of P_3 in the MCR3BP requires a form of the potential function. The scalar potential of P_3, per unit mass, is assumed to consist of the following terms:

$$U_3 = \underbrace{\frac{\tilde{G}\tilde{M}_1}{\tilde{R}_{13}} + \frac{\tilde{G}\tilde{M}_2}{\tilde{R}_{23}}}_{\text{pairwise potential}} + \underbrace{\frac{\tilde{K}}{\tilde{R}_{12}\tilde{R}_{13}\tilde{R}_{23}}}_{\text{three-body potential}} \tag{2.1}$$

where the tilde denotes dimensional quantities, $\tilde{G}$ is the universal gravitational constant, and $\tilde{K}$ is a constant that scales the contribution of the three-body interactions to the resultant potential. Since the magnitude and sign of this constant is unknown, it is assumed that $\tilde{K}$ can be selected as either positive, negative or zero with the associated units $[length]^5[time]^{-2}$. When the value of the constant $\tilde{K}$ is equal to zero, the potential of the MCR3BP reduces to the CR3BP potential.

2.2 Equations of Motion Relative to an Inertial Frame

From the definition of the potential function in equation (2.1), the equations of motion for P_3 are derived relative to an inertial observer. A potential function depending solely upon position variables is differentiated to determine the force per unit mass, $\bar{F}_i$, acting on body P_i:

$$\bar{F}_i = \bar{\nabla}_i U_i = \bar{R}_i'' \tag{2.2}$$

where U_i reflects the terms in the potential function that are functions of the coordinates locating body P_i. Then, $\bar{\nabla}_i(.)$ is a vector operator, and derivatives with respect to an inertial observer are denoted with a prime, $(.)'$. Although P_3 is the body of interest, this relationship applies to any of the three bodies. Assuming that P_3 is located at the inertial position $(\tilde{X}, \tilde{Y}, \tilde{Z})$ as indicated in Figure 2.1, the partial

derivatives of the potential function U_3 yield the force components in each of the inertial directions:

$$\begin{aligned}\frac{\partial U_3}{\partial \tilde{X}} &= \frac{\partial}{\partial \tilde{X}}\left(\frac{\tilde{G}\tilde{M}_1}{\tilde{R}_{13}}+\frac{\tilde{G}\tilde{M}_2}{\tilde{R}_{23}}+\frac{\tilde{K}}{\tilde{R}_{12}\tilde{R}_{13}\tilde{R}_{23}}\right)\\ &= -\frac{\tilde{G}\tilde{M}_1(\tilde{X}-\tilde{X}_1)}{\tilde{R}_{13}^3}-\frac{\tilde{G}\tilde{M}_2(\tilde{X}-\tilde{X}_2)}{\tilde{R}_{23}^3}-\tilde{K}\left[\frac{\tilde{X}-\tilde{X}_1}{\tilde{R}_{13}^3\tilde{R}_{23}}+\frac{\tilde{X}-\tilde{X}_2}{\tilde{R}_{13}\tilde{R}_{23}^3}\right] \quad (2.3)\end{aligned}$$

$$\begin{aligned}\frac{\partial U_3}{\partial \tilde{Y}} &= \frac{\partial}{\partial \tilde{Y}}\left(\frac{\tilde{G}\tilde{M}_1}{\tilde{R}_{13}}+\frac{\tilde{G}\tilde{M}_2}{\tilde{R}_{23}}+\frac{\tilde{K}}{\tilde{R}_{12}\tilde{R}_{13}\tilde{R}_{23}}\right)\\ &= -\frac{\tilde{G}\tilde{M}_1(\tilde{Y}-\tilde{Y}_1)}{\tilde{R}_{13}^3}-\frac{\tilde{G}\tilde{M}_2(\tilde{Y}-\tilde{Y}_2)}{\tilde{R}_{23}^3}-\tilde{K}\left[\frac{\tilde{Y}-\tilde{Y}_1}{\tilde{R}_{13}^3\tilde{R}_{23}}+\frac{\tilde{Y}-\tilde{Y}_2}{\tilde{R}_{13}\tilde{R}_{23}^3}\right] \quad (2.4)\end{aligned}$$

$$\begin{aligned}\frac{\partial U_3}{\partial \tilde{Z}} &= \frac{\partial}{\partial \tilde{Z}}\left(\frac{\tilde{G}\tilde{M}_1}{\tilde{R}_{13}}+\frac{\tilde{G}\tilde{M}_2}{\tilde{R}_{23}}+\frac{\tilde{K}}{\tilde{R}_{12}\tilde{R}_{13}\tilde{R}_{23}}\right)\\ &= -\frac{\tilde{G}\tilde{M}_1(\tilde{Z}-\tilde{Z}_1)}{\tilde{R}_{13}^3}-\frac{\tilde{G}\tilde{M}_2(\tilde{Z}-\tilde{Z}_2)}{\tilde{R}_{23}^3}-\tilde{K}\left[\frac{\tilde{Z}-\tilde{Z}_1}{\tilde{R}_{13}^3\tilde{R}_{23}}+\frac{\tilde{Z}-\tilde{Z}_2}{\tilde{R}_{13}\tilde{R}_{23}^3}\right] \quad (2.5)\end{aligned}$$

where $\tilde{R}_{j3}=\sqrt{(\tilde{X}-\tilde{X}_j)^2+(\tilde{Y}-\tilde{Y}_j)^2+(\tilde{Z}-\tilde{Z}_j)^2}$ is the distance between P_j and P_3, for $j=1,2$. Since these partial derivatives are equal to the forces acting in each of the inertial directions, differentiating the pairwise gravitational potential terms recovers the well-known inverse-square gravitational force. The additional force components in equations (2.3)-(2.5) comprise the conservative force acting on P_3 due to the three-body interactions within the system. The equations of motion for P_3 with respect to an inertially fixed observer are subsequently obtained by inserting the gravitational and three-body force components into equation (2.2):

$$\tilde{X}'' = -\frac{\tilde{G}\tilde{M}_1(\tilde{X}-\tilde{X}_1)}{\tilde{R}_{13}^3}-\frac{\tilde{G}\tilde{M}_2(\tilde{X}-\tilde{X}_2)}{\tilde{R}_{23}^3}-\tilde{K}\left[\frac{\tilde{X}-\tilde{X}_1}{\tilde{R}_{13}^3\tilde{R}_{23}}+\frac{\tilde{X}-\tilde{X}_2}{\tilde{R}_{13}\tilde{R}_{23}^3}\right] \quad (2.6)$$

$$\tilde{Y}'' = -\frac{\tilde{G}\tilde{M}_1(\tilde{Y}-\tilde{Y}_1)}{\tilde{R}_{13}^3}-\frac{\tilde{G}\tilde{M}_2(\tilde{Y}-\tilde{Y}_2)}{\tilde{R}_{23}^3}-\tilde{K}\left[\frac{\tilde{Y}-\tilde{Y}_1}{\tilde{R}_{13}^3\tilde{R}_{23}}+\frac{\tilde{Y}-\tilde{Y}_2}{\tilde{R}_{13}\tilde{R}_{23}^3}\right] \quad (2.7)$$

$$\tilde{Z}'' = -\frac{\tilde{G}\tilde{M}_1(\tilde{Z}-\tilde{Z}_1)}{\tilde{R}_{13}^3}-\frac{\tilde{G}\tilde{M}_2(\tilde{Z}-\tilde{Z}_2)}{\tilde{R}_{23}^3}-\tilde{K}\left[\frac{\tilde{Z}-\tilde{Z}_1}{\tilde{R}_{13}^3\tilde{R}_{23}}+\frac{\tilde{Z}-\tilde{Z}_2}{\tilde{R}_{13}\tilde{R}_{23}^3}\right] \quad (2.8)$$

Depending on the sign of $\tilde{K}$, the force corresponding to the three-body interaction is either attractive or repulsive.

Determining the position and velocity time histories governing the behavior of P_3 with respect to an inertially fixed point requires the simultaneous solution for the position and velocity of all three bodies. Combining equations (2.6)-(2.8) with similar equations of motion for P_1 and P_2 results in 18 scalar first-order differential equations. An analytical solution, therefore, requires 18 constants. However, only 10 integrals of the motion are known to exist: six from the conservation of linear momentum, three from the conservation of angular momentum and one from the conservation of energy. Reformulating the problem to model the relative motion of P_3 with respect to a primary reduces the number of first-order scalar differential equations to 12. However, the number of integrals remains insufficient.

2.3 Simplifying Assumptions and Nondimensionalization

In the absence of an analytical solution, the introduction of simplifying assumptions and a reformulation of the equations of motion offers a limited yet useful insight into the behavior of P_3. First, the third body is assumed to have infinitesimal mass in comparison to P_1 and P_2. Such an assumption is applicable to many binary pulsar systems that may include a smaller additional companion, such as an exoplanet. Incorporating this assumption into the MCR3BP results in a center of mass for the three-body system that is located along the line between the two massive primaries. The system barycenter, an inertially fixed location, is conveniently selected to be the origin of the $\hat{X}\hat{Y}\hat{Z}$ coordinate frame. Since the infinitesimal third body does not influence the motion of P_1 and P_2, the primaries trace out closed conics about their mutual barycenter. For an arbitrary conic, the distance between P_1 and P_2 is time-dependent, resulting in complexities in visualizing the motion of P_3 with respect to the primaries. To eliminate the pulsation of the primaries and the time-dependence of their rotation rate, P_1 and P_2 are assumed to

move on circular orbits in this preliminary investigation. The locations of P_1 and P_2 are, therefore, known for all time: $(\tilde{X}_1, \tilde{Y}_1, \tilde{Z}_1) = (-\mu\cos(t), -\mu\sin(t), 0)$ and $(\tilde{X}_2, \tilde{Y}_2, \tilde{Z}_2) = ((1-\mu)\cos(t), (1-\mu)\sin(t), 0)$.

To extend the analysis to systems of various relative mass ratios, it is convenient to nondimensionalize the system parameters using appropriately defined characteristic quantities. Distances are nondimensionalized using the distance between the two primaries as a reference, denoted l^*:

$$l^* = \tilde{D}_1 + \tilde{D}_2$$

where $\tilde{D}_i$ is the distance from the system barycenter to each of the two primaries, respectively. Since the two primaries are assumed to follow circular orbits, the nondimensional distance between P_1 and P_2 is constant at a value of 1. The characteristic mass quantity, m^*, is the sum of the masses of the primaries, while time is nondimensionalized with t^* such that the mean motion of the primaries is equal to 1. These characteristic quantities are evaluated as:

$$m^* = \tilde{M}_1 + \tilde{M}_2$$

$$t^* = \left(\frac{\tilde{D}_1 + \tilde{D}_2}{\tilde{G}(\tilde{M}_1 + \tilde{M}_2)}\right)^{1/2}$$

The characteristic mass quantity yields nondimensional mass values for P_1 and P_2 equal to $(1-\mu)$ and μ, respectively, where μ is defined as:

$$\mu = \frac{\tilde{M}_2}{m^*}$$

Throughout this investigation, the value for μ remains fixed and is equal to 0.3. The value $\mu = 0.3$ is a large mass ratio that has not been explored extensively from the perspective of the CR3BP. It is, however, representative of the order of magnitude corresponding to many binary pulsar systems, such as the pulsar-white dwarf binary PSR B1620-26 that is orbited by an exoplanet [18] [19]. Rewriting the potential of P_3 in terms of nondimensional units, the form of equation (2.1) simplifies to:

$$U_3 = \frac{1-\mu}{R_{13}} + \frac{\mu}{R_{23}} + \frac{k}{R_{13}R_{23}}$$

Similarly, the equations of motion, equations (2.6)-(2.8), in nondimensional variables are equal to:

$$\begin{aligned} X'' &= -\frac{(1-\mu)(X+\mu cos(t))}{R_{13}^3} - \frac{\mu(X-(1-\mu)cos(t))}{R_{23}^3} \\ &\quad -k\left[\frac{X+\mu cos(t)}{R_{13}^3 R_{23}} + \frac{X-(1-\mu)cos(t)}{R_{13}R_{23}^3}\right] \end{aligned} \tag{2.9}$$

$$\begin{aligned} Y'' &= -\frac{(1-\mu)(Y+\mu sin(t))}{R_{13}^3} - \frac{\mu(Y-(1-\mu)sin(t))}{R_{23}^3} \\ &\quad -k\left[\frac{Y+\mu sin(t)}{R_{13}^3 R_{23}} + \frac{Y-(1-\mu)sin(t)}{R_{13}R_{23}^3}\right] \end{aligned} \tag{2.10}$$

$$Z'' = -\frac{(1-\mu)Z}{R_{13}^3} - \frac{\mu Z}{R_{23}^3} - k\left[\frac{Z}{R_{13}^3 R_{23}} + \frac{Z}{R_{13}R_{23}^3}\right] \tag{2.11}$$

These equations of motion still include time-dependent terms locating P_1 and P_2. Such terms add complexity to the identification of equilibrium and other particular solutions, as well as visualization of trajectories.

2.4 Equations of Motion in a Rotating Frame

The MCR3BP equations of motion are autonomous if a rotating coordinate frame, $\hat{x}\hat{y}\hat{z}$, is introduced. This coordinate frame is defined in Figure 2.2 such that the $\hat{x}$ unit vector is directed from P_1 towards P_2; the $P_1 - P_2$ line rotates at a constant, nondimensional rate of unity about the $+\hat{Z}$ axis. The $\hat{z}$ unit vector is defined in a direction that is normal to the $P_1 - P_2$ orbit plane and parallel to the orbital angular momentum. This right-handed triad is completed by appropriately defining $\hat{y}$ within the binary's plane of motion and perpendicular to $\hat{x}$. In the rotating frame, the location of P_3, (x, y, z), is written in terms of its inertial nondimensional coordinates (X, Y, Z) as:

$$\begin{bmatrix} x \\ y \\ z \end{bmatrix} = \begin{bmatrix} cos(t) & sin(t) & 0 \\ -sin(t) & cos(t) & 0 \\ 0 & 0 & 1 \end{bmatrix} \begin{bmatrix} X \\ Y \\ Z \end{bmatrix}$$

Using this rotation matrix, the fixed locations of the two primaries expressed in terms of the nondimensional rotating coordinates are $(x_1, y_1, z_1) = (-\mu, 0, 0)$ and

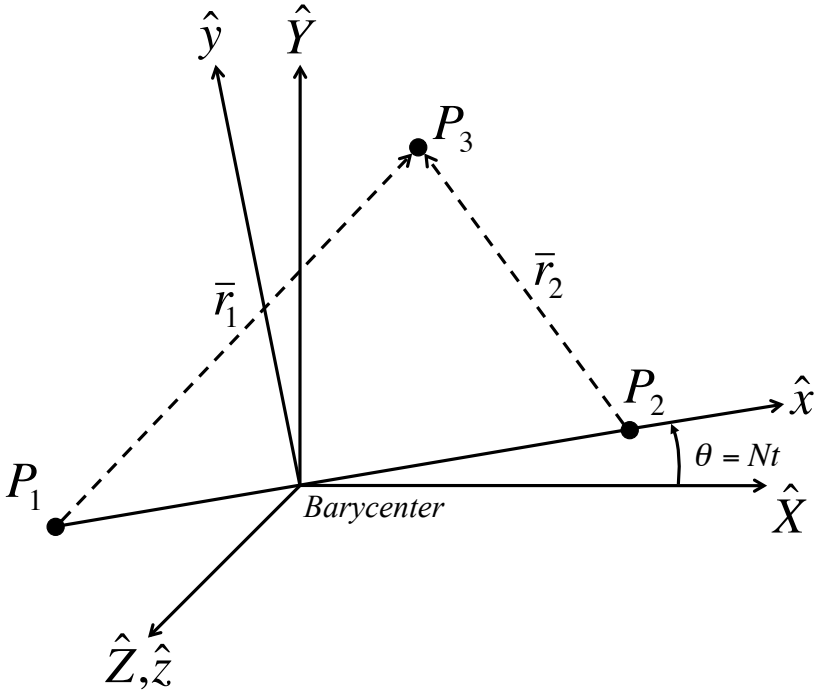

Figure 2.2. Definition of the rotating coordinate frame which rotates with respect to the inertial frame at a nondimensional rate of $N = 1$ about the $\hat{Z}$-axis.

$(x_2, y_2, z_2) = (1 - \mu, 0, 0)$. Lowercase position vectors, $\bar{r}_1 = (x + \mu)\hat{x} + y\hat{y} + z\hat{z}$ and $\bar{r}_2 = (x - 1 + \mu)\hat{x} + y\hat{y} + z\hat{z}$, locate P_3 with respect to the two primaries.

A kinematic expansion is employed to rewrite the acceleration of P_3 in terms of rotating coordinates and shift the view to a rotating observer. Recall that the angular velocity of the rotating frame with respect to the inertial frame is in the $\hat{z}$ direction, with a nondimensional magnitude of unity. With this information, the acceleration is expressed as the second derivative of the position vector, $\bar{r} = x\hat{x} + y\hat{y} + z\hat{z}$, with respect to an inertial observer, and the kinematic expansion yields:

$$\bar{r}'' = (\ddot{x} - 2\dot{y} - x)\hat{x} + (\ddot{y} + 2\dot{x} - y)\hat{y} + \ddot{z}\hat{z}$$

where $(\dot{.})$ represents a time derivative with respect to an observer in the rotating frame. Using this result, the equations of motion, given in equations (2.6)-(2.8), are expressed in terms of rotating coordinates as:

$$\ddot{x} = 2\dot{y} + x - \frac{(1-\mu)(x+\mu)}{r_1^3} - \frac{\mu(x-1+\mu)}{r_2^3} - k\left[\frac{(x-1+\mu)}{r_1 r_2^3} + \frac{(x+\mu)}{r_1^3 r_2}\right] \tag{2.12}$$

$$\ddot{y} = -2\dot{x} + y - \frac{(1-\mu)y}{r_1^3} - \frac{\mu y}{r_2^3} - k\left[\frac{y}{r_1 r_2^3} + \frac{y}{r_1^3 r_2}\right] \tag{2.13}$$

$$\ddot{z} = -\frac{(1-\mu)z}{r_1^3} - \frac{\mu z}{r_2^3} - k\left[\frac{z}{r_1 r_2^3} + \frac{z}{r_1^3 r_2}\right] \tag{2.14}$$

where $r_1 = \sqrt{(x+\mu)^2 + y^2 + z^2}$ and $r_2 = \sqrt{(x-1+\mu)^2 + y^2 + z^2}$ are the nondimensional distances between P_3 and the primaries. No analytical solution to these nonlinear differential equations is available. The three second-order differential equations can be transformed into six first-order differential equations and numerically integrated using initial conditions in the form of six position and velocity states, $(x, y, z, \dot{x}, \dot{y}, \dot{z})$, in terms of the rotating coordinates.

2.5 Integral of the Motion

From conservation of energy, a constant energy integral exists when the equations of motion in the MCR3BP are expressed relative to the rotating frame. The equations of motion, equations (2.12)-(2.14), from Section 2.2, can be written in the form:

$$\ddot{x} - 2\dot{y} = \frac{\partial U^*}{\partial x} \tag{2.15}$$

$$\ddot{y} + 2\dot{x} = \frac{\partial U^*}{\partial y} \tag{2.16}$$

$$\ddot{z} = \frac{\partial U^*}{\partial z} \tag{2.17}$$

where U^* is defined as the pseudopotential. Although U^* is analogous to the potential in Section 2.1, the potential acting on P_3 is now written in terms of rotating coordinates. Solving for the pseudopotential, U^* is evaluated as:

$$U^* = \frac{1}{2}(x^2 + y^2) + \frac{1-\mu}{r_1} + \frac{\mu}{r_2} + \frac{k}{r_1 r_2} \tag{2.18}$$

which is employed to develop the energy integral that corresponds to the equations of motion as formulated in the rotating frame. The dot product of the acceleration and velocity vectors, $(\ddot{x}, \ddot{y}, \ddot{z})$ and $(\dot{x}, \dot{y}, \dot{z})$, after inserting equations (2.15)-(2.17), produces the following relationship:

$$\dot{x}\ddot{x} + \dot{y}\ddot{y} + \dot{z}\ddot{z} = \frac{\partial U^*}{\partial x}\dot{x} + \frac{\partial U^*}{\partial y}\dot{y} + \frac{\partial U^*}{\partial z}\dot{z}$$

which, when integrated, is equivalent to:

$$\frac{1}{2}v^2 = \int dU^* - \frac{dU^*}{dt}$$

where $v^2 = \dot{x}^2 + \dot{y}^2 + \dot{z}^2$. Since the pseudopotential is autonomous, its derivative with respect to time is always equal to zero. A constant energy integral, C, is, therefore, defined as:

$$v^2 = 2U^* - C$$

which remains constant along any natural solution to the MCR3BP equations of motion. This expression reveals that increasing C is equivalent to decreasing the physical energy of P_3 relative to the three-body system. Rearranging, the constant of integration in terms of the state variables in the rotating frame is expressed as:

$$C = x^2 + y^2 + \frac{2(1-\mu)}{r_1} + \frac{2\mu}{r_2} + \frac{2k}{r_1 r_2} - \dot{x}^2 - \dot{y}^2 - \dot{z}^2 \tag{2.19}$$

When the contribution of the three-body potential is negated by selecting $k = 0$, this energy integral reduces to the well-known Jacobi Constant of the CR3BP [6].

2.6 Equilibrium Points

Despite the lack of an analytical solution, significant insight into the dynamics in the MCR3BP emerges from particular solutions - the simplest being in the form of equilibrium points. These are points in the phase space, $(x, y, z, \dot{x}, \dot{y}, \dot{z})$, with an acceleration of zero. If the velocities are also equal to zero, the equations of motion, equations (2.15)-(2.17), simplify to:

$$\frac{\partial U^*}{\partial x} = \frac{\partial U^*}{\partial y} = \frac{\partial U^*}{\partial z} = 0$$

Points of equilibrium in the rotating frame are, therefore, determined as stationary points of the pseudopotential function, U^*.

Five intervals for the possible locations of the equilibrium points are identified by examining these partial derivatives. When $z = 0$, the partial derivative of U^* with respect to z is equal to zero, placing all five equilibrium points within the plane of motion of the primaries. If the y component is zero, there are three intervals in which an equilibrium point could potentially exist:

$$(x + \mu) > 0, (x - 1 + \mu) > 0$$

$$(x + \mu) < 0, (x - 1 + \mu) < 0$$

$$(x + \mu) > 0, (x - 1 + \mu) < 0$$

The equilibrium points are computed by numerically solving the equations of motion when the relative accelerations and velocities are both zero, providing initial guesses in each of the three intervals. Two additional equilibrium points exist above and below the $\hat{x}$ axis and are located by solving for the stationary points of the pseudopotential written in terms of the variables r_1 and r_2. Physical combinations of x and y coordinates that correspond to these stationary points locate the equilibrium points that exist off the x-axis.

In the CR3BP, or when $k = 0$ in the MCR3BP, there are five well-known equilibrium points, all in the plane of motion of the two primaries: three collinear points located along the $\hat{x}$ line, and two equilateral points with a nonzero component in the $\hat{y}$ direction, located such that $r_1 = r_2 = 1$. These five equilibrium points are labeled L_i, for $i = 1, 2, 3, 4, 5$. The location of the equilibrium points with respect to the primaries in the rotating frame appear in Figure 2.3 for $\mu = 0.3$, and are labeled consistent with the conventional numbering for each point. For a nonzero value of the constant that scales the three-body potential contribution in the MCR3BP, the number and location of the equilibrium points differs from those in the CR3BP, impacting the behavior of P_3.

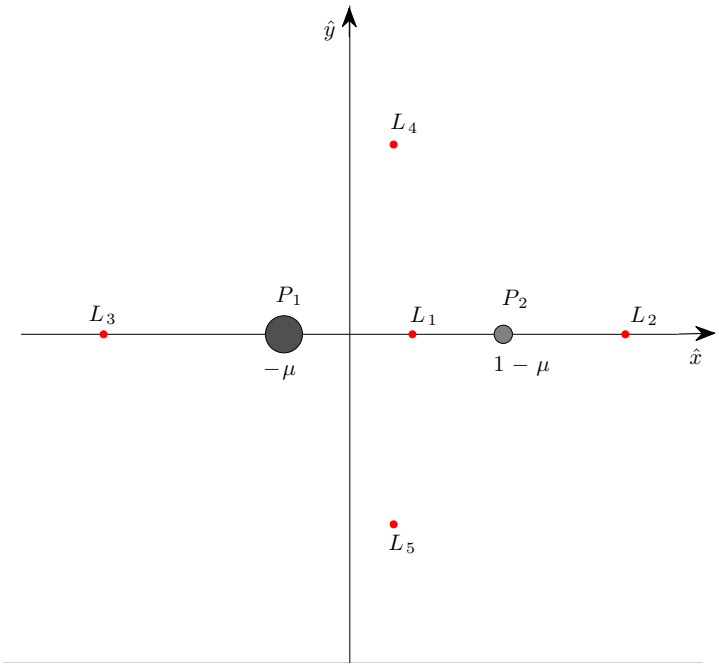

Figure 2.3. Equilibrium points in the CR3BP relative to the two primaries, shown for $\mu = 0.3$

2.7 Zero Velocity Curves

The dynamics that emerge in the MCR3BP are explored by searching for points in the phase space with a velocity of zero relative to the rotating frame. In contrast to equilibrium solutions, this infinite set of points can include nonzero accelerations. Recall the energy constant derived in equation (2.19), rearranged to isolate the magnitude of the velocity:

$$\dot{x}^2 + \dot{y}^2 + \dot{z}^2 = x^2 + y^2 + \frac{2(1-\mu)}{r_1} + \frac{2\mu}{r_2} + \frac{2k}{r_1 r_2} - C$$

When the speed is equal to zero, an infinite set of points, $(x, y, z, 0, 0, 0)$, satisfies the following expression for a given value of the energy constant, C:

$$x^2 + y^2 + \frac{2(1-\mu)}{r_1} + \frac{2\mu}{r_2} + \frac{2k}{r_1 r_2} = C$$

Together, these points form a surface in three-dimensional space. Since the scope of this investigation is limited to planar motion of P_3, it is sufficient to consider the

intersections of these surfaces with the plane of motion of the primaries. Within the $x-y$ plane, the curves created by these intersections are denoted zero velocity curves.

In the plane, on either side of the closed curves, the square of the velocity is either positive or negative. The zero velocity curves therefore separate regions in the phase space with either real or imaginary velocity magnitudes. Given that imaginary speeds are not physically valid, zero velocity curves separate regions of allowable and forbidden motion. Accordingly, the zero velocity curves cannot be crossed. Thus, zero velocity curves are useful in visualizing regions that bound the motion for P_3.

For a value of the energy constant that is equal to $C(L_i)$, that is, the energy constant evaluated at one of the equilibrium points, any point on the zero velocity curve possesses no acceleration relative to the rotating frame. Figure 2.4 depicts the zero velocity curves at the four specific values of C that correspond to the five equilibrium points in the CR3BP, or, equivalently, the MCR3BP with $k = 0$, at a mass ratio $\mu = 0.3$. The dark shaded regions are forbidden to motion, and white space represents allowable regions for P_3. Equilibrium points are colored in red and the two primaries are represented by blue circles. Since the primaries are modeled as point masses, their sizing in this figure is purely illustrative. When P_3 is located in the vicinity of either primary, it is in the "interior region", while the "exterior region" encompasses the phase space exterior to the zero velocity curves.

Analysis of the zero velocity curves across a range of energy levels reveals the regions that P_3 can traverse along a single, natural trajectory. From a value $C = C(L_1)$, raising the energy level, or, equivalently, decreasing the value of C, results in growth of the allowable interior regions. Beginning at a constant of motion that is higher than $C(L_1)$, P_3 can move near one of the primaries or in the exterior region, beyond the zero velocity curves. When the constant of motion is lowered below that of L_1, P_3 is able to move between the vicinity of P_1 and P_2 or exterior to the zero velocity curves, but not between all regions of the phase space. Decreasing the value of the constant further, below $C(L_2)$, P_3 may move between the vicinity of either primary and the exterior region. Any exchange between the exterior and interior regions at this

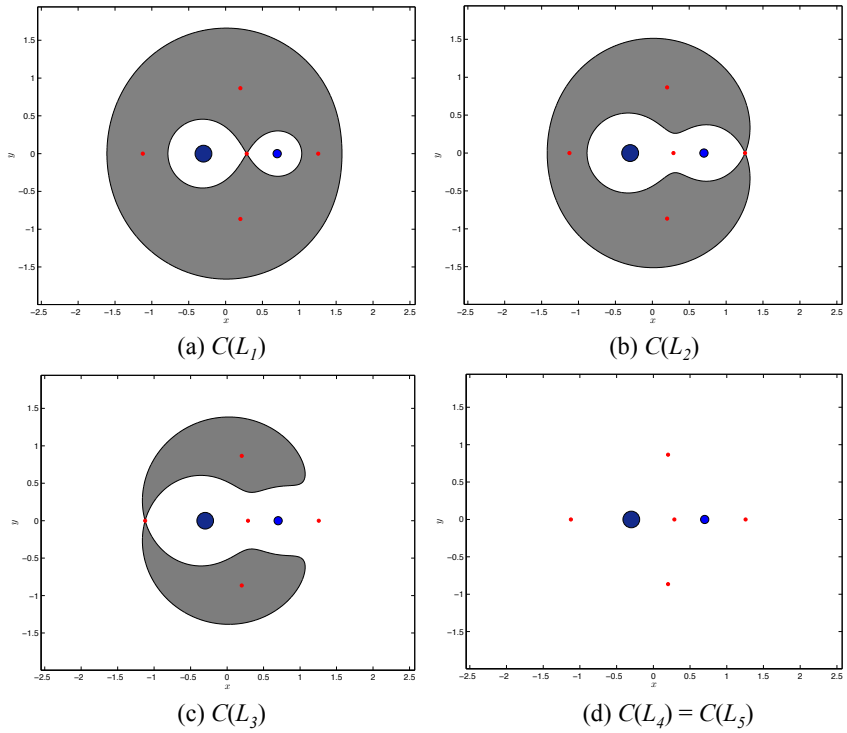

Figure 2.4. Zero Velocity Curves of the CR3BP (equivalently, the MCR3BP with $k = 0$) for energy integrals evaluated at the equilibrium points, where $C(L_1) > C(L_2) > C(L_3) > C(L_4)$, for $\mu = 0.3$.

energy level occurs in the vicinity of L_2, i.e., the L_2 gateway. If the energy constant is slightly below $C(L_3)$, further interchange between the interior and exterior region may now potentially occur through the L_3 gateway. When the energy constant is reduced to a value below that of L_4 or L_5, P_3 can move anywhere within the plane of the primaries. At these higher values of the energy constant, zero velocity surfaces still exist above and below the $z = 0$ plane. Accordingly, while motion in the plane is unrestricted at low values of C, P_3 is still bounded by zero velocity surfaces in three-dimensional space. The zero velocity curves do not, however, provide insight into the form of the infinite solutions present in the allowable regions; instead, alternative techniques must be employed to locate solutions with desired characteristics.

3. TIME-VARYING SOLUTIONS IN THE CIRCULAR RESTRICTED THREE-BODY PROBLEM

Since the equations of motion in the CR3BP are nonintegrable and autonomous, four types of steady-state solutions exist: equilibrium points, periodic orbits, quasi-periodic orbits, and chaotic motion [20]. Each of these solutions, for a mass ratio of $\mu = 0.3$, is plotted in Figure 3.1(a)-(d) in position space, with blue filled circles indicating the location of the primaries. From the derivation in Section 2.6, the equilibrium point locations remain constant over time. Periodic solutions, however, are time-varying and repeatable. The dense set of periodic orbits in the CR3BP forms the underlying structure of the phase space: a stable orbit attracts trajectories in its vicinity, while trajectories near an unstable orbit flow away from the orbit [21]. Thus, identifying periodic orbits and evaluating their stability delivers significant insight into the behavior in their vicinity. Quasi-periodic orbits offer additional characteristics concerning the dynamical environment. These orbits are bounded and each traces out a torus, with a nearby stable periodic orbit at its center [6]. Investigating the properties of quasi-periodic orbits and their excursions within the phase space completes the representation of stable dynamics within the CR3BP. Although the complete, three-dimensional equations of motion are available, only planar solutions are considered throughout the remainder of this investigation.

3.1 Periodic Orbits

In dynamical systems, a closed, time-varying trajectory is identified as a periodic orbit. Defining a four element state, $\bar{x}$, as the column vector, $\bar{x} = [x, y, \dot{x}, \dot{y}]^T$,

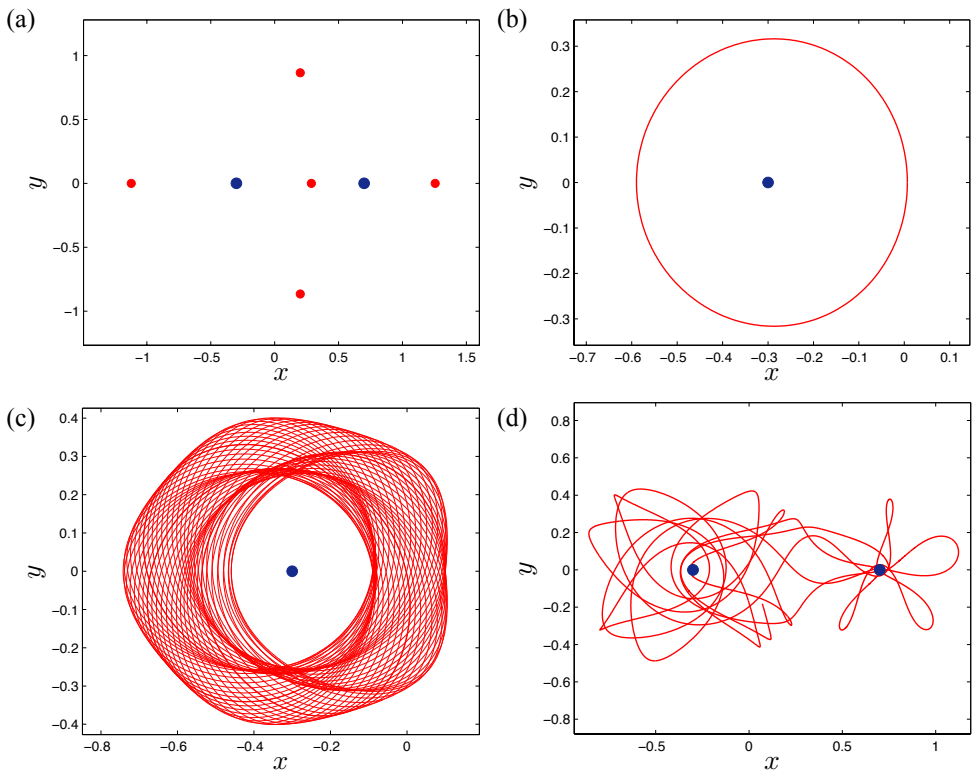

Figure 3.1. Examples of steady-state solutions in the CR3BP for $\mu = 0.3$: (a) equilibrium points, (b) a periodic orbit, (c) a quasi-periodic orbit, and (d) chaotic motion.

any state along a planar periodic orbit in the rotating frame satisfies the following repeatability condition:

$$\bar{x}(t) = \bar{x}(t+T) \tag{3.1}$$

when integrated for a time T. The minimum positive value of T for which this condition is satisfied is labeled the period [20]. Given the definition of the rotating frame in Section 2.4, an orbit that is periodic in the rotating frame is only periodic in the inertial frame if the orbital period is a rational multiple of the period of the primaries. In the rotating coordinate system, a periodic orbit can encircle the primaries or an equilibrium point q times during one period; this is labeled a period-q orbit. Examples appear in Figure 3.2: a period-1 orbit in Figure 3.2(a) encircles P_2 once and, in Figure 3.2(b), a period-3 orbit completes three clockwise revolutions about both

primaries. More generally, a period-q orbit can travel about either or both of the primaries in any direction in the rotating frame.

Periodic orbits are, therefore, further classified by their direction of motion. Recall from Section 2.4 that the primaries move with an orbital angular momentum vector parallel to the $+\hat{Z}$-direction in the inertial frame, or equivalently, in the $+\hat{z}$-direction as defined in the rotating frame. This angular momentum vector is used as a reference when describing the direction of motion of a trajectory as viewed in the rotating frame. An arbitrary trajectory, representing the path of particle P in the vicinity of a reference point, appears in Figure 3.3. At any time t^* along the path, the state describing the position and velocity of P, relative to the primary P_i and with respect to the rotating frame, is represented by the vector $\bar{x}^*_{P_i}$. This four-dimensional relative state vector, $\bar{x}^*_{P_i}$, is comprised of the two-dimensional relative vectors of position, $\bar{r}$, and velocity, $\bar{v}$, as illustrated. Then, the specific angular momentum for the motion of P with respect to the reference primary is evaluated at t^* as the cross product $\bar{H} = \bar{r} \times \bar{v}$. An arc with an instantaneous angular momentum vector in the $+\hat{z}$-direction is prograde with respect to the selected primary, while an instantaneous angular momentum in the $-\hat{z}$-direction corresponds to a retrograde path. In the rotating frame, a periodic orbit can appear to wind about one of the primaries in an

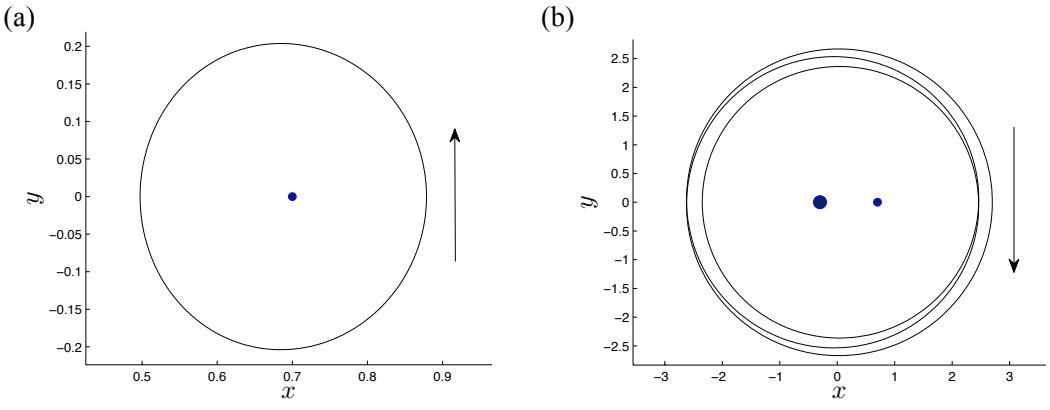

Figure 3.2. A period-1 orbit (a) and period-3 orbit (b) plotted in the rotating frame.

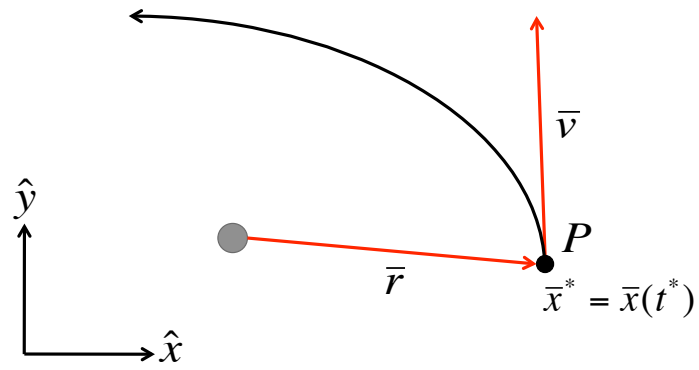

Figure 3.3. Definition of position and velocity vectors with respect to one of the primaries in the rotating frame.

entirely prograde or retrograde direction, or a particle moving along a periodic path can alternate between the two directions as it encircles one or both of the primaries. When viewed from an observer above the plane of motion, the period-1 orbit in Figure 3.2(a) reflects motion that is counterclockwise about P_2. Since the associated angular momentum vector is parallel to the $+\hat{z}$-direction, this periodic orbit is defined as prograde with respect to P_2. Similarly, the period-3 orbit in Figure 3.2(b) is clearly retrograde with respect to both P_1 and P_2.

3.2 Quasi-Periodic Orbits

Stable periodic orbits are typically surrounded by quasi-periodic orbits, corresponding to nonperiodic, bounded motion that lies on a two-dimensional torus [21]. As illustrated in Figure 3.4, the closed surface of a torus, outlined in grey, is generated as the product of two circles [22]. The central circle highlighted in red corresponds to the periodic orbit at the center of the torus, while the blue circle corresponds to rotation transverse to the periodic orbit. Each quasi-periodic orbit, described by the

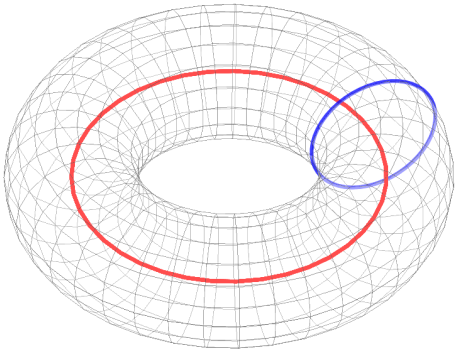

Figure 3.4. A two-dimensional torus, the product of two circles.

evolving states $\bar{x}(t)$, is, therefore, parametrically defined using two incommensurate, fundamental frequencies [6]:

$$\bar{x}(t) = \bar{A}_0 + \bar{A}_1 cos(\omega_1 t) + \bar{B}_1 sin(\omega_1 t) + \bar{A}_2 cos(\omega_2 t) + \bar{B}_2 sin(\omega_2 t) \tag{3.2}$$

where $\bar{A}_i$ and $\bar{B}_i$ are, respectively, the coefficients of the cosine and sine components corresponding to the i-th frequency [23]. When the two frequencies, w_1 and w_2, are commensurate, their ratio is equated to the ratio of two integers: a limiting case that corresponds to a resonant periodic orbit. Computing and interpreting this frequency decomposition is, in fact, a key element in the analysis of the dynamics in the CR3BP.

3.3 State Transition Matrix

Given a reference arc, a neighboring trajectory that represents a periodic or quasi-periodic solution is located using the state transition matrix and a linear corrections process. Such a process is based on first-order variational equations relative to the reference trajectory. A sample reference trajectory, $\bar{x}^*(t)$, with an initial condition $\bar{x}^*(t_0)$ appears in Figure 3.5. Introducing a variation $\delta\bar{x}(t_0)$ to define a nearby initial state in the vicinity of the reference:

$$\bar{x}(t_0) = \bar{x}^*(t_0) + \delta\bar{x}(t_0)$$

such that, after numerical integration, the perturbed trajectory is represented as:

$$\bar{x}(t) = \bar{x}^*(t) + \delta\bar{x}(t)$$

Since each solution in the CR3BP is unique, integrating the reference and perturbed initial states results in two distinct paths. Consequently, at a time t_f, the states along these two paths are not equal and their difference, $\delta\bar{x}(t_f)$, is estimated using a first-order Taylor series expansion about the reference trajectory. The general equations of motion are expressed in first-order form and, after introducing the variation from the reference, appear as:

$$\dot{\bar{x}} = \dot{\bar{x}}^* + \delta\dot{\bar{x}} = \bar{f}(\bar{x}^* + \delta\bar{x})$$

where $\bar{f}$ represents the nonlinear differential equations in the CR3BP. A Taylor series expansion about the reference trajectory yields the first-order terms:

$$\dot{\bar{x}} \approx \bar{f}(\bar{x}^*, t) + \left.\frac{\partial \bar{f}}{\partial \bar{x}}\right|_{\bar{x}^*} \delta\bar{x}$$

which simplifies to the vector, linear variational equation:

$$\delta\dot{\bar{x}} \approx \left.\frac{\partial \bar{f}}{\partial \bar{x}}\right|_{\bar{x}^*} \delta\bar{x} \tag{3.3}$$

Solutions to this equation are of the form:

$$\delta\bar{x}(t) = \Phi(t, t_0)\delta\bar{x}(t_0) \tag{3.4}$$

where $\Phi(t, t_0)$ denotes the state transition matrix (STM). Analysis of this relationship reveals that the STM is essentially a linear mapping from t_0 to a time t. Substituting this solution into equation (3.3) produces the first-order matrix differential equation for the STM:

$$\dot{\Phi}(t, t_0) = \left.\frac{\partial \bar{f}}{\partial \bar{x}}\right|_{x^*} \Phi(t, t_0) \tag{3.5}$$

with the initial condition $\Phi(t_0, t_0) = I_{4\times4}$, where $I_{4\times4}$ represents the 4×4 identity matrix [22]. The elements of the STM can, therefore, be appended to the state vector along the reference trajectory and simultaneously integrated.

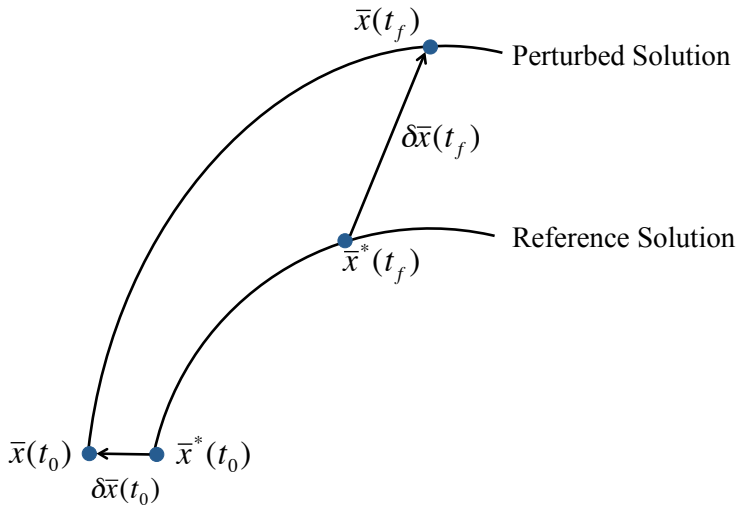

Figure 3.5. Deviation in states at times t_0 and t_f along a reference path and a nearby perturbed trajectory.

Many useful properties exist for the STM, including its inherent decomposition into the product of intermediate STMs and its symplecticity. First, by the chain rule, equation (3.4) is rewritten at time t_f as:

$$\delta\bar{x}(t_f) = \Phi(t_f, t_0)\delta\bar{x}(t_0) \tag{3.6}$$

Consecutively employing the chain rule and substituting the variations at intermediate times produces the equivalent expression:

$$\delta\bar{x}(t_f) = \Phi(t_f, t_{f-1})\Phi(t_{f-1}, t_{f-2})....\Phi(t_1, t_0)\delta\bar{x}(t_0) \tag{3.7}$$

Combining equations (3.6) and (3.7) reveals that an STM, $\Phi(t_f, t_0)$, can be computed as the product of intermediate STMs:

$$\Phi(t_f, t_0) = \Phi(t_f, t_{f-1})\Phi(t_{f-1}, t_{f-2}).....\Phi(t_2, t_1)\Phi(t_1, t_0) \tag{3.8}$$

where $t_0 < t_1... < t_{f-1} < t_f$. Additional useful properties of the STM are deduced as a consequence of the fact that it is a symplectic matrix. For a $2n \times 2n$ matrix, S, to be considered symplectic, it must satisfy the condition:

$$S^T JS = J \tag{3.9}$$

where J is defined as the constant $2n \times 2n$ matrix:

$$J = \begin{bmatrix} 0_{n\times n} & I_{n\times n} \\ -I_{n\times n} & 0_{n\times n} \end{bmatrix}$$

In this matrix, $I_{n\times n}$ is the $n \times n$ identity matrix and $0_{n\times n}$ is an $n \times n$ matrix of zeroes [24]. This condition reflects the fact that S is a symplectic transformation matrix that preserves many properties of the flow, including the volume of the phase space. Since the STM is initially equal to the identity matrix, it is symplectic at t_0. To determine whether the STM satisfies this condition at any other time t, the derivative of the symplectic condition can be analyzed. Using the chain rule, this derivative is equal to:

$$\frac{d}{dt}\left(\Phi(t,t_0)^T J \Phi(t,t_0)\right) = \dot{\Phi}(t,t_0)^T J \Phi(t,t_0) + \Phi(t,t_0)^T J \dot{\Phi}(t,t_0)$$

Substituting the first-order differential equation for the STM into this expression:

$$\begin{aligned} \frac{d}{dt}\left(\Phi(t,t_0)^T J \Phi(t,t_0)\right) &= \Phi(t,t_0)^T \left.\frac{\partial \bar{f}}{\partial \bar{x}}\right|_{\bar{x}^*}^T J \Phi(t,t_0) + \Phi(t,t_0)^T J \left.\frac{\partial \bar{f}}{\partial \bar{x}}\right|_{\bar{x}^*} \Phi(t,t_0) \\ &= \Phi(t,t_0)^T \left[\left.\frac{\partial \bar{f}}{\partial \bar{x}}\right|_{\bar{x}^*}^T J + J \left.\frac{\partial \bar{f}}{\partial \bar{x}}\right|_{\bar{x}^*} \right] \Phi(t,t_0) \end{aligned} \tag{3.10}$$

Recall that $\left.\frac{\partial \bar{f}}{\partial \bar{x}}\right|_{\bar{x}^*}$ is a matrix representing the derivative of the six first-order nonlinear differential equations with respect to the state vector, evaluated at $\bar{x}^*(t^*)$. It is comprised of two nonzero submatrices:

$$\left.\frac{\partial \bar{f}}{\partial \bar{x}}\right|_{\bar{x}^*} = \begin{bmatrix} 0_{3\times 3} & I_{3\times 3} \\ \frac{\partial^2 U}{\partial \bar{x}^2} & 0_{3\times 3} \end{bmatrix}$$

where $\frac{\partial^2 U}{\partial \bar{x}^2}$ is a matrix of second derivatives of the potential function with respect to the state vector. Given the form of $\left.\frac{\partial \bar{f}}{\partial \bar{x}}\right|_{\bar{x}^*}$, this matrix satisfies the following relationship:

$$J \left.\frac{\partial \bar{f}}{\partial \bar{x}}\right|_{\bar{x}^*} = \begin{bmatrix} \frac{\partial^2 U}{\partial \bar{x}^2} & 0_{3\times 3} \\ 0_{3\times 3} & I_{3\times 3} \end{bmatrix} = -\left.\frac{\partial \bar{f}}{\partial \bar{x}}\right|_{\bar{x}^*}^T J$$

Substituting this relationship into the brackets in equation (3.10), the time derivative of $\Phi(t,t_0)^T J \Phi(t,t_0)$ is equal to zero for any time t. Since the initial STM is symplectic,

it is also symplectic for all time. As a direct result of this property, the determinant of the STM is theoretically always equal to 1.

The symplectic nature of the STM is also exploited to determine and explore the eigenvalues of the STM. Substituting the STM into the symplectic condition in equation (3.9) and rearranging, such that J is a similarity transformation, the STM satisfies:

$$\Phi(t,t_0)^T = J^{-1}\Phi(t,t_0)^{-1}J \tag{3.11}$$

This relationship reveals that $\Phi(t,t_0)^T$ and $\Phi(t,t_0)^{-1}$ are similar matrices. Denoting the $2n$ eigenvalues of $\Phi(t,t_0)$ - and equivalently $\Phi(t,t_0)^T$ - as λ_i, the eigenvalues of $\Phi(t,t_0)^{-1}$ must therefore be equal to $1/\lambda_i$. Similar matrices possess eigenvalues that are equal; thus, the eigenvalues of the STM must occur in reciprocal pairs λ_i and $1/\lambda_i$, i.e., a result denoted Lyapunov's theorem.

Since the STM represents the sensitivity of a solution at a time downstream to perturbations in the initial state, its eigenvalues offer information about trajectories in the vicinity of $\bar{x}^*(t)$. Thus, for trajectory computation, simultaneous integration of the state, $\bar{x}(t)$, and the STM, $\Phi(t,t_0)$, is very useful. The accuracy of the STM, however, is limited for integration over long periods of time, or for prediction of motion resulting from large perturbations. The former is typically monitored by comparing the determinant of the STM to one, supplying a measure of the numerical error incurred during integration.

3.4 Stability of Periodic Orbits

The stability of a periodic orbit is deduced from the monodromy matrix, defined as the STM propagated for precisely one period of the orbit [24]. Recall that the general solution to the variational equations of motion, linearized relative to a given periodic orbit, is written as:

$$\delta\bar{x}(t) = \Phi(t,0)\delta\bar{x}(t_0)$$

where $\delta\bar{x}(t_0)$ is the variation with respect to the initial state along the planar orbit [22]. In contrast to constant coefficient matrices that are straightforwardly decomposed into eigenvalues and eigenvectors to assess stability, a different strategy is necessary to determine the modes of behavior in the vicinity of a periodic solution. Via Floquet theory, the time-varying STM is decomposed into the following form:

$$\Phi(t,0) = F(t)e^{\Omega t}F(0)^{-1}$$

where $F(t)$ is a periodic matrix and the diagonal elements of Ω are the Poincaré exponents, Ω_i, for $i = 1...4$ [22]. The initial value of $F(t)$ is available by evaluating this decomposition after one period, T, and noting that $F(T) = F(0)$:

$$\Phi(T,0) = F(0)e^{\Omega T}F(0)^{-1} \tag{3.12}$$

Since $e^{\Omega T}$ is a diagonal matrix, $F(0)$ is formed from the eigenvectors of the monodromy matrix and the Poincaré exponents are related to its eigenvalues such that $\lambda_i = \pm e^{\Omega_i T}$. Thus, the eigenvalues of the monodromy matrix are the modes of the linear dynamics in the vicinity of the periodic orbit.

The eigenvalues of the monodromy matrix reflect the characteristics of the underlying linear system; however, the nontrivial eigenvalues also supply insight into the stability of the periodic orbit in the original, nonlinear system. Given a reference periodic trajectory, $\bar{x}_{PO}(t)$, the Lyapunov definition of stability decomposes a stability assessment of this solution into three classes:

- A reference solution is stable if a nearby solution, $\bar{x}(t)$, remains bounded and there exists a reasonable, positive constant $\epsilon > 0$ such that $\left|\left|\bar{x}(t) - \bar{x}_{PO}(t)\right|\right| \leq \epsilon$ for all time.

- A reference solution is asymptotically stable if a nearby solution, $\bar{x}(t)$, converges to the reference trajectory such that $\lim_{t\to\infty} \left|\left|\bar{x}(t) - \bar{x}_{PO}(t)\right|\right| = 0$

- A reference solution is unstable if a nearby solution, $\bar{x}(t)$, diverges from the reference solution over time.

Thus, this definition of stability is based on the concept of boundedness [6]. Analyzing the eigenvalues of the monodromy matrix allows for an assessment of the nonlinear stability of the periodic reference orbit using this definition as it is applied to maps within the context of dynamical systems theory [22]. Each planar, periodic orbit possesses a monodromy matrix that can be decomposed into four eigenvalues and their associated eigenvectors. Two of the eigenvalues are equal to one; one of these correspond to the eigenvector direction along the periodic orbit and the eigenvector corresponding to the second unit eigenvalue is directed along the family of orbits [24]. The other two nontrivial eigenvalues are typically represented in the form $\lambda = a \pm bi$, in terms of two real numbers, a and b. Three possible forms for each eigenvalue of the monodromy matrix emerge:

- $\lambda_{1,2} = \pm bi$: purely imaginary eigenvalues correspond to oscillatory motion, as a direct result of Euler's formula. The solution neither decays nor grows over time, so the resulting trajectory is bounded and stable.

- $\lambda_{1,2} = a \pm bi$: complex roots occur in conjugate pairs, corresponding to motion that is oscillatory and either grows or decays over time. If $|a| > 1$, the solution is unstable and diverges, whereas if $|a| \leq 1$, the solution is linearly stable.

- $\lambda_1 = a$, $\lambda_2 = 1/a$: real roots correspond to exponential growth or decay of the solution. An eigenvalue of $|\lambda| > 1$ indicates an unstable mode, while an eigenvalue of $|\lambda| \leq 1$ corresponds to the stable mode. Since the eigenvalues of the monodromy matrix occur in reciprocal pairs, nontrivial eigenvalues with $|a| > 1$ indicate that a periodic solution is unstable.

Using these classifications, stable periodic orbits possess a nontrivial pair of complex or imaginary eigenvalues, $\lambda_1, \lambda_2 = a \pm bi$, while nontrivial eigenvalues in the form $|\lambda_1| > 1$ and $|\lambda_2| < 1$ emerge when the periodic orbits are unstable [24].

Real eigenvalues with identical magnitude and opposite sign correspond to modes with an identical absolute measure of convergence or divergence with respect to a reference trajectory; however, the distinct difference between the flow governed by

each mode is the relative direction of motion. The examples sketched in Figure 3.6 demonstrate motion governed by a (a) positive and (b) negative real eigenvalue, respectively, with magnitude less than 1. For flow represented by a stable mode described by a positive eigenvalue, the nearby, grey trajectories approach the reference periodic orbit, in blue, with an even number of twists about the orbit. A stable, negative mode, however, reflects the twisting of nearby trajectories an odd number of times around the periodic orbit - analogous to motion along a Mobius strip [25].

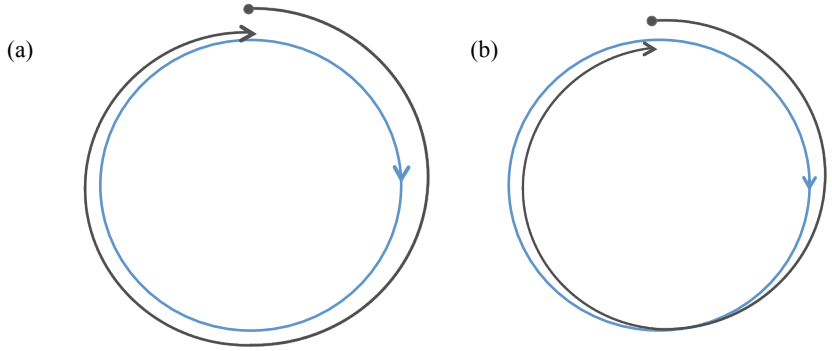

Figure 3.6. Illustration of the motion in the vicinity of the blue periodic orbit. Nearby trajectories are governed by the mode corresponding to (a) a stable, positive eigenvalue and (b) a stable, negative eigenvalue.

3.5 Bifurcations

In the CR3BP, periodic orbits exist in families that, for a constant mass ratio, depend upon the energy constant. Varying C, the natural parameter, directly modifies the vector field, $\bar{f}(\bar{x})$, and, therefore, its infinite set of solutions. A local bifurcation occurs if a change in the energy constant results in a change in the qualitative behavior of trajectories in the vicinity of a periodic orbit. In dynamical systems, a bifurcation may result in a change in the stability of the periodic orbits along a family, the formation of a new family of periodic orbits, or termination of the current family [26].

Since the stability of a periodic orbit reflects the behavior of nearby trajectories, local bifurcations are detected and characterized by monitoring the eigenvalues of the monodromy matrix corresponding to each periodic orbit along a family. In the complex plane, these eigenvalues are located with respect to the unit circle, as illustrated in Figure 3.7. Nontrivial eigenvalues located on the red unit circle possess a magnitude of 1, corresponding to oscillatory modes. A pair of reciprocal eigenvalues that are located off the unit circle, however, indicate the presence of one unstable mode ($|\lambda| > 1$) and one stable mode ($|\lambda| < 1$) governing motion in the vicinity of the periodic orbit.

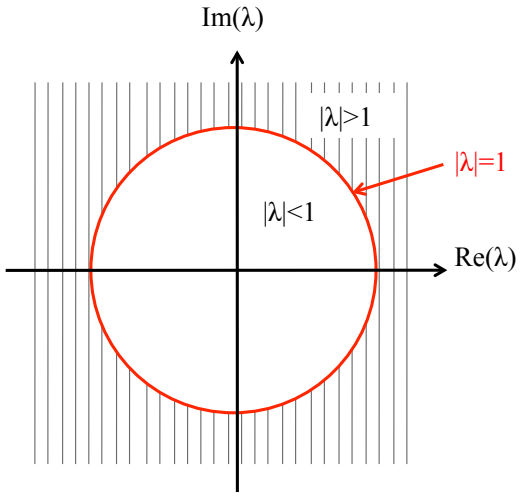

Figure 3.7. Magnitude of the eigenvalues in the complex plane with respect to the unit circle, colored red.

Two-dimensional visualization of the eigenvalues of the monodromy matrix in the complex plane, however, does not reflect the value of the natural parameter for the corresponding periodic orbit. To reduce the dimension of the graphical representation of a pair of eigenvalues, a stability index is introduced. This quantity is defined as the sum of two reciprocal eigenvalues, equal to:

$$s = \lambda + \frac{1}{\lambda} \tag{3.13}$$

Given the form of this expression, s is a real number; this statement is always true, even for a pair of complex conjugate eigenvalues. In addition, the stability index is used to locate possible bifurcations by detecting changes in the stability of the periodic orbits comprising a family. As an example, the critical eigenvalues $\lambda_1, \lambda_2 = +1, +1$ correspond to the stability index $s = 2$, while eigenvalues equal to $\lambda_1, \lambda_2 = -1, -1$ produce a stability index equal to $s = -2$. As the stability index passes through either of these critical values, the nontrivial eigenvalues associated with the periodic orbits along a family transition between the unit circle and the real axis. Confirmation of the occurrence of a bifurcation at these sample values of the stability index requires verification; the eigenvalues of the monodromy matrix of the corresponding orbit must not be complex for $|s| \geq 2$.

Although many bifurcations exist in dynamical systems, two types emerge within the dynamical environment that is the focus of this investigation: tangent, and period-multiplying bifurcations. The nontrivial eigenvalues reflecting the stability of the periodic orbits on either side of these bifurcations are depicted in the complex plane in Figure 3.8: the pair of eigenvalues are blue on one side of the critical value and green on the opposite side of the bifurcation, plotted in red. Each type of bifurcation is associated with a particular change in the characteristics of the dynamics in the neighborhood of the periodic orbits in a family.

3.5.1 Tangent Bifurcation

A family of periodic orbits undergoes a tangent bifurcation when the stability of its orbits changes with the energy constant. During this type of local bifurcation, the nontrivial eigenvalues of the monodromy matrix pass through the critical values $\lambda_1 = \lambda_2 = +1, +1$. Simultaneously, the stability index passes through $s = 2$. The tangent bifurcation is further classified into three types [26]:

- Fold bifurcation: The orbits along a single family shift in terms of their stability, neither creating nor intersecting any other families.

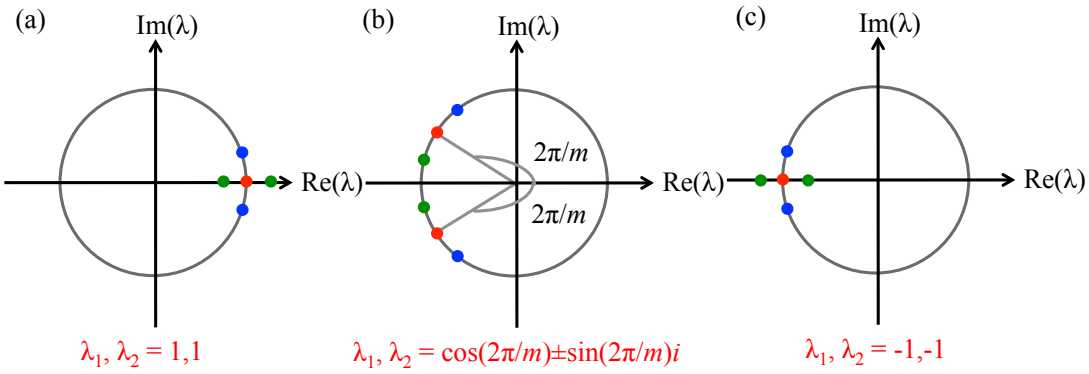

Figure 3.8. Eigenvalues on either side of a (a) tangent bifurcation, (b) period-multiplying bifurcation for a multiplicative factor m and (c) period-doubling bifurcation (leading to a stability change).

- Pitchfork bifurcation: As the stability of the orbits along a family changes, two additional families of similar period are formed. These new families of orbits possess the same stability as members of the original family prior to the bifurcation.

- Transcritical bifurcation: A family of stable orbits intersects a family of unstable orbits. At the intersection, the two families exchange stability characteristics.

Across each type of tangent bifurcation, the eigenvalues that reflect the stability of orbits along a family transition between the unit circle and the real axis, as depicted in Figure 3.8(a).

3.5.2 Period-Multiplying Bifurcation

During a period-multiplying bifurcation, a family of period-mq orbits emerges from a family of period-q orbits. At the critical value of the natural parameter, the orbit located at the intersection of the two families is equivalently described as a period-mq orbit or a period-q orbit traced out m times. Accordingly, the monodromy

matrix of the period-mq orbit is written in terms of the monodromy matrix of the period-q orbit as:

$$\begin{aligned}\Phi_{mq}(0,mT) &= \Phi_q(0,T)\Phi_q(T,2T)....\Phi_q((m-2)T,(m-1)T)\Phi_q((m-1)T,mT) \\ &= [\Phi_q(0,T)]^m\end{aligned}$$

where T is the period of the period-q orbit, and the subscript identifies the corresponding orbit. Decomposing these two monodromy matrices via Floquet theory, the modes of the period-mq orbit are expressed in terms of the modes of the period-q orbit as:

$$\lambda_{mq} = \lambda_q^m \tag{3.14}$$

At the period-multiplying bifurcation, the monodromy matrix of a planar period-mq orbit has two trivial pairs of eigenvalues: one pair corresponding to the periodicity of orbits along a family and the other pair signifying its intersection with another family. Since $\lambda_{mq} = 1$ for the first period-mq orbit in the family, a period-multiplying bifurcation with multiplicity m occurs when the eigenvalues of the monodromy matrices of period-q orbits along a family pass through the first and $(m-1)$-th complex roots of unity, as sketched in Figure 3.8(b) [27]. Therefore, this bifurcation is detected when the eigenvalues are equal to:

$$\lambda_1, \lambda_2 = \cos\left(\frac{2\pi}{m}\right) \pm \sin\left(\frac{2\pi}{m}\right) i \tag{3.15}$$

or, equivalently, when the stability index has the value:

$$s = 2\cos\left(\frac{2\pi}{m}\right) \tag{3.16}$$

Since the stability index does not reflect the imaginary components of any complex conjugate eigenvalues, confirmation of a period-multiplying bifurcation requires verification that the eigenvalues do not split off the unit circle after passing through the corresponding unity roots; such behavior corresponds to a Krein collision.

3.5.3 Period-Doubling Bifurcation Leading to Stability Change

One limiting case of the period-multiplying bifurcation is particularly pertinent to this investigation: the period-doubling bifurcation that is accompanied by a change in the orbital stability. A period-doubling bifurcation is detected when a pair of eigenvalues passes through $\lambda_1, \lambda_2 = -1, -1$, and, therefore, corresponds to a critical value of the stability index, such that $s = -2$. As depicted in Figure 3.8(c), the orbits on one side of the bifurcation possess two nontrivial eigenvalues located on the unit circle. On the opposite side of the bifurcation, however, the eigenvalues of the monodromy matrix are located on the real axis, i.e., $\lambda_1 < -1$ and $\lambda_2 > -1$. This behavior corresponds to the changing stability characteristics of the periodic orbits along the family, i.e, transitioning between stable and unstable [26].

3.6 A Differential Corrections Strategy

Since the equations of motion are not solvable analytically, the search for a periodic orbit - or a trajectory with a set of desired characteristics at its endpoints - requires the solution to a two-point boundary value problem. Various numerical methods are available to solve a problem of this form; given the nonuniform dynamical sensitivity in the CR3BP, shooting methods are employed in this investigation in contrast to relaxation methods.

Consider an arbitrary reference solution to a system of first-order nonlinear differential equations, $\dot{\bar{x}} = \bar{f}(\bar{x}(t))$, given an initial condition, $\bar{x}^*(t_1)$, as depicted in Figure 3.9. Integrating this initial condition forward to a time t_2 supplies an initial guess trajectory with a final state vector $\bar{x}^*(t_2)$. Although the elements comprising this final state vector do not meet a specified set of constraints, an alternative path within its vicinity may satisfy the requirements, that is, $\bar{x}_d(t_2 + \delta t_2)$. Modifying the reference initial condition by a variation $\delta\bar{x}(t_1)$ can produce a distinctly different path that, when integrated for a time $t_2 + \delta t_2$, satisfies the specified set of boundary conditions.

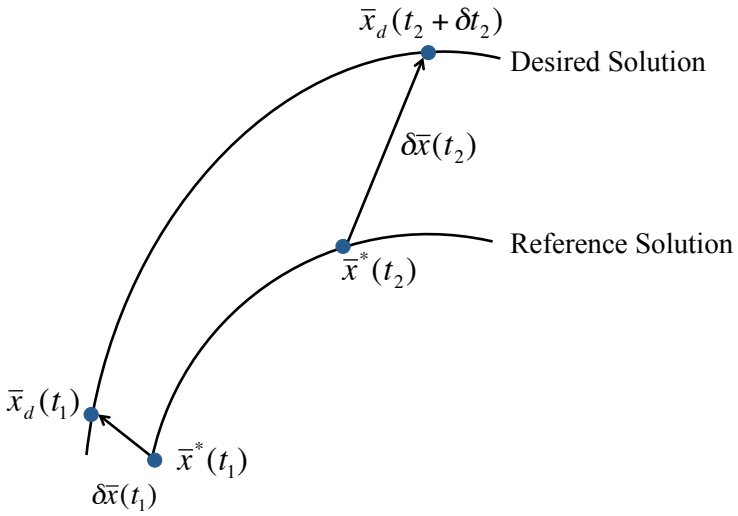

Figure 3.9. Illustration of a shooting method.

The trajectory, $\bar{x}_d(t)$, therefore, represents the solution to the two-point boundary value problem.

The numerical implementation of a shooting method recasts the two point boundary value problem as a vectorial root-finding problem. At the initial point on the path, n_1 components of the state vector $\bar{x}^*(t_1)$ are required. The values of these components are subject to c_1 constraints. Subtracting the number of constraints from the number of components in the initial state, there are $f_1 = n_1 - c_1$ free variables to be specified [28]. These free variables form an f_1-dimensional vector, $\bar{V}$:

$$\bar{V} = \begin{bmatrix} V_1 \\ \vdots \\ V_{c_1} \end{bmatrix}$$

Given the c_1 boundary conditions, this vector completely specifies the initial state, $\bar{x}^*(t_1)$. The n_1 equations of motion are then integrated forward from the initial state for a time $t_2 - t_1$ to obtain the final state, $\bar{x}^*(t_2)$.

Depending on the accuracy of the initial guess for the free variables, $\bar{x}^*(t_2)$ may not satisfy the c_2 scalar boundary conditions imposed at the end of the trajectory.

Accordingly, a c_2-dimensional vector, $\bar{F}$, is defined such that its scalar components, $F_i(\bar{V})$, represent the extent to which the solution violates the independent boundary conditions at its endpoint:

$$\bar{F} = \begin{bmatrix} F_1(\bar{V}) \\ \vdots \\ F_{c_2}(\bar{V}) \end{bmatrix}$$

The constraints are formulated such that $F_i(\bar{V}) = 0$. Consequently, the vector that satisfies $\bar{F} = \bar{0}$, to within a reasonably small tolerance, is denoted $\bar{V}_d$ and describes the desired solution [28].

To determine the vector, $\bar{V}$, that represents the solution that satisfies the boundary conditions in $\bar{F}$, an iterative update procedure is employed. An initial guess for the free variables, $\bar{V}^0$, is first specified. This initial guess is obtained through a variety of methods, including linearization about a known solution and the analysis of a Poincaré map. Assuming that the initial guess is sufficiently accurate, a Taylor series expansion is performed about $\bar{V}^d$, the vector of free variables that represents the initial state along a desired trajectory. Retaining only first-order terms, this expansion is written as:

$$\bar{F}(\bar{V}^d) \approx \bar{F}(\bar{V}^0) + D\bar{F}(\bar{V}^0) \cdot (\bar{V}^d - \bar{V}^0) \tag{3.17}$$

where $D\bar{F}(\bar{V}^0)$ is a Jacobian matrix comprised of the partial derivatives of the constraint vector with respect to the elements of $\bar{V}$:

$$D\bar{F}(\bar{V}) = \begin{bmatrix} \frac{\partial F_1}{\partial V_1} & \cdots & \frac{\partial F_1}{\partial V_{c_1}} \\ \vdots & \ddots & \vdots \\ \frac{\partial F_{c_2}}{\partial V_1} & \cdots & \frac{\partial F_{c_2}}{\partial V_{c_1}} \end{bmatrix} \tag{3.18}$$

Since the vector $\bar{F}$ is equal to the zero vector when the set of free variables deliver the desired solution, equation (3.17) simplifies to:

$$0 \approx \bar{F}(\bar{V}^0) + D\bar{F}(\bar{V}^0) \cdot (\bar{V}^d - \bar{V}^0) \tag{3.19}$$

The approach for solving this expression for $\bar{V}^d$ depends upon the number of independent constraints compared with the number of free variables. If $f_1 = c_2$, the Jacobian

matrix is square and invertible. Rearranging the Taylor series expansion, a first-order update equation is obtained:

$$\bar{V}^d = \bar{V}^0 - D\bar{F}(\bar{V}^0)^{-1}\bar{F}(\bar{V}^0)$$

Generalizing, the update equation at any iteration i is, therefore, expressed as:

$$\bar{V}^{i+1} = \bar{V}^i - D\bar{F}(\bar{V}^i)^{-1}\bar{F}(\bar{V}^i) \tag{3.20}$$

If, however, there are more free variables than constraints, i.e., $f_1 > c_2$, infinitely many solutions satisfy the boundary conditions [28]. From among a number of different options, selecting the minimum-norm solution of equation (3.19), the first-order update equation at iteration i is written as:

$$\bar{V}^{i+1} = \bar{V}^i - D\bar{F}(\bar{V}^i)^T[D\bar{F}(\bar{V}^i) \cdot D\bar{F}(\bar{V}^i)^T]^{-1}\bar{F}(\bar{V}^i) \tag{3.21}$$

Although the rectangular Jacobian matrix $D\bar{F}(\bar{V}^i)$ is not invertible, multiplying it by its transpose produces a square, symmetric matrix that can be inverted.

The update equations, equations (3.20) and (3.21), resemble a vector formulation of the well-known Newton's method, a fixed-point iteration scheme that updates the approximation to a root using the first derivative of the function. Assuming that an initial guess is sufficiently close to the root of $\bar{F}$, Newton's method exhibits second-order convergence over subsequent iterations [29]. Comparing the magnitude of the error vector at iterations i and $i+1$, the ratio:

$$\frac{||\bar{F}(\bar{V}^{i+1})||}{||\bar{F}(\bar{V}^i)||^2} \tag{3.22}$$

should approach a constant value, demonstrating the quadratic convergence of this fixed point iteration scheme [29]. Monitoring the convergence rate also allows for verification that the Jacobian matrix is correctly computed.

3.6.1 Variable-Time Single Shooting Algorithm

In this investigation, a planar, symmetric periodic orbit is computed by implementing the generalized differential corrections procedure described in Section 3.6. A

periodic orbit in the planar CR3BP requires specification of five variables: the four components of an initial state, $\bar{x}^* = [x_0, y_0, \dot{x}_0, \dot{y}_0]^T$, and the period, T. Introducing constraints at the beginning of the trajectory, however, reduces the number of free variables. Consider an initial guess that has been obtained for a symmetric periodic orbit. Since periodic orbits that are symmetric cross the x-axis implying at least two perpendicular crossings, two initial boundary constraints are applied: $\dot{x}_0 = 0$ and $y_0 = 0$ [6]. The $\bar{V}$ vector is accordingly defined with the three remaining free variables and a slack variable, β:

$$\bar{V} = \begin{bmatrix} x_0 \\ \dot{y}_0 \\ T \\ \beta \end{bmatrix} \tag{3.23}$$

where β is used to control the direction of the x-axis crossing, thereby effectively constraining the direction of motion of the orbit [30]. Together with the two initial constraints, the free variables uniquely define a natural solution in the planar CR3BP.

To identify a trajectory as periodic, a periodicity constraint must be enforced in all four states at the endpoint. Recall, however, that periodic orbits occur in dense sets in the CR3BP, producing a one-parameter family of orbits. Thus, to target a periodic orbit at a desired value of the energy constant, the constant of motion is introduced as an additional boundary constraint at the final time. Given that the numerical integration process is accurate, specifying the constant of motion at the end of a natural trajectory enforces that constraint along the entire path. Additionally, the direction of the orbital velocity is imposed by defining an inequality constraint on the y-component of the velocity. This boundary condition is transformed into an equality constraint using the slack variable, β.

Since there are four free variables, the definition of more than four boundary conditions over-constrains the problem: the constraints imposed at the endpoint of the trajectory arc must, therefore, be independent. Accordingly, the number of constraints must be equal to or less than the number of free variables. In this targeting

scheme, two of the explicit periodicity constraints are removed when the energy constant and direction of motion are specified. Thus, the scalar boundary conditions are expressed in terms of the free-variables and recast into the four-dimensional error vector, $\bar{F}$:

$$\bar{F} = \begin{bmatrix} y(T) \\ \dot{x}(T) \\ \dot{y}(T) \pm \beta^2 \\ C(x(T), y(T), \dot{x}(T), \dot{y}(T)) - C_d \end{bmatrix} \tag{3.24}$$

where C_d is the desired energy constant and $C(x(T), y(T), \dot{x}(T), \dot{y}(T))$ is the energy constant evaluated at the end of the trajectory. The first two elements of $\bar{F}$ indicate that a perpendicular intersection of the map is desired at the end of the arc, to match the perpendicular crossing at its initial state. The sign in the third element of $\bar{F}$ is selected to yield the desired direction of motion: if a positive crossing of the map is desired at $\bar{x}(T)$, a negative coefficient is selected for β^2, and vice versa.

Given the definitions for the elements of the free variable and constraint vectors, the Jacobian matrix is computed and an update equation specified using equation (3.18). This matrix is evaluated from the following:

$$D\bar{F}(\bar{V}) = \begin{bmatrix} \frac{\partial y(T)}{\partial x_0} & \frac{\partial y(T)}{\partial \dot{y}_0} & \frac{\partial y(T)}{\partial T} & \frac{\partial y(T)}{\partial \beta} \\ \frac{\partial \dot{x}(T)}{\partial x_0} & \frac{\partial \dot{x}(T)}{\partial \dot{y}_0} & \frac{\partial \dot{x}(T)}{\partial T} & \frac{\partial \dot{x}(T)}{\partial \beta} \\ \frac{\partial (\dot{y}(T) \pm \beta^2)}{\partial x_0} & \frac{\partial (\dot{y}(T) \pm \beta^2)}{\partial \dot{y}_0} & \frac{\partial (\dot{y}(T) \pm \beta^2)}{\partial T} & \frac{\partial (\dot{y}(T) \pm \beta^2)}{\partial \beta} \\ \frac{\partial (C - C_d)}{\partial x_0} & \frac{\partial (C - C_d)}{\partial \dot{y}_0} & \frac{\partial (C - C_d)}{\partial T} & \frac{\partial (C - C_d)}{\partial \beta} \end{bmatrix} \tag{3.25}$$

To compute this matrix during each iteration, the STM is exploited. Substituting elements of the numerically determined STM, $\Phi_{mn}(T, 0) = \frac{\partial x_m(T)}{\partial x_n(0)}$ for $m, n = 1...4$, into equation (3.25), the Jacobian matrix at iteration i simplifies to:

$$D\bar{F}^i(\bar{V}^i) = \begin{bmatrix} \Phi_{21} & \Phi_{24} & \dot{y}(T) & 0 \\ \Phi_{31} & \Phi_{34} & \ddot{x}(T) & 0 \\ \Phi_{41} & \Phi_{44} & \ddot{y}(T) & \pm 2\beta \\ \frac{\partial C}{x_0} & \frac{\partial C}{\dot{y}_0} & 0 & 0 \end{bmatrix} \tag{3.26}$$

Since this Jacobian matrix is square and nonsingular, equation (3.20) is employed to iteratively update the initial guess for the vector $\bar{V}$ and, therefore, the solution. The update equation is successively applied until the l_2-norm of $\bar{F}^i(\bar{V}^i)$ at iteration i, is equal to zero to within some user-specified positive tolerance, ϵ. A trajectory that is sufficiently close to periodic satisfies the aforementioned constraints to within a nondimensional tolerance on the order of 10^{-11} to 10^{-12}.

The development of the targeting scheme is complete and is now employed to compute a planar, symmetric periodic orbit in the CR3BP. For illustration, a retrograde period-1 orbit in the exterior region at the energy level $C = 3.885149584125780$ is produced. Assume that an initial guess for a retrograde period-1 orbit is available. Since success of the first-order Newton's method requires a good initial guess, the period and slack variable are iteratively selected such that the norm of the error vector at the first iteration is less than 1. An error vector with a larger l_2-norm indicates an initial guess that is further from the true solution. Figure 3.10 features a plot of the resulting periodic orbit, which is determined after five iterations of the targeting process. In addition, a zoomed view of the beginning and end of each intermediate solution is plotted in Figure 3.11(a). With each iteration, the endpoint along the path, denoted by a large circle, is increasingly closer to the initial state. A quantitative representation of the error in satisfying the boundary conditions is displayed in Figure 3.11(b). In this figure, the base-10 logarithm of $||F^i||_2$ is plotted at each iteration; as $||F^i||_2$ approaches 0, $log_{10}(||F^i||_2)$ approaches $-\infty$. For the given initial guess, the targeting scheme quadratically converges towards a periodic orbit that satisfies the boundary conditions to within an accuracy of 10^{-13}.

A single shooting algorithm can also be used to locate and compute asymmetric periodic orbits by modifying the free variable and error vectors. However, using this algorithm to target periodic orbits (symmetric or nonsymmetric) with longer periods or many revolutions about one of the primaries may result in poor convergence, or divergence. This problem is overcome by introducing constraints at multiple intermediate nodes and locating a solution using a multiple shooting algorithm.

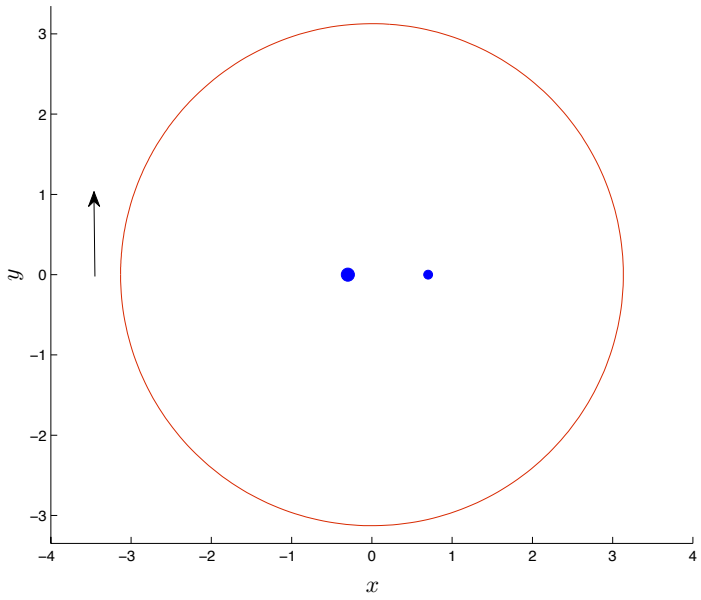

Figure 3.10. Retrograde period-1 orbit in the CR3BP at $C = 3.885149584125780$.

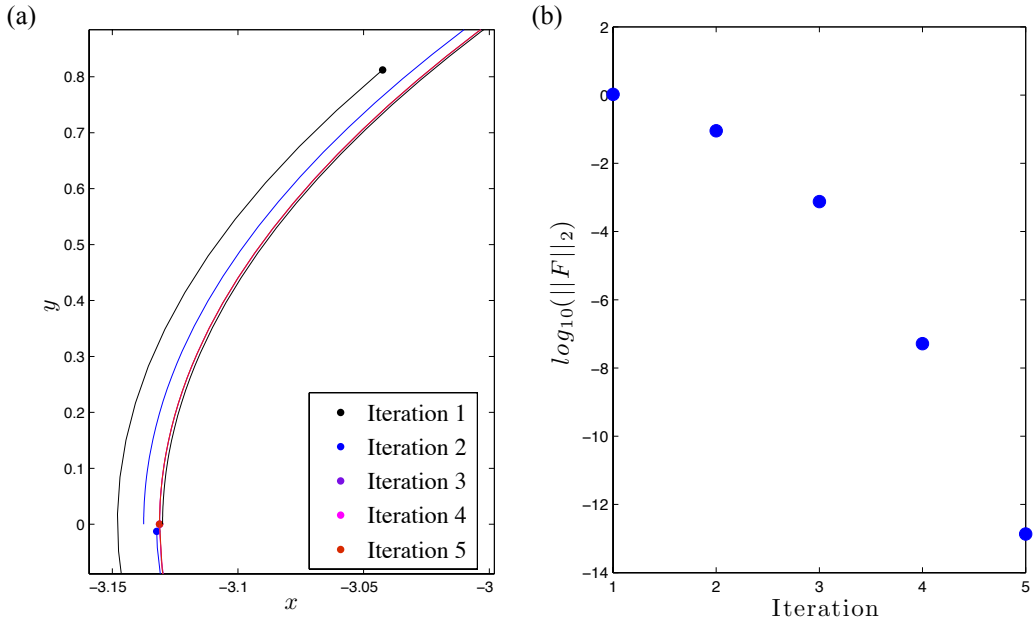

Figure 3.11. Illustration of error in intermediate solutions during the five iterations of the targeting scheme.

3.6.2 Variable-Time Multiple Shooting Algorithm

A period-q orbit with an orbital period much larger than the period of the primary orbit is targeted effectively and accurately using a multiple shooting algorithm. Targeting orbits with long periods using variable-time multiple shooting offers numerous advantages over a single shooting targeting scheme. In particular, in a dynamically or numerically sensitive region in the phase space, a small error in an initial state may grow significantly over a long integration time. In some scenarios, the initial guess may deviate sufficiently far from the desired periodic orbit to cause a single shooting algorithm to diverge. In contrast to the single shooting algorithm in Section 3.6.1, a multiple shooting scheme employs intermediate nodes that are distributed along an initial guess. Simultaneously integrating the states at each of these nodes to produce multiple arcs results in an initial guess that remains in the vicinity of the desired solution. This concept is sketched in Figure 3.12 for an arbitrary periodic orbit split into seven arcs. The states at the nodes that are represented as red dots form the

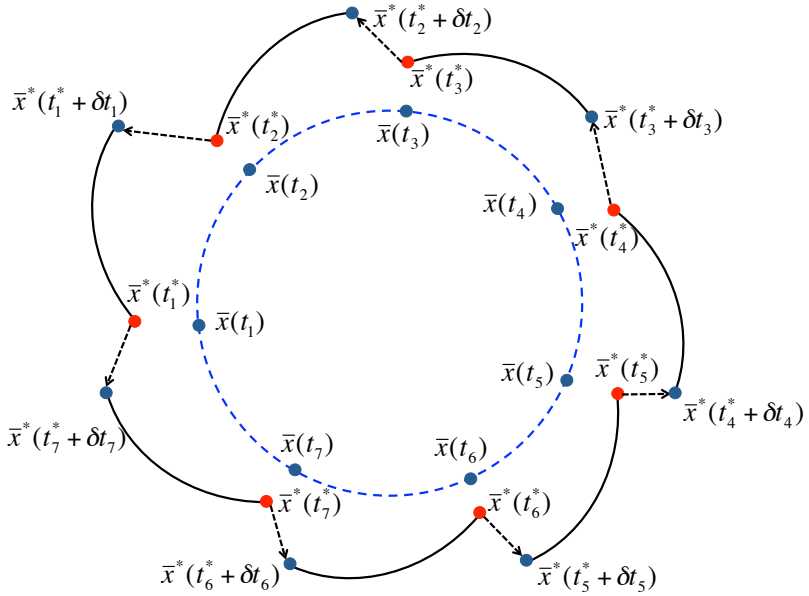

Figure 3.12. Illustration of variable time multiple shooting formulation to target a periodic orbit.

initial guess, labeled $\bar{x}^*(t_i)$, for $i = 1...7$. Integrating each four-dimensional node state for a time δt_i yields seven arcs, each with endpoints $\bar{x}^*(t_i + \delta t_i)$ that are denoted by blue dots. The discontinuities between the beginning and end points of neighboring arcs are identified by the dashed arrows. A multiple shooting algorithm eliminates these discontinuities to within a specified tolerance, and the corrected states, $\bar{x}(t_i)$, lie on the nearby periodic solution, represented as a blue dashed path.

An additional benefit of using a multiple shooting scheme is the reduction of error in the numerically-computed monodromy matrix. Recall that the monodromy matrix represents the sensitivity of $\bar{x}^*(t_n)$, a state along the reference path, with respect to changes in an initial state $\bar{x}^*(t_0)$. Using the decomposition property of the STM in equation (3.8), the monodromy matrix is computed as the product of the STMs of n intermediate arcs along a path or arc, integrated for a time $\delta t_i < (t_{i+1} - t_i)$.The determinant of the assembled monodromy matrix may be closer to 1 than the determinant of the monodromy matrix calculated through continuous integration of the STM over a complete orbital period, $t_n - t_0$.

The multiple shooting algorithm as formulated here targets a period-q orbit (for $q > 1$) using q nodes, each with a y-component equal to zero. Specification of the initial state and the integration time along each arc, therefore, contributes four elements to the free variable vector, $\bar{V}$:

$$\bar{V} = \begin{bmatrix} x^*(t_1) \\ \dot{x}^*(t_1) \\ \dot{y}^*(t_1) \\ \delta t_i \\ \vdots \\ x^*(t_q) \\ \dot{x}^*(t_q) \\ \dot{y}^*(t_q) \\ \delta t_q \end{bmatrix} \tag{3.27}$$

Combined with the q scalar constraints, $y^*(t_i) = 0$, these $4q$ free variables uniquely define a set of q arcs.

To target a trajectory that is continuous and periodic, constraints are enforced between neighboring arcs. A continuity constraint of the form:

$$\bar{x}^*(t_i + \delta t_i) - \bar{x}^*(t_{i+1}) = \bar{0}$$

could be applied to all four states corresponding to each of the intermediate nodes, where $i = 1...q-1$. However, to maintain the same energy level as determined by the state elements at each node, the x-component of the continuity constraint is replaced with a constraint on the constant of motion as evaluated at the origin of the arc. Additionally, for these arcs to converge to a periodic solution at a desired energy level, an explicit continuity constraint is applied to join the endpoint of the final arc and the first node. Thus, the constraint vector, $\bar{F}$, takes the form:

$$\bar{F} = \begin{bmatrix} y^*(t_1 + \delta t_1) \\ \dot{x}^*(t_1 + \delta t_1) - \dot{x}^*(t_2) \\ \dot{y}^*(t_1 + \delta t_1) - \dot{y}^*(t_2) \\ C(\bar{x}^*(t_1)) - C_d \\ \vdots \\ x^*(t_q + \delta t_q) - x^*(t_1) \\ y^*(t_{q-1} + \delta t_{q-1}) \\ \dot{x}^*(t_q + \delta t_q) - \dot{x}^*(t_1) \\ \dot{y}^*(t_q + \delta t_q) - \dot{y}^*(t_1) \end{bmatrix} \tag{3.28}$$

where C_d is the desired value of the energy constant corresponding to the periodic orbit. These constraints are analytical expressions of the free variables, and are, therefore, straightforwardly differentiated to determine the Jacobian matrix. Given that the number of constraints equals the number of free variables, the update equation in equation (3.20) is applied at each iteration of the targeting scheme.

The multiple shooting algorithm is tested on a retrograde period-5 orbit in the CR3BP, at an energy level equal to $C_d = 3.930149584125778$. In Figure 3.13(a), an

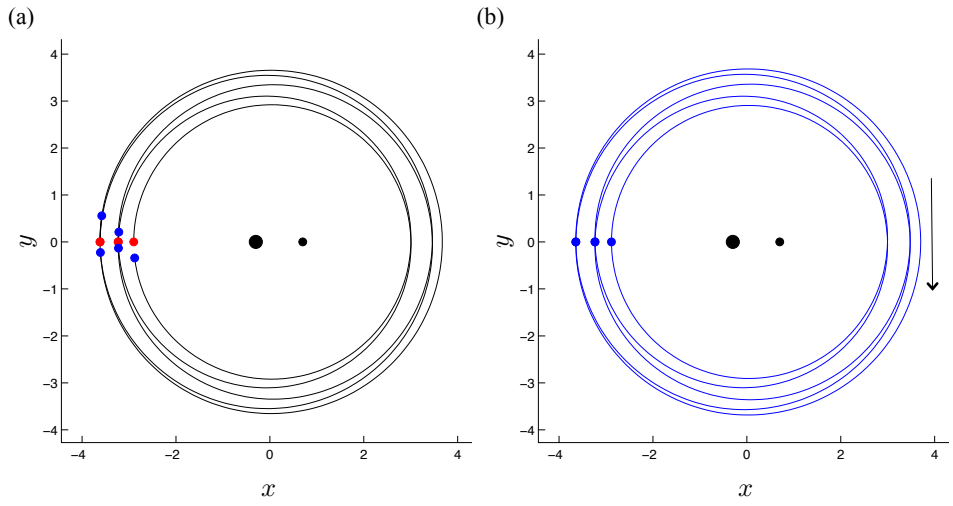

Figure 3.13. Demonstration of variable-time multiple shooting to target a period-5 orbit at $C_d = 3.930149584125778$, with $k = 0$.

initial guess comprised of five arcs is plotted in black. The initial nodes associated with these arcs are represented as red dots, while the endpoints along the arcs are represented as blue dots. Since the initial and final points corresponding to the five arcs do not coincide, this initial guess is clearly discontinuous. After nine iterations, the algorithm converges to the periodic orbit plotted in blue in Figure 3.13(b), with a black arrow representing the direction of motion along the path. The initial guess in this example has an error vector with an l_2-norm, $||F||_2 \approx 0.96$; this level of the error reflects an initial guess that is significantly far from the true solution. Thus, the algorithm completes a few iterations before the guess is sufficiently close to the true solution for quadratic convergence to be observed. Given a more accurate initial guess, the algorithm converges to a solution in less than five iterations. The converged solution satisfies the continuity, periodicity and energy constraints to within a tolerance on the order of 10^{-13}. Additionally, the determinant of the final monodromy matrix is equal to 1 with an accuracy on the order of 10^{-12}. This converged solution, therefore, represents a period-5 orbit with a period of approximately 37.7956 nondimensional time units.

3.7 Continuation

A single periodic solution that belongs to a continuous, one-parameter family in the CR3BP can be exploited to obtain information representing other members of the family. Assuming that the parameter representing a family of orbits evolves smoothly, various continuation methods are available for determining the solutions comprising each family, including natural parameter continuation and psuedo-arc length continuation. As depicted in Figure 3.14(a), natural parameter continuation assumes knowledge of a periodic solution described by the free-variable vector, $\bar{V}$, at some value of a natural, frequently physical, parameter, p^*. This known solution, represented as a blue dot located along the one-parameter curve, is used as an initial guess for the orbit within the family that possesses a value of the natural parameter equal to $p^* + \delta p$. The actual solution at this value of the natural parameter is represented as a red dot. Since the convergence of a solution using Newton's method requires a good initial guess, the success of natural parameter continuation depends upon the step size, δp, that is appropriate for the local slope of the solution curve. Psuedo-arc length continuation, however, incorporates knowledge of the gradient of this curve at p^* to predict the nearby solution. As sketched in Figure 3.14(b), the initial guess is constructed by moving along the tangent vector by a distance δs. In fact, this tangent vector lies in the null-space of the Jacobian matrix of the corrections algorithm used at each iteration. Accordingly, pseudo-arclength continuation often exhibits better convergence than true natural parameter continuation. For this reason, pseudo-arclength parameter continuation is used within this investigation, employing the multiple shooting approach of Section 3.6.2 to correct the solution predicted at each step.

As an example, the retrograde period-1 orbit computed in Section 3.6.2 is used as an initial solution for the pseudo-arclength continuation method. This periodic orbit lies in the exterior region in the CR3BP. Twenty members of the same family are plotted in Figure 3.15, each with energy constants, C, in the range from

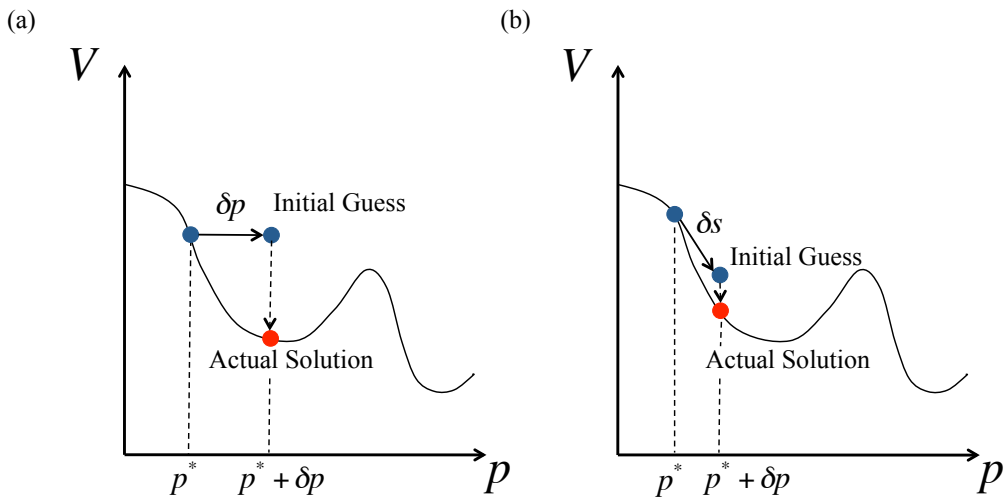

Figure 3.14. Illustration of (a) natural parameter continuation and (b) pseudo-arclength continuation process.

3.885149584125778 to 5.704695183648688. The black arrow depicts the direction of motion along the orbits, while the blue arrow signifies the direction of an increasing energy constant; the two primaries are indicated by the black dots. Computation of a family of periodic orbits in the CR3BP using continuation requires that the arc-length, δs, is selected based on the dynamical properties, including: the geometry of the orbits, the presence of equilibrium points in the vicinity of the solution, changes in the orbital stability along the family, and the slope of a one-parameter curve representing the family in the solution space. Since this subset of orbits along the family possesses a simple geometry that remains far from the primaries and any equilibrium points, a pseudo-arclength of $\delta s = 0.5$ nondimensional units is selected. As the shape and properties of the family of orbits evolves, the size of the arclength may be updated.

In constructing a family of periodic orbits, the targeting algorithm may sometimes fail to compute the next family member: due to divergence, the algorithm may converge to a solution belonging to another distinct family. Such behavior may occur if the step size results in an initial guess that is either too far from the true solution

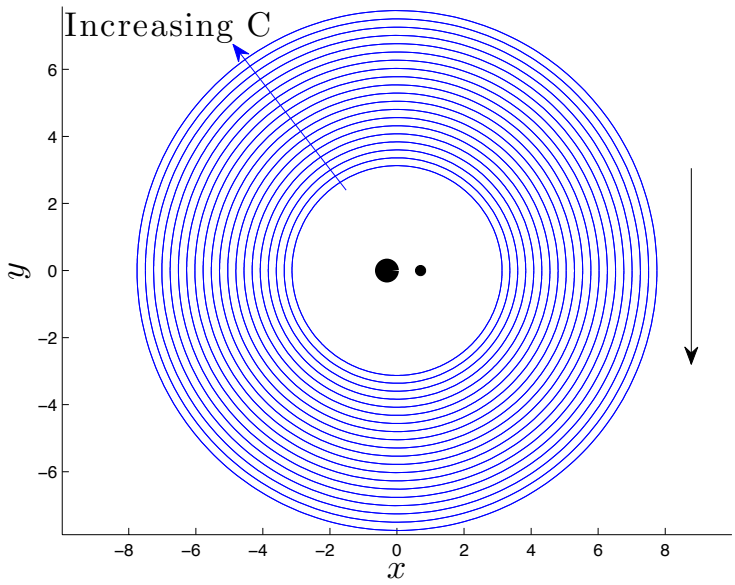

Figure 3.15. Twenty members of a family of retrograde period-1 orbits in the exterior region in the CR3BP.

for convergence, or the new predicted initial guess is actually closer to solutions in another family. An adaptive step size can be implemented, reducing the arc-length if the targeting algorithm does not converge within a given number of iterations. Alternatively, the numerical computation of a periodic orbit at a given energy level may not be successful because the family has terminated. Recording and analyzing the stability of each orbit during the continuation process can aid in ascertaining whether a family has terminated or evolved to another family. This check can also be performed through visualization of the dynamical environment in the vicinity of the periodic orbits along the family. In fact, an appropriately constructed discrete-time system that preserves periodicity may elucidate the stability and form of the periodic solutions of interest.

4. DISCRETE TIME MAPPING IN THE CIRCULAR RESTRICTED THREE-BODY PROBLEM

The search for periodic and quasi-periodic solutions in the CR3BP requires significantly more computational effort than, for example, the determination of equilibrium points. In fact, for a given value of the energy constant, C, an infinite number of planar initial conditions $[x, y, \dot{x}, \dot{y}]^T$ exist. Since the CR3BP is nonintegrable, ordered behavior may give way to chaotic motion at some energy levels. Consequently, small perturbations in an initial state may result in trajectories that depart the vicinity of a reference path. Thus, in the absence of a priori knowledge of the phase space and techniques from dynamical systems theory, it is challenging to search for solutions with desired characteristics. Reformulating the system of differential equations into a discrete-time map reduces the dimension of the problem and offers a clearer visualization of the dynamical structure. The resulting maps are straightforwardly employed to identify and analyze regions of stable, unstable and chaotic behavior.

4.1 Poincaré Maps

To create a Poincaré map from a system of differential equations, the concept of a surface of section is introduced. Consider the system of four scalar autonomous, nonlinear differential equations represented in vector form:

$$\dot{\bar{x}} = \bar{f}(\bar{x})$$

with initial conditions $\bar{x}_0 = [x_0, y_0, \dot{x}_0, \dot{y}_0]^T$. Integrating these differential equations forward from a time t_0 to t produces a solution, $\bar{x}(\bar{x}_0, t)$, or equivalently, a continuous-time flow, $\phi_t(\bar{x}_0)$ [20]. The four-dimensional phase space of the flow is reduced to three dimensions by considering initial conditions at a given energy: if three of the

four coordinates $[x, y, \dot{x}, \dot{y}]^T$ are known, the fourth coordinate is determined from the expression for the energy constant [21]. Then, a smooth surface of section, Σ, is selected such that the flow is transverse to the hyperplane [20]. As illustrated in Figure 4.1, the flow through $\bar{x}_0$ is propagated forward or backward in time. Its first intersection with the surface of section is denoted the Poincaré map, P, as:

$$\bar{x}_0 \rightarrow P(\bar{x}_0) \tag{4.1}$$

Subsequently, the n-th intersection of the flow with the surface of section is denoted $P^n(\bar{x}_0)$, crossing the surface of section in either the positive or negative direction. A two-sided map records crossings in both the positive and negative directions while a one-sided map records only crossings in one direction: an important distinction that is critical when defining the map [20]. Since the flow at a given energy level crosses the hyperplane transversally, the discrete time mapping P possesses a dimension of two. In comparison to the original system of continuous-time differential equations, the reduction in the dimension of the phase space significantly simplifies visualization of the flow, while preserving many of the physical properties of the continuous-time solutions that intersect the surface of section. Properties that are preserved by the mapping P include stability and periodicity. As depicted in Figure 4.1, a periodic orbit repeatedly crosses the surface of section at the intersection labeled $\bar{x}_{PO}$, exhibiting periodicity in the discrete-time mapping and is labeled a fixed point in the flow. A stable, periodic, continuous-time solution, for example, is also stable and periodic in the discrete time system.

Although there are numerous possible options for a surface of section, a physical plane in configuration space such as a section at $y = 0$ has been used extensively in the CR3BP, as many planar trajectories tend to revolve around the primaries, successively crossing the x-axis [21]. One limitation when employing a $y = 0$ surface of section, however, is that information is only retained for trajectories revolving around the primaries. Trajectories that do not cross the x-axis, such as those that tightly orbit L_4, are not preserved in the transformation between the differential equations and this particular discrete mapping. Thus, an appropriately selected surface of section retains

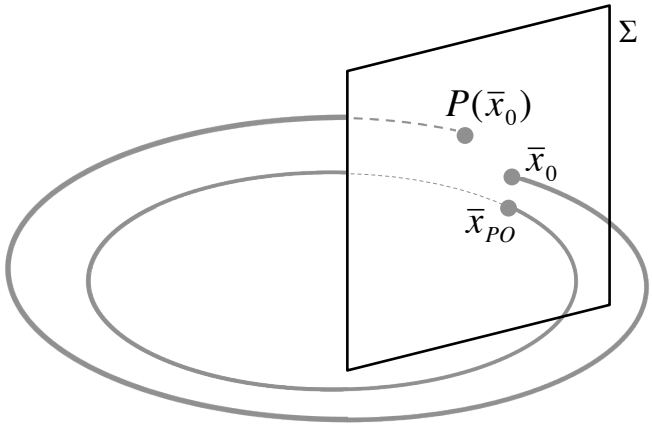

Figure 4.1. From the initial state $\bar{x}_0$ in Σ, the mapping $\bar{x}_0 \rightarrow P(\bar{x}_0)$ represents the intersection of the surface of section as the first return of the flow through $P(\bar{x}_0)$.

trajectories with the desired characteristics. Given that the MCR3BP is formulated to reduce to the CR3BP as $k \rightarrow 0$, $y = 0$ serves as a reasonable choice for a surface of section when examining a subset of the dynamics in the CR3BP. However, not all the dynamical structure is revealed.

4.2 Identification of Map Structures

An appropriately constructed, one-sided Poincaré map elucidates the form of solutions present at a particular energy level in the CR3BP and offers a qualitative assessment of their stability. Recall the three types of time-varying solutions: periodic orbits, quasi-periodic orbits, and chaotic trajectories. These trajectories appear as distinct features on a Poincaré map.

Period-q orbits repeat after every period, appearing as q points on an appropriately defined one-sided map. Two examples of the representations of periodic orbits on a Poincaré map are illustrated in Figures 4.2 and 4.3. The first figure highlights the map for a simple period-1 orbit and a period-4 orbit appears in the second figure.

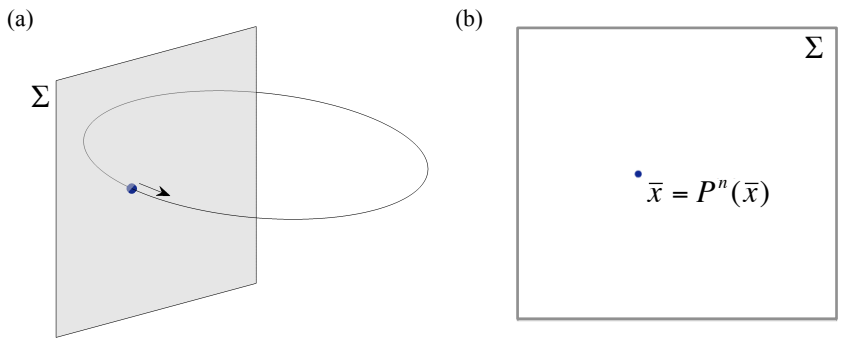

Figure 4.2. Period-1 orbit (a) intersecting a surface of section and (b) represented as a fixed point on the resulting Poincaré map.

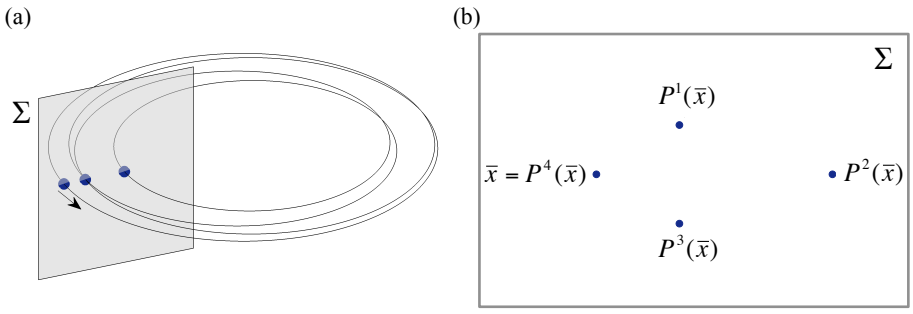

Figure 4.3. Period-4 orbit (a) intersecting a surface of section and (b) represented as four successive points on the resulting Poincaré map.

On the left in both figures, the trajectories are depicted intersecting a surface of section, Σ. These intersections are isolated and plotted on the Poincaré map on the right. Behavior near the points of intersection with the surface of section qualitatively describes the orbital stability.

If a period-q orbit is stable, it is surrounded by an infinite number of quasi-periodic orbits in its vicinity. Since a quasi-periodic orbit fills out a torus, it appears as a series of q closed curves on the map [20]. Within each of these curves lies one of the q points corresponding to the periodic orbit at the center of the torus. As an example, Figure 4.4(a) depicts the intersection of a quasi-periodic orbit with a surface of section. On a one-sided map, such as the map in Figure 4.4(b), the quasi-periodic

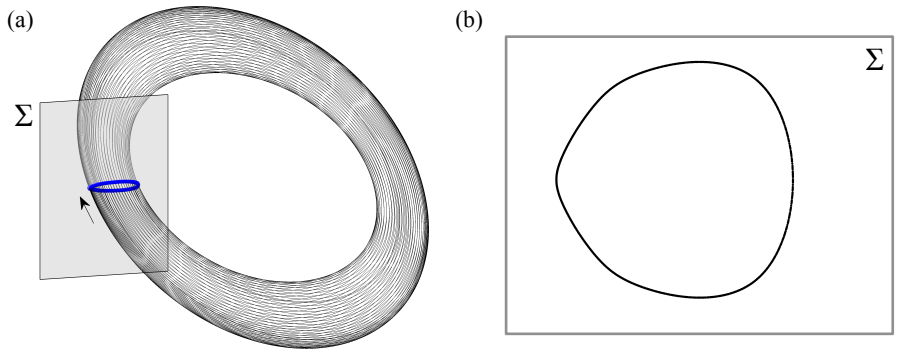

Figure 4.4. Quasi-periodic orbit (a) intersecting a surface of section and (b) represented as a closed curve consisting of successive points on the resulting Poincaré map.

orbit is represented as a single curve with a fixed point corresponding to a period-1 orbit at its center.

Since perturbations to an unstable orbit depart the vicinity of the orbit relatively quickly, unstable orbits are only identifiable on a map when they are embedded between stable islands. As illustrated in Figure 4.5, each of the q points correspond to an unstable periodic orbit that is located at an intersection of a separatrix on the map. In dynamical systems, a separatrix is a boundary between two different types of behavior, such as higher-order stable islands embedded within the two invariant curves corresponding to quasi-periodic orbits. Unstable orbits can, therefore, be identified when they lie between stable islands. When surrounded by chaos, however, unstable orbits are not associated with any discernible structures on a Poincaré map because chaotic trajectories randomly intersect the map, forming a "dusty region", as depicted in Figure 4.6 [21].

4.3 Example Map Analysis

In this investigation, Poincaré maps are used to identify stable islands of periodic and quasi-periodic motion, and to qualitatively determine their form; this process

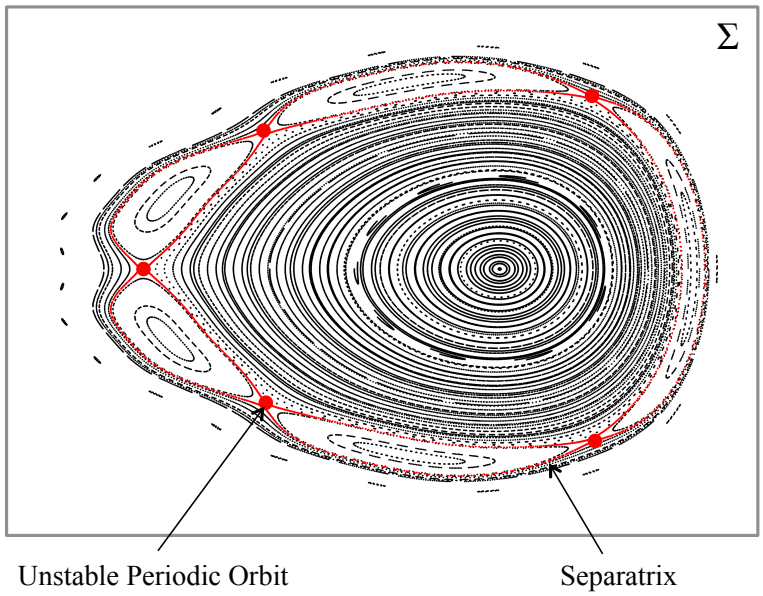

Figure 4.5. A map featuring a central stable island with embedded higher order islands. Red dots correspond to an unstable period-q orbit, located where the red separatrix intersects.

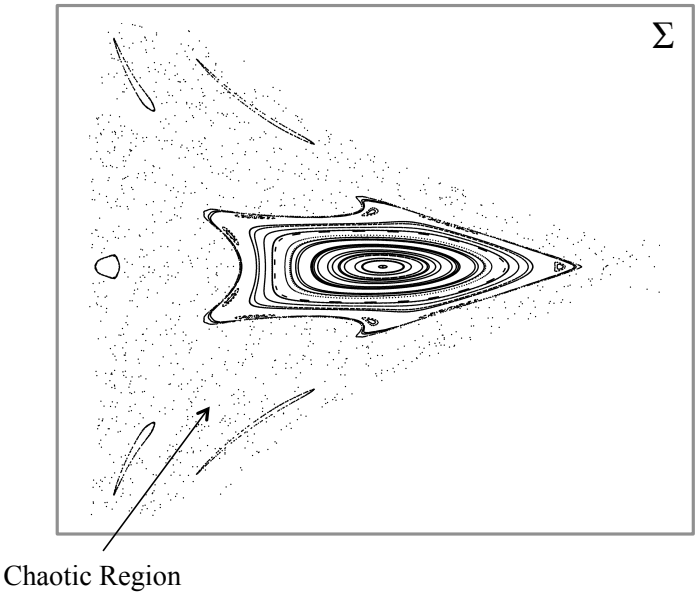

Figure 4.6. Dusty regions on a map between stable islands, corresponding to chaotic orbits.

is described for a sample map in the CR3BP for a mass ratio $\mu = 0.3$. Consider a constant of motion $C = 3.885149584125780$, a value that is just below $C(L_1)$, the energy constant evaluated at L_1. The ZVCs at this energy level are plotted in Figure 4.7, with the equilibrium points represented as red diamonds, and the primaries plotted as blue circles. Forbidden regions are shaded grey, and regions of allowable motion are white. Since the L_2 and L_3 gateways are closed at this value of the energy constant, the ZVCs reveal that P_3 can travel within the exterior region, or between the P_1 and P_2 regions; however, P_3 cannot naturally travel between all three regions in the figure.

A useful Poincaré map is then numerically constructed using initial conditions located on the $y = 0$ surface of section with a velocity perpendicular to the section, thereby possessing the form $[x, y, \dot{x}, \dot{y}]^T = [x_0, 0, 0, \dot{y}_0]^T$. These initial conditions form a one-dimensional grid along the x-axis. Given a value for x_0, the magnitude of $\dot{y}_0$ is determined from the expression for the constant of motion. The sign of $\dot{y}_0$

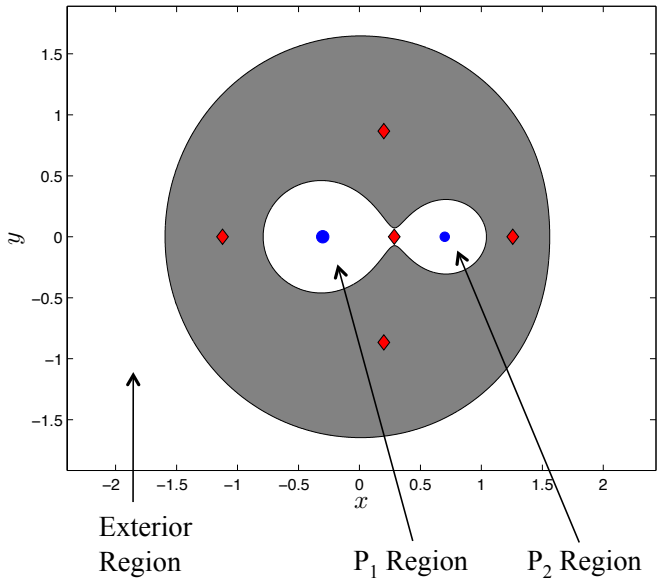

Figure 4.7. Zero velocity curves in the CR3BP at an energy level $C = 3.885149584125780$ in a system with $\mu = 0.3$.

is determined by whether the trajectories are selected to be initially prograde or retrograde; the direction of the arrows in Figure 4.8 illustrates a choice of sign for the velocity in the y-direction. Between L_1 and L_3, the direction of motion for a trajectory is defined with respect to P_1, while the direction of motion between L_1 and L_2, is defined with respect to P_2. Paths beginning in the exterior region are equivalently defined as prograde or retrograde with respect to either primary. Each initial condition, defined in the appropriate direction, is propagated for 1000 returns to the surface of section; this number of returns sufficiently fills out the invariant curves that represent higher-order quasi-periodic motion on the map. In addition, the resolution of the sets of initial conditions along the x-axis is iteratively selected to display sufficient detail within the stable islands formed on the map. The resulting Poincaré map, constructed using initial conditions with an energy constant equal to the value $C = 3.885149584125780$, is depicted in Figures 4.9 and 4.10. In Figure 4.9, a zoomed-in view of the crossings in the interior region is plotted, while Figure

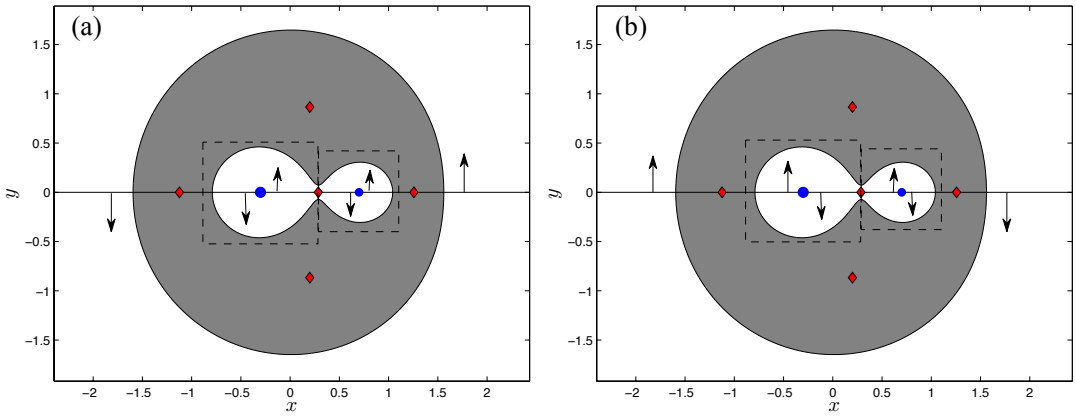

Figure 4.8. Definition of (a) prograde and (b) retrograde trajectories by region. In both figures, the direction of motion is defined with respect to P_1 in the left dotted box, and with respect to P_2 in the right dotted box. Direction of motion in the exterior region is equivalently defined from P_1 or P_2.

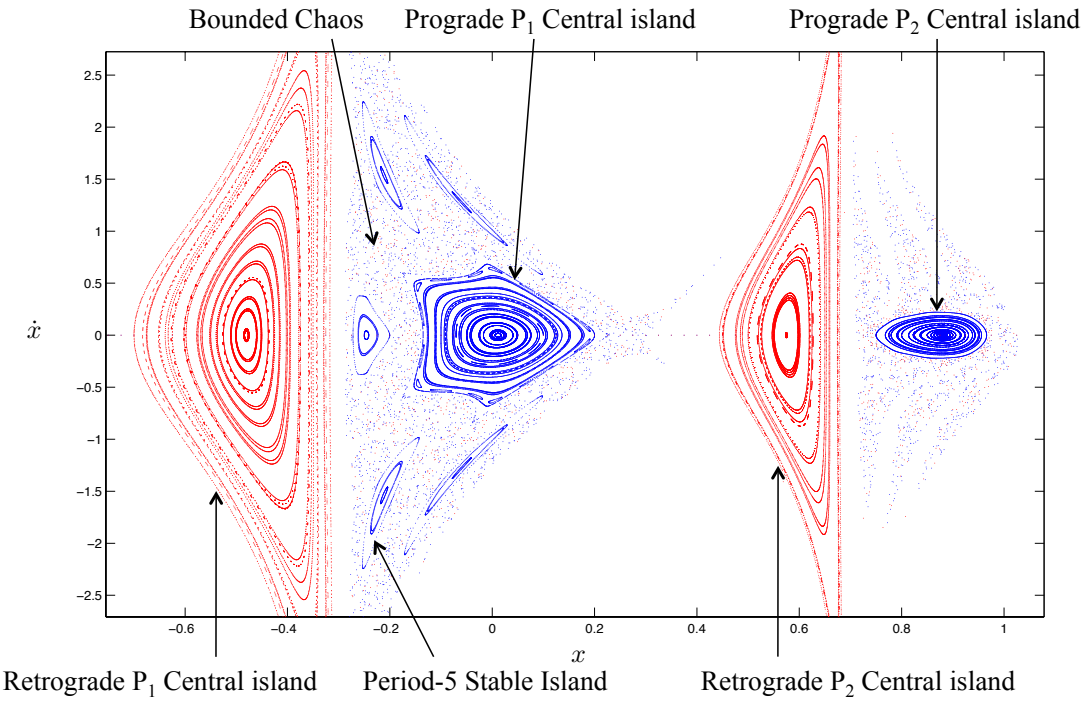

Figure 4.9. Zoomed-in view of the interior region of a Poincaré map at an energy value $C = 3.885149584125780$ for $\mu = 0.3$. A $y = 0$ surface of section is employed.

4.10 displays crossings in the exterior region. Blue points on the map correspond to trajectories that are initially prograde with respect to one of the primaries, while red intersections depict motion that is initially retrograde. Together, these figures represent a subset of the dynamics at this energy level.

Both retrograde and prograde trajectories form stable islands in the interior region; however, the primary difference between these stable zones is their maximum excursions within the phase space. As plotted in Figure 4.9, the retrograde stable islands located to the left of each of the primaries are larger than the prograde stable islands that are embedded within a sea of chaos. Since the retrograde trajectories appear in islands that are associated with a period-1 orbit, they are generally less sensitive to perturbations than the prograde trajectories. In addition, the prograde

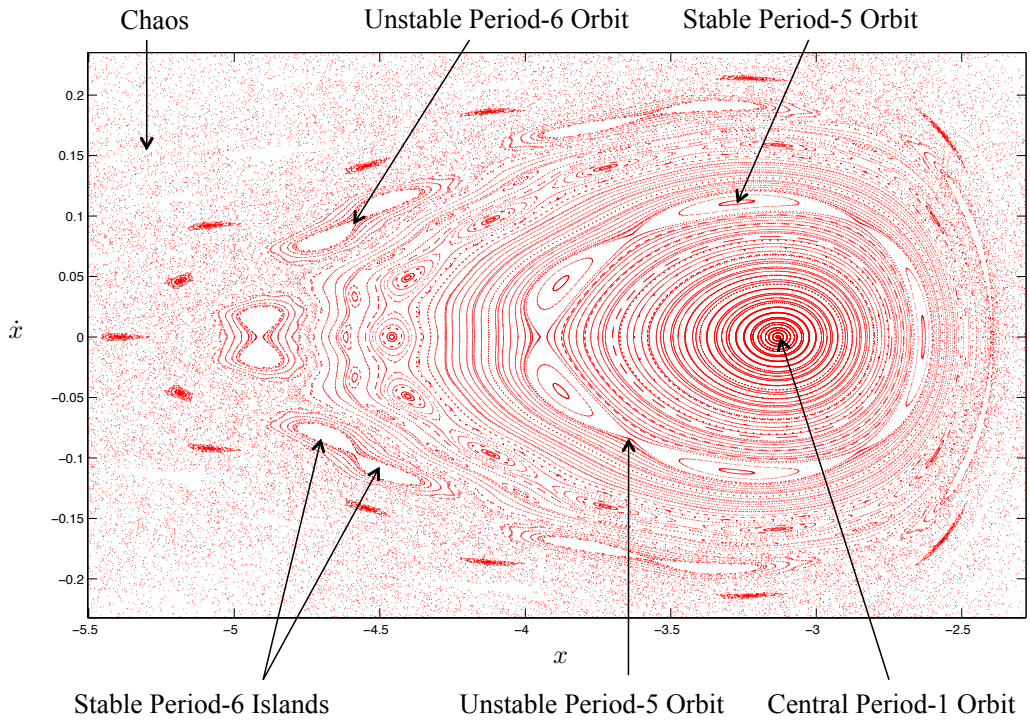

Figure 4.10. Zoomed-in view of the exterior region of a Poincaré map at an energy value $C = 3.885149584125780$ for $\mu = 0.3$. A $y = 0$ surface of section is employed.

motion about P_1 exhibits significantly-sized higher-order behavior; that is, there is a stable period-5 island that has separated from the prograde central island.

The retrograde trajectories located in the exterior region also possess an interesting dynamical structure. At the center of the central stable island depicted in Figure 4.10 lies a period-1 orbit that remains in the exterior region for all time. Within this island, higher order stable islands exist between any two invariant curves on the maps. However, only those islands that are significantly large with respect to the resolution of the Poincaré map are visible. In this subsection of the Poincaré map, for example, there is a prominent chain consisting of five islands: a stable period-5 orbit lies at the center of the concentric curves, while an unstable period-5 orbit lies between them. Additionally, beyond the last torus of the central stable island is a six-island chain embedded within unbounded chaos. The figure-eight structures in this

chain consist of two small period-6 stable islands separated by an unstable period-6 orbit. On the map in Figure 4.10, the period-6 islands feature significant white space because none of the trajectories propagated from the grid of initial conditions include intersections within these islands. Modifying the set of initial conditions to include states possessing velocities that are not perpendicular to the surface of section would reveal the stable islands contained within the white spaces.

Despite the large computational effort required to generate Poincaré maps, they are an invaluable tool for locating periodic and quasi-periodic motions. Although Poincaré maps can be used to approximately locate a periodic orbit, it is unlikely that an integrated initial condition corresponds precisely to a periodic solution. Instead, the nearby periodic orbit can be located by iteratively refining an initial guess from the map, as explained in Section 3.6. When searching for a quasi-periodic orbit, however, a point on an invariant curve is selected and integrated. Once computed, the resulting periodic and quasi-periodic orbits may be parameterized. Although many quantitative representations exist, frequency analysis is employed in this investigation.

5. FREQUENCY ANALYSIS IN THE CIRCULAR RESTRICTED THREE-BODY PROBLEM

Given their toroidal geometry, quasi-periodic orbits, introduced in Section 3.2, are characterized by the fundamental frequencies of the oscillatory motion in each of the central and transverse directions. Various properties of quasi-periodic orbits can be identified from the fundamental frequencies and some significant characteristics can be deduced. Thus, these frequencies can directly represent: the presence of resonant orbits; a qualitative evaluation of the orbital stability; an estimate of the orbital period (to within an integer ratio); and, through either the number of map crossings of a periodic orbit or the number of stable islands on a map, imply the existence of quasi-periodic orbit (to within an integer ratio). Frequency analysis is, therefore, a solid basis from which to explore the influence of three-body interactions on the form and prevalence of ordered motion in the MCR3BP.

One approach to determine the two fundamental frequencies corresponding to a quasi-periodic orbit involves computing a truncated normal form of the dynamical structure relative to a reference solution in the MCR3BP such as an equilibrium point or a periodic orbit [31]. This process involves numerically approximating the true dynamics using a truncated series expansion, allowing for direct computation and manipulation of the two fundamental frequencies of a quasi-periodic orbit, rather than their linear combinations. Despite this inherent advantage, computing accurate trajectories from the normal forms can require that the series expansion be computed up to a large degree, posing many computational challenges, including computational time and accuracy.

An alternative numerical approach to frequency analysis, which is adopted in this investigation, is based on Laskar's Numerical Analysis of the Fundamental Frequency

(NAFF algorithm) [14]. Laskar's method decomposes a trajectory, integrated for a finite time, into a finite set of linear combinations of the fundamental frequencies. An initial guess for each frequency and its amplitude is generated from a Fourier transform on a state component that comprises the complete trajectory that sufficiently reflects the fundamental frequencies. A differential corrections algorithm is then employed to iteratively update the initial guess for each sinusoidal wave until the trajectory is sufficiently reconstructed from the dominant linear combinations of its two fundamental frequencies. From an implementation perspective, the NAFF algorithm requires less memory and computational time than the construction of the normal form for the dynamical topology in the vicinity of a periodic orbit. For this reason, Laskar's method is employed in this investigation.

5.1 Frequency Decomposition using the Fourier Transform

5.1.1 Continuous Fourier Transform

Prior to a precise description of Laskar's method for decomposing a trajectory into its dominant frequencies, the Fourier transform is derived and explored originating with a Fourier series expansion. First consider a continuous, periodic function, $g(t)$, that is expressed using a Fourier series in rectangular form such as:

$$g(t) = A_0 + \sum_{m=1}^{\infty} \left(A_m \cos(2\pi m \omega_0 t) + B_m \sin(2\pi m \omega_0 t) \right) \tag{5.1}$$

where A_m and B_m are, respectively, the coefficients of the cosine and sine components for the m-th multiple of the fundamental frequency, ω_0, and the period is calculated as $T = 1/\omega_0$. This function, $g(t)$, may also be represented in complex coordinates as:

$$g(t) = \sum_{m=-\infty}^{\infty} C_m e^{i2\pi m \omega_0 t} \tag{5.2}$$

The summation in this expression spans both positive and negative frequencies, $\pm\omega$. Two frequencies of the same magnitude and opposite sign possess contributions that

are identical in amplitude, but shifted in phase. Applying Euler's theorem, the rectangular coefficients, A_m and B_m, are related to the complex coefficients, C_m and C_{-m}, for $m = [0, \infty)$, by the following change of variables:

$$A_m = \frac{1}{2}(C_m + C_{-m})$$
$$B_m = \frac{1}{2}(C_{-m} - C_m)i$$

Under this transformation, the amplitude of each sinusoidal wave is invariant. Consequently, the concepts are more easily developed and explored in complex coordinates for the purpose of simplifying the resulting expressions. The examples in this section and the practical implementation described later, however, use rectangular coordinates due to the intuitive impact that changes in sine and cosine coefficients render on the resulting sinusoidal wave.

If the parameters that describe the sinusoidal waves comprising $g(t)$ are not known, the frequencies and their coefficients are employed to represent the original function in the frequency domain. First, the fundamental frequency is straightforwardly calculated as the inverse of the period of $g(t)$. Next, the coefficient C_m corresponding to the frequency $\omega_m = m\omega_0$ is evaluated by rearranging the Fourier series expansion in equation (5.2), resulting in the following relationship:

$$C_m = \frac{1}{T}\int_{-T/2}^{T/2} g(t)e^{-i2\pi m\omega_0 t}dt \tag{5.3}$$

which is valid for all integers $m = (-\infty, \infty)$. Each coefficient and frequency combination, (C_m, ω_m), represents a single sinusoidal wave contribution to $g(t)$. Together, the set of combinations (C_m, ω_m), for all values m, represent the function $g(t)$ in the frequency domain.

To illustrate the correlation between the time and frequency representations, an arbitrary periodic function, $g_1(t)$, is transformed from the time domain into the frequency domain. The sample function is defined in rectangular form as:

$$g_1(t) = 0.25\cos(2\pi\frac{1}{3}t) + 0.6\sin(2\pi\frac{1}{3}t)$$

Since the fundamental frequency corresponding to this function is $\omega_0 = \frac{1}{3}$, the period is equal to 3. By inspection of this expression, the coefficients A_1 and B_1 are clearly equal to 0.25 and 0.6, respectively. In Figure 5.1(a), this function is plotted in the time domain for three periods, while its representation in the frequency domain is displayed in Figure 5.1(b). Along the vertical axis in Figure 5.1(b), the amplitude $G_1(\omega_m) = \sqrt{(A_m^2 + B_m^2)}$ is plotted for each positive frequency, ω_m. Accordingly, the location of each spike along the x-axis indicates a frequency component present in the analyzed function, while its height corresponds to the amplitude of the sinusoidal wave. Analyzing $G_1(\omega)$, there is one spike located at the frequency $\omega_0 = \frac{1}{3}$ with a height equal to the amplitude of the sinusoid, $\sqrt{(0.25^2 + 0.6^2)} = 0.65$. The original function, $g_1(t)$, is recovered by substituting ω_0, A_1 and B_1 into the Fourier series in equation (5.1). Thus, this simple example demonstrates the correlation between the time and frequency domains.

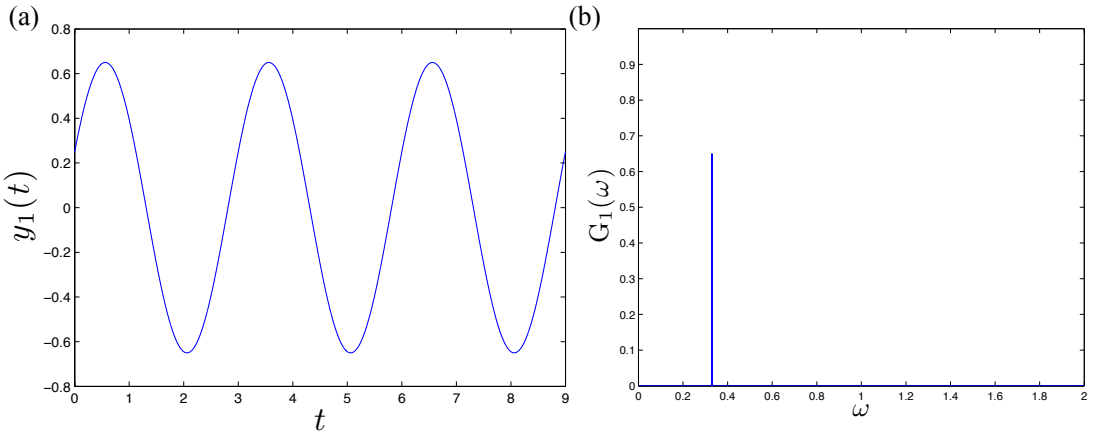

Figure 5.1. Representations of $g_1(t) = 0.25\cos(2\pi\frac{1}{3}t) + 0.6\sin(2\pi\frac{1}{3}t)$ in the (a) time domain and (b) frequency domain.

A nonperiodic function, $y(t)$, can also be represented in the frequency domain. Since $y(t)$ does not repeat, it is considered a periodic function with an infinite period. Analyzing equation (5.3) in the limit as $T \to \infty$, the set of frequencies, $\omega_m = m\omega_0$

for $m = (-\infty, \infty)$, approaches a continuous spectrum. The integral in the resulting expression is used to define the complex Fourier Transform, $Y(\omega)$:

$$Y(\omega) = \int_{-\infty}^{\infty} y(t) e^{-i2\pi\omega t} dt \tag{5.4}$$

Since equation (5.4) is derived from the expression for the individual coefficients in the Fourier series expansion, the continuous Fourier Transform, $Y(\omega)$, is used to represent $y(t)$ in the frequency domain.

5.1.2 Discrete Fourier Transform

Each of the numerically integrated trajectories in this investigation are only defined at a finite set of times, yielding discrete time-dependent functions. Since equation (5.4) assumes that $y(t)$ is a continuous function, a Discrete Fourier Transform (DFT) is also required. Assume that the continuous function $y(t)$ is sampled at N equally-spaced time intervals of length Δt, where N is assumed to be even. Each point along the function, sampled at $t_n = n\Delta t$, possesses a value $\tilde{y}(n)$ corresponding to the time indices $n = 0, 1, ...N-1$. Together, these samples form a discrete function that is expressed as a discrete Fourier series expansion in the form:

$$\tilde{y}(n) = \sum_{m=-N/2}^{N/2} \tilde{C}_m e^{i2\pi\omega_m t_n} \tag{5.5}$$

where $\tilde{C}_m$ is the complex coefficient characterizing the sinusoidal wave with frequency $\omega_m = \frac{m}{N\Delta t}$. Each complex coefficient is computed by discretizing equation (5.3), yielding the relationship:

$$\tilde{C}_m = \frac{1}{N} \sum_{n=0}^{N-1} \tilde{y}(n) e^{-i2\pi mn/N} \tag{5.6}$$

where the frequency index, m, spans the integer range $[-N/2, N/2]$. Extracting the summation, the DFT is then defined as:

$$\tilde{Y}(m) = \sum_{n=0}^{N-1} \tilde{y}(n) e^{-i2\pi mn/N} \tag{5.7}$$

corresponding to the frequency, $\omega_m = \frac{m}{N\Delta t}$. This expression, representing the discrete form of equation (5.4), transforms the N samples, $\tilde{y}(n)$, in the time domain into the N values of $\tilde{Y}(m)$ in the frequency domain. The DFT is, therefore, used to decompose a set of discrete samples into their frequency representation.

5.2 Numerical Implementation of the Discrete Fourier Transform

Numerically computing the DFT corresponding to a discrete function of N samples requires $O(N^2)$ operations; for a large number of samples, computing the DFT can be computationally time-consuming. As an alternative, a well-known algorithm, the Fast Fourier Transform (FFT), is frequently employed to more efficiently represent the function. Consider, as an example, the Cooley-Tukey FFT algorithm. Computation of the DFT is still based on equation (5.7), but the algorithm exploits the Danielson-Lanczos lemma to recursively reduce the problem of computing an N-dimensional DFT into two $N/2$-dimensional DFTs [28]. The resulting DFTs are combined and rearranged to recover the N-dimensional DFT, reducing the operation count to $O(2N\log_2(N))$. In this investigation, an FFT algorithm significantly reduces the computational time required to decompose a trajectory, discretely sampled at $O(10^5)$ points in time, and represent the path in the frequency domain.

In practical applications, sampling a function over a finite time span introduces error into the frequency decomposition. To illustrate this concept, recall the continuous function $g_1(t)$ plotted in Figure 5.1(a). Using a sampling interval equal to $t = 0.001$, Figure 5.2 depicts $g_1(t)$ sampled for (a) 3 and (b) 30 periods. These two discrete functions, respectively denoted $\tilde{y}_1(t)$ and $\tilde{y}_2(t)$, are transformed into the frequency domain using an FFT algorithm. Compared with the continuous Fourier Transform plotted in Figure 5.1, the spike at $\omega_1 = 1/3$ now appears as a peak of finite width in each of the discrete frequency domain representations plotted in Figure 5.3(a) and (b). Comparison of $|\tilde{Y}_1(\omega)|$ and $|\tilde{Y}_2(\omega)|$ demonstrates that increasing the total sample time span reduces the width of the peak that is located near the fundamental frequency,

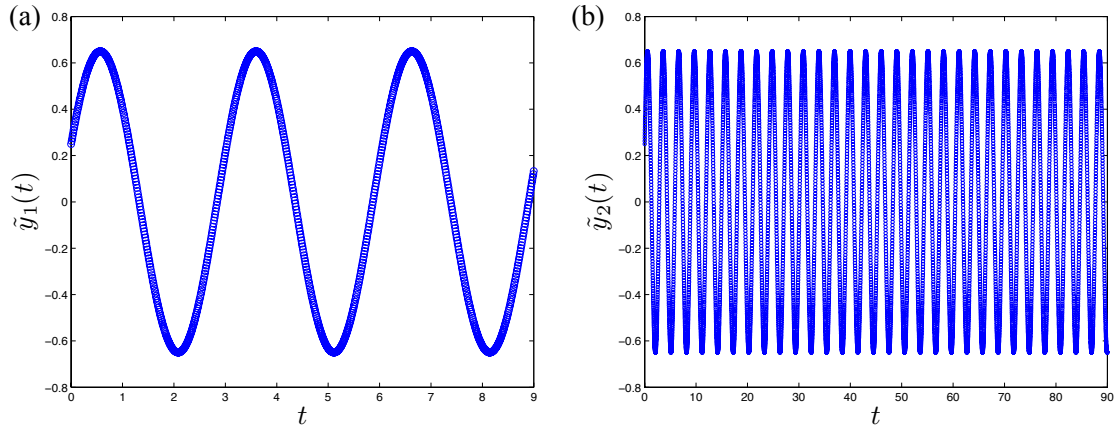

Figure 5.2. Time domain representations of $g_1(t) = 0.25cos(2\pi\frac{1}{3}t) + 0.6sin(2\pi\frac{1}{3}t)$ sampled at an interval of $\Delta t = 0.001$ for (a) 3 periods and (b) 30 periods.

$\omega = 1/3$. This observation is straightforwardly explained by considering the DFT as a discrete power spectrum: the area under the curve of $|\tilde{Y}(\omega)|$ represents the 'energy' of the signal [21]. Since the numerical DFT cannot compute frequencies precisely, the contribution from each fundamental frequency appears as a lobe of finite width in the frequency domain. A consequence is that the 'energy' incorrectly appears diffused over a range of frequencies. A fundamental frequency that is actually known to a higher accuracy reduces this diffusion, and, therefore, the width of the corresponding peak in the frequency domain. Since the size of each frequency interval is $1/(N\Delta t)$, increasing the total time span, $N\Delta t$, reduces the uncertainty in computing a fundamental frequency. Accordingly, the lobe corresponding to a single fundamental frequency approaches an impulse in the resulting frequency representation; thus, the associated parameters describing the sinusoidal wave are more accurate.

The errors induced by sampling a nonperiodic function over a finite time span can be further reduced through windowing. When the original function is multiplied by a window, the function equals a specified value at the beginning and the end of the interval; within the boundaries, the windowed function is artificially periodic.

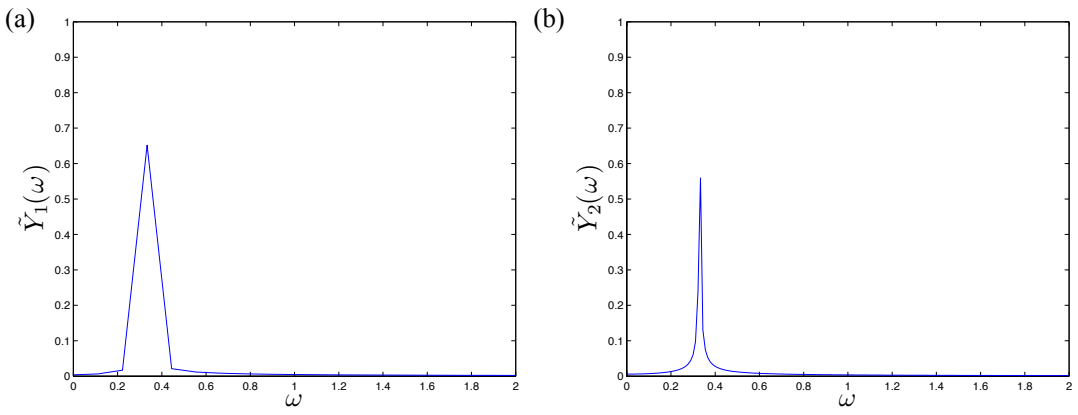

Figure 5.3. Representations of $g_1(t) = 0.25cos(2\pi\frac{1}{3}t) + 0.6sin(2\pi\frac{1}{3}t)$ in the frequency domain for a sample interval of $\Delta t = 0.001$ for (a) 3 periods and (b) 30 periods.

This tapering of the original function can increase the accuracy of the resulting frequency representation by reducing the presence of any nonperiodic behavior. As a result, windowing decreases the width of the lobes corresponding to the fundamental frequencies. Although various windows exist, a Hanning window is effective and is employed in this analysis. This windowing function is modeled by the expression:

$$w(t_n) = \frac{2}{3}\left(1 - \cos\left(\frac{2\pi t_n}{N\Delta t}\right)\right)^2 \tag{5.8}$$

at each sampled time, t_n. This window is multiplied by the sample function $g_1(t)$ and is plotted in blue in Figure 5.4. Overlaid in red is the window in equation (5.8), demonstrating the bounding properties. This window sufficiently increases the accuracy of the DFT for trajectories in the exterior region in the MCR3BP.

Sampling a nonperiodic function at equally spaced time intervals introduces error. From the Nyquist sampling theorem, a function can be accurately reconstructed if it is sampled at a frequency that is, at least, twice the highest frequency of the function itself [32]. The factor of two corresponds to the number of extrema present during one period: one minimum and one maximum. If the sampling frequency is less than this critical value, that is, the Nyquist frequency, aliasing can occur.

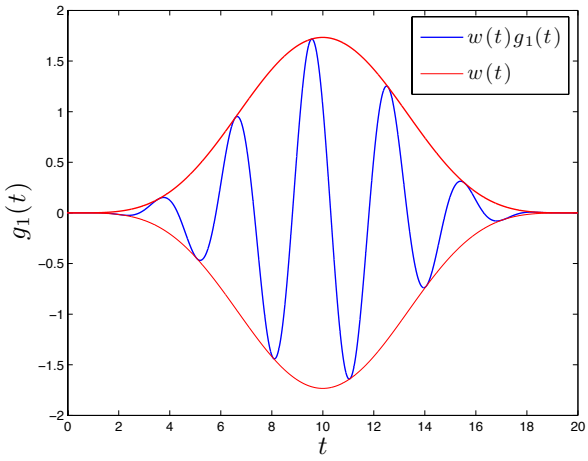

Figure 5.4. A plot of $g_1(t)$ multiplied by the windowed function in equation (5.8); overlaid in red is the Hanning window.

To demonstrate this concept, consider again the continuous function $g_1(t)$ plotted in Figure 5.1(a). The fundamental frequency corresponding to this function is, by definition, equal to $\omega_0 = 1/3$. To accurately reconstruct $g_1(t)$, the sampling frequency must be less than or equal to $2\omega_0$, corresponding to a critical sampling interval of 1.5 time units. In Figure 5.5(a), $g_1(t)$ is sampled at the Nyquist frequency. These samples are represented as blue dots. In contrast, Figure 5.5(b) features samples at a frequency equal to 0.5. Since this sampling frequency is below the Nyquist frequency, these samples can reflect a distinctly different function. One example, plotted as the red dashed curve, is $g_2(t) = 0.25\cos(2\pi\frac{1}{6}t) - 0.6\sin(2\pi\frac{1}{6}t)$. Although these two functions possess different frequencies, they intersect periodically. An insufficiently sampled function can, therefore, experience aliasing, resulting in an incorrect representation of the fundamental frequencies. To avoid this phenomenon, the sampling interval is selected by estimating of the order of magnitude of the fundamental frequencies. In this investigation, a conservative estimate is generated from the eigenvalues of the periodic orbit at the center of the primary stable island at one energy level.

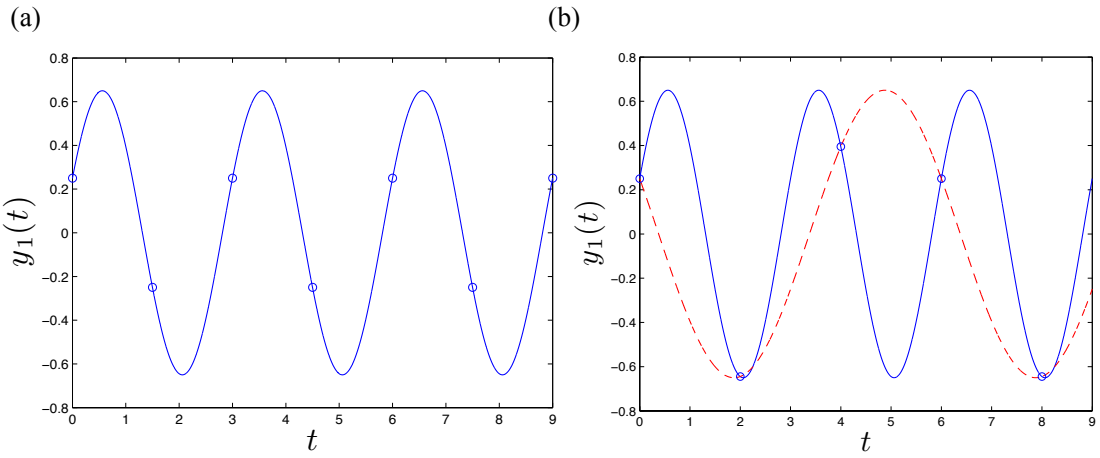

Figure 5.5. The function $g_1(t) = 0.25\cos(2\pi\frac{1}{3}t) + 0.6\sin(2\pi\frac{1}{3}t)$ sampled at an interval of (a) $\Delta t = 1.5$ and (b) $\Delta t = 2.0$. In red is the function $g_2(t) = 0.25\cos(2\pi\frac{1}{6}t) - 0.6\sin(2\pi\frac{1}{6}t)$

5.3 Numerical Frequency Refinement

The limitations of the DFT are apparent when a frequency decomposition is generated on numerically integrated trajectories in the CR3BP. As described in Section 5.1.2, the accuracy of the resulting frequency decomposition theoretically improves as the integration time increases. However, with many numerical integrators, small errors accumulate over long time spans. The integration time interval is, therefore, selected to supply sufficient resolution in the frequency spectrum, while maintaining an accurate representation of a natural trajectory in the CR3BP. For the implementation in this analysis, constraints on the computation time, as well as the allowable variation of the energy constant, limit the maximum integration time to a range between $5,000$ and $10,000$ nondimensional time units. For a trajectory propagated over this time span, the accuracy of any frequency computed via the DFT, incorporating windowing, is on the order of 10^{-4} (nondimensional time units)$^{-1}$. In the CR3BP, the fundamental frequencies corresponding to the quasi-periodic orbits within a stable island at a given energy level can vary by a smaller order of magnitude than the

accuracy obtained by the FFT. Thus, a frequency resolution of 10^{-4} is considered insufficient for this application.

To increase the accuracy of the frequency decomposition, frequency and amplitude approximations obtained from an FFT algorithm are refined using a process modeled after Laskar's NAFF algorithm. For each of the M dominant frequencies that comprise a discrete function, $\tilde{y}(t_n)$, Laskar's algorithm uses a differential corrections scheme to target the frequency, rather than the interval containing the frequency [14]. Recall from Section 5.1.1 that each frequency contribution to $y(t_n)$ is described in rectangular form as:

$$\tilde{y}_j(t_n) = A_j \cos(2\pi\omega_j t_n) + B_j \sin(2\pi\omega_j t_n) \tag{5.9}$$

where $\tilde{y_j}(t_n)$ is the sinusoidal wave corresponding to the j-th dominant frequency, ω_j, evaluated at the discrete times, t_n. Since these discrete times are the same as those in the original function, the sinusoidal waves described by the M dominant frequencies and their associated amplitudes are directly summed to approximate the original function:

$$\tilde{y}(t_n) \approx \sum_{j=0}^{M} \tilde{y}_j(t_n) = \sum_{j=0}^{M} A_j \cos(2\pi\omega_j t_n) + B_j \sin(2\pi\omega_j t_n) \tag{5.10}$$

A targeting scheme is, therefore, implemented to individually refine the parameters describing the M sinusoidal waves $\tilde{y}_j(t_n)$. As explored in Section 3.6, a differential corrections scheme is implemented using free variable and constraint vectors. In this section, these elements of a targeting algorithm are defined, along with the method to construct an initial guess.

5.3.1 Free Variable Vector

Differential corrections is employed to refine the description of a function in the frequency domain. To implement this methodology and develop an algorithm, the independent elements of the free-variable vector are available for adjustment to rep-

resent the sinusoidal wave corresponding to the j-th frequency. Three real-valued parameters, therefore, form the free variable vector, $\bar{X}$:

$$\bar{X} = \begin{bmatrix} \omega_j \\ A_j \\ B_j \end{bmatrix} \tag{5.11}$$

The sinusoidal wave constructed from the initial guess for the free variable vector is iteratively refined until it coincides with one of the sinusoidal waves comprising the original function, $\tilde{y}(t_n)$.

5.3.2 Constraint Vector

Since the frequencies in a time-dependent function are identified from the locations of the peaks in a DFT, a differential corrections scheme can be implemented to locate these peaks. Constraints can, therefore, be formulated to target the local maximum amplitude of the quantity:

$$u(\omega_j) = \frac{1}{N} \sum_{n=1}^{N} \tilde{y}(t_n) e^{-i2\pi\omega_j t_n} \tag{5.12}$$

or, equivalently, in rectangular coordinates:

$$u(\omega_j) = \frac{1}{N} \sum_{n=1}^{N} \tilde{y}(t_n) \left[\cos(2\pi\omega_j t_n) - \sin(2\pi\omega_j t_n) i\right] \tag{5.13}$$

where N is the number of points comprising the discrete function $\tilde{y}(t_n)$. As defined, the complex form of $u(\omega_j)$ resembles the DFT in equation (5.7), however ω_j is no longer a discrete variable limited by the sampling time. Differentiating the rectangular form of $u(\omega_j)$, and writing the result in terms of the independent set of free variables, produces the frequency constraint:

$$\frac{\partial u(\omega_j)}{\partial \omega_j} = \frac{2}{\sqrt{F_c^2 + F_s^2}} \left[F_c \frac{\partial F_c}{\partial \omega_j} + F_s \frac{\partial F_s}{\partial \omega_j} \right] = 0 \tag{5.14}$$

where F_c and F_s are, respectively, the real and imaginary components of the rectangular form of $u(\omega_j)$. These two variables are equal to:

$$F_c = \frac{1}{N}\sum_{n=1}^{N} \tilde{y}(t_n)\cos(2\pi\omega_j t_n)$$

$$F_s = \frac{1}{N}\sum_{n=1}^{N} \tilde{y}(t_n)\sin(2\pi\omega_j t_n)$$

Note that equation (5.14) is not the sole constraint to target the sinusoidal wave corresponding to ω_j because it does not constrain the two free variables that are amplitudes, that is, A_c and A_s. Thus, two additional constraints are incorporated. These constraint relationships equate the cosine and sine components of the DFT of the original function, $\tilde{y}(t_n)$, evaluated at ω_j, and the DFT of the approximation, $\tilde{y}_j(t_n)$. These scalar constraint equations are deduced to be of the following form:

$$\Delta F_c = \frac{1}{N}\sum_{n=1}^{N} \left[A_j\cos(2\pi\omega_j t_n) + B_j\sin(2\pi\omega_j t_n)\right]\cos(2\pi\omega_j t_n) - F_c \tag{5.15}$$

$$\Delta F_s = \frac{1}{N}\sum_{n=1}^{N} \left[A_j\cos(2\pi\omega_j t_n) + B_j\sin(2\pi\omega_j t_n)\right]\sin(2\pi\omega_j t_n) - F_s \tag{5.16}$$

If $\Delta F_c = \Delta F_s = 0$, equations (5.15) and (5.16) simplify to:

$$A_j = F_c$$

$$B_j = F_s$$

reflecting the fact that the amplitude and phase of the sinusoidal approximation, $\tilde{y}_j(t_n)$, match the amplitude and phase of the contribution to the original function from the frequency ω_j. Since the frequency and amplitude constraints are expressed in terms of the free variables, the constraints from equations (5.14), (5.15), and (5.16) are assembled to form the three-dimensional constraint vector, $\bar{F}(\bar{X})$, equal to:

$$\bar{F}(\bar{X}) = \begin{bmatrix} \frac{2}{\sqrt{F_c^2+F_s^2}}\left[F_c\frac{\partial F_c}{\partial\omega_j} + F_s\frac{\partial F_s}{\partial\omega_j}\right] \\ \frac{1}{N}\sum_{n=1}^{N}\left[A_j\cos(2\pi\omega_j t_n) + B_j\sin(2\pi\omega_j t_n)\right]\cos(2\pi\omega_j t_n) - F_c \\ \frac{1}{N}\sum_{n=1}^{N}\left[A_j\cos(2\pi\omega_j t_n) + B_j\sin(2\pi\omega_j t_n)\right]\sin(2\pi\omega_j t_n) - F_s \end{bmatrix} \tag{5.17}$$

When this constraint vector is equal to zero, the sinusoid described by $\bar{X}$ is present in the original function, $\tilde{y}(t_n)$.

5.3.3 Initial Guess for the Sinusoid Parameters

A straightforward process to generate an initial guess for the resulting differential corrections scheme is developed using the fundamental principles of frequency decomposition. The form of the approximation in equation (5.10) suggests a suitable approach to implement the frequency refinement process: after determining the contribution from $\omega_0 = 0$, each of the M dominant frequencies in $\tilde{y}(t_n)$ are computed in order of decreasing amplitude. The initial guess for the set of parameters that describe each sinusoidal wave is constructed using the FFT algorithm. Each local maximum in the Fourier transform computed by the FFT represents an approximation to a sinusoidal wave present in the original function. Once the contribution from the j-th frequency is refined using the differential corrections scheme, its corresponding sinusoidal wave is subtracted from an intermediate function, $\tilde{z}^j(t_n)$. After j iterations of the differential corrections process, this function is equal to:

$$\tilde{z}^j(t_n) = \tilde{y}(t_n) - \sum_{i=0}^{j} \left(A_i \cos(2\pi\omega_i t_n) + B_i \sin(2\pi\omega_i t_n)\right)$$

Thus, the global maximum of $\tilde{z}^j(t_n)$ after j iterations corresponds to the $(j+1)$-th largest maximum of $\tilde{y}(t_n)$. Since this process is repeated for each of the M frequencies, the closer the maximum of $\tilde{z}^M(t_n)$ is to zero, the more accurately the original function, $\tilde{y}(t_n)$, is reconstructed.

5.3.4 Summary of the Frequency Refinement Process

The frequency analysis scheme employed in this investigation combines an FFT algorithm and a differential corrections strategy. Specifically, the technique for determining the fundamental frequencies of a trajectory is summarized as follows:

1. Compute A_0 for $w_0 = 0$ using the cosine component of the DFT.

2. Set $\tilde{z}^j(t_n)$ equal to the original function $\tilde{y}(t_n)$, where $j = 0$.

3. Construct an FFT on $\tilde{z}^j(t_n)$, and locate the global maximum of the amplitude of the DFT.

4. Create an initial guess for the free variable vector in equation (5.11) from the parameters ω_j, A_j and B_j at the peak in the DFT identified in step 3.

5. Iteratively apply the differential corrections scheme to solve for the free variable vector that satisfies the constraints in equation (5.17). Continue until the l_2-norm of the constraint vector is less than or equal to a fixed tolerance. The converged free variable vector then represents the sinusoidal wave corresponding to the j-th frequency.

6. Using the components of the converged free variable vector, subtract the term $(A_j \cos(2\pi\omega_j t_n) + B_j \sin(2\pi\omega_j t_n))$ from $\tilde{z}^j(t_n)$.

7. Set $j = j + 1$.

8. Repeat steps 3-7 until the maximum scalar amplitude of $\tilde{z}^j(t_n)$ is less than some specified tolerance, or a pre-determined maximum number of frequencies are computed.

When these steps have been completed, the original function is decomposed into its dominant frequencies and is approximately reconstructed using equation (5.9).

5.4 Frequency Decomposition of Trajectories in the Circular Restricted Three-Body Problem

To produce the frequency representation for various types of trajectories, this frequency refinement technique is explored within the context of the CR3BP. First, a trajectory is selected from the desired region in a Poincaré map, a map that has been constructed using a $y = 0$ surface of section at a specified energy level. Once the map crossing that corresponds to a desired trajectory is identified, the initial state is propagated for approximately $9,000$ nondimensional time units and sampled

every 0.05 time units to generate a discrete set of data points. The discrete function, created from the x-coordinate in each sample, is multiplied by a Hanning window and initially decomposed into its frequency representation using an FFT algorithm. Each trajectory that is examined in this investigation lies in the exterior region; thus, a frequency analysis of the set of x-components corresponding to the state vectors along the path reveals any underlying frequencies. If any fundamental frequencies are identified from the DFT, the initial guesses for the corresponding sinusoidal waves are corrected using the targeting scheme summarized in Section 5.3.4.

Since a quasi-periodic orbit traces out a torus over time, it can be described by two independent and fundamental frequencies: a frequency ratio that is irrational signifies that a quasi-periodic orbit does not repeat over finite time spans. A quasi-periodic orbit is plotted in both configuration space and the frequency domain in Figure 5.6 over 100 time units. Although this orbit is actually propagated for a longer time span, only this range of the trajectory is plotted for visual clarity. The location of the two primaries are overlayed as red dots, and the arrow indicates the direction of orbital motion. In Figure 5.6(b), the DFT of this orbit appears scaled by the maximum amplitude of the computed Fourier coefficients. Multiple peaks are apparent in this frequency representation, each located at linear combinations of the two fundamental frequencies. Exploiting knowledge of the eigenvalues associated with the stable periodic orbit at the center of this quasi-periodic orbit, the largest peak approximately occurs at the frequency describing motion in the central direction, as defined in Section 3.2 and denoted ω_1. The two smaller peaks are located equidistant from this dominant peak; this distance, denoted ω_2, is approximately equal to the frequency governing motion in the transverse direction. Additionally, there are a number of significantly smaller peaks present in this DFT, approximately located at other linear combinations of the two fundamental frequencies.

As the contribution from the transverse mode approaches zero, the quasi-periodic orbits in a stable island reduce, in the limit, to the stable periodic orbit at their center. Although a periodic orbit possesses a single fundamental frequency, it can be

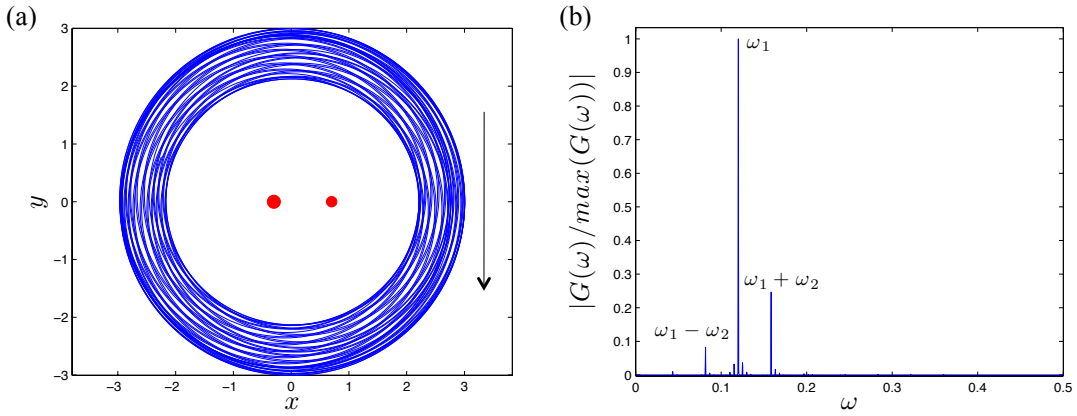

Figure 5.6. Representation of a quasi-periodic orbit in the (a) configuration space of the CR3BP and (b) frequency domain.

characterized by the features of its DFT. To demonstrate this concept, first consider the periodic orbit in Figure 5.7(a) as represented in the frequency domain; its DFT is plotted in Figure 5.7(b). The largest peak in this DFT is located at approximately the fundamental frequency, with smaller peaks occurring at multiples of this frequency. In contrast, a period-q orbit produces a DFT with different features. A sample period-3 orbit is plotted in Figure 5.8(a). The fundamental frequency corresponding to this orbit is known and equal the inverse of its period. The peak corresponding to this frequency, denoted ω_1, is identified on the DFT in Figure 5.8(b). Subsequently, the location of the largest peak in the DFT is identified as three times the fundamental frequency. Thus, for a period-q orbit, the ratio of the frequency locating the dominant peak in the DFT to the fundamental frequency is equal to the integer q. These observations are equally applicable to the frequency decompositions in the analysis of unstable periodic orbits.

In contrast to periodic and quasi-periodic orbits, a chaotic trajectory cannot be decomposed into a finite set of frequencies. Accordingly, a chaotic trajectory appears as a large set of randomly-distributed frequencies in the frequency domain. This is demonstrated using the chaotic trajectory plotted in Figure 5.9(a); the corresponding DFT is plotted in Figure 5.9(b). As expected, the DFT features a large number of

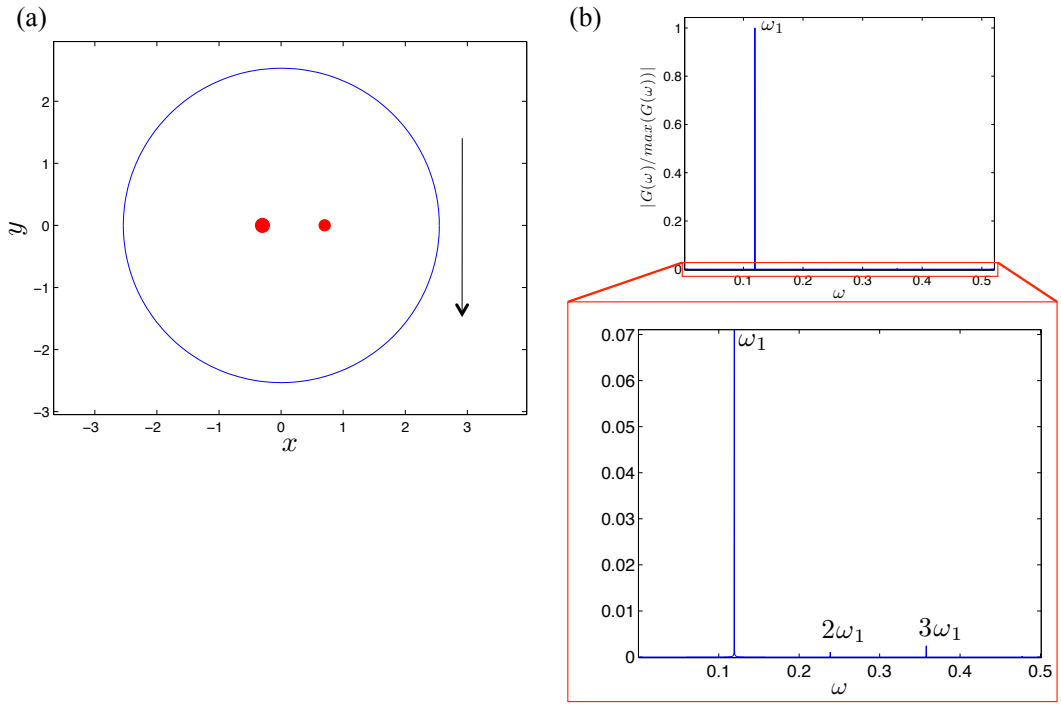

Figure 5.7. Representation of a nonresonant periodic orbit in the (a) configuration space of the CR3BP and (b) frequency domain.

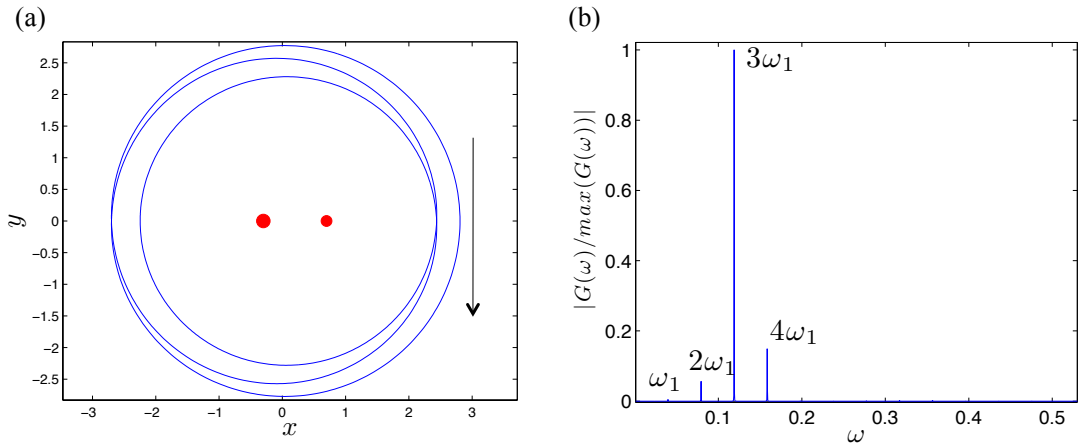

Figure 5.8. Representation of a resonant periodic orbit in the (a) configuration space of the CR3BP and (b) frequency domain.

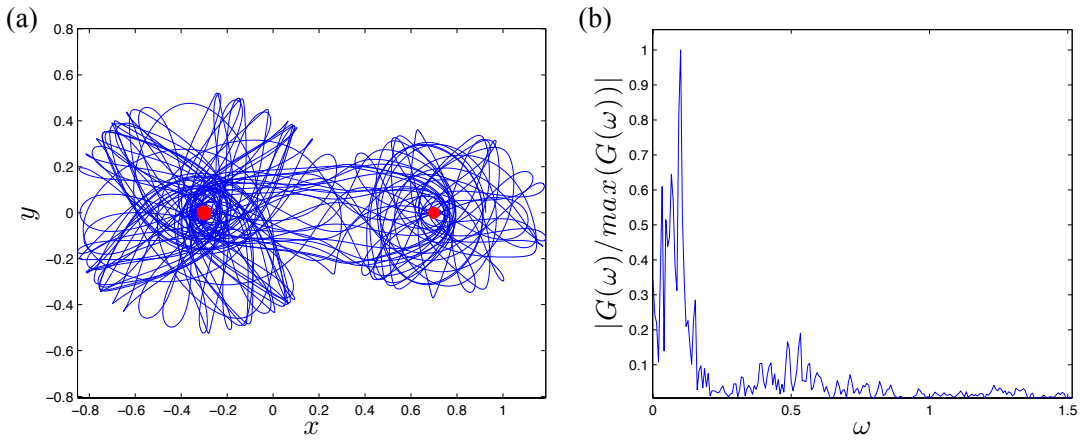

Figure 5.9. Representation of a chaotic trajectory in the (a) configuration space of the CR3BP and (b) frequency domain.

peaks of significant magnitude, but located at random frequencies. If the chaotic trajectory shadows a nearby quasi-periodic orbit prior to departing chaotically, frequencies close to those of the quasi-periodic orbit may emerge in the DFT.

5.5 Frequencies Characterizing Trajectories in the Exterior Region in the Circular Restricted Three-Body Problem

The process of decomposing a single trajectory into its fundamental frequencies is then extended to the representation of the dynamical structures in the CR3BP in the frequency domain. Frequency decomposition is applied to the analysis of retrograde trajectories in the vicinity of the stable period-1 orbit located in the exterior region in the CR3BP. At discrete values of the energy constant, nearby quasi-periodic orbits are sampled and decomposed into their fundamental frequencies. For each value of the energy constant, the frequency ratio the corresponds to ordered motion intersecting $y = \dot{x} = 0$, forms a one parameter curve. The continuity along subsections of this curve depends on whether the quasi-periodic orbits of interest are embedded within a stable island, or appear as concentric islands separated by unbounded chaos. The one parameter frequency ratio curves, each computed at various energy levels, are overlaid

to represent the spectrum of the dynamical behavior present within the region of interest. This resulting composite frequency representation is used to analyze the existence and properties of orbits in this region in the CR3BP.

Construction of a composite frequency representation begins with a frequency analysis at a single energy level. Consider an energy constant that is equal to the value $C = 3.880149584125780$. The corresponding $y = 0$ Poincaré map, localized to the exterior region, is plotted in Figure 5.10. The structures captured by this map are located to the left of the two primaries and far beyond the location of L_3. By observation, the periodic and quasi-periodic orbits form concentric curves and island chains that cross the $\dot{x} = 0$ line, overlaid in blue in the figure. The structures contained within this region are, therefore, sufficiently represented by considering only trajectories corresponding to map crossings coinciding with the $\dot{x} = 0$ line. This subset of map crossings forms the set of initial conditions for trajectories that are integrated and decomposed into their fundamental frequencies. At the specified energy level, each of the resulting nonchaotic orbits is identified by the coordinate pair $(x_0, \omega_2/\omega_1)$. Here, x_0 represents the nonunique x-coordinate of the map crossing coinciding with the $\dot{x} = 0$ line, and ω_2/ω_1 is the frequency ratio of the corresponding orbit, computed using the frequency refinement technique.

At a given energy level, the one parameter curve formed by the frequency ratios of quasi-periodic orbits reveals the structures visible in a Poincaré map. The frequency ratios, computed for orbits in the vicinity of the stable period-1 orbit at $C = 3.880149584125780$, are plotted in blue in Figure 5.11. This plot also features red dashed lines at selected, labeled integer ratios. Consider the two intersections of the frequency ratio curve with the $\omega_2/\omega_1 = 1/5$ line: both occur at the same x-coordinate as the intersections of the period-5 island chain with the $\dot{x} = 0$ line on the map depicted in Figure 5.10. The left-most intersection of the period-5 island chain with the $\dot{x} = 0$ line occurs at an unstable periodic orbit; on the right, a stable period-5 orbit intersects $\dot{x} = 0$ line. Correspondingly, these two intersections appear distinctly different in the frequency representation: the unstable orbit appears as a

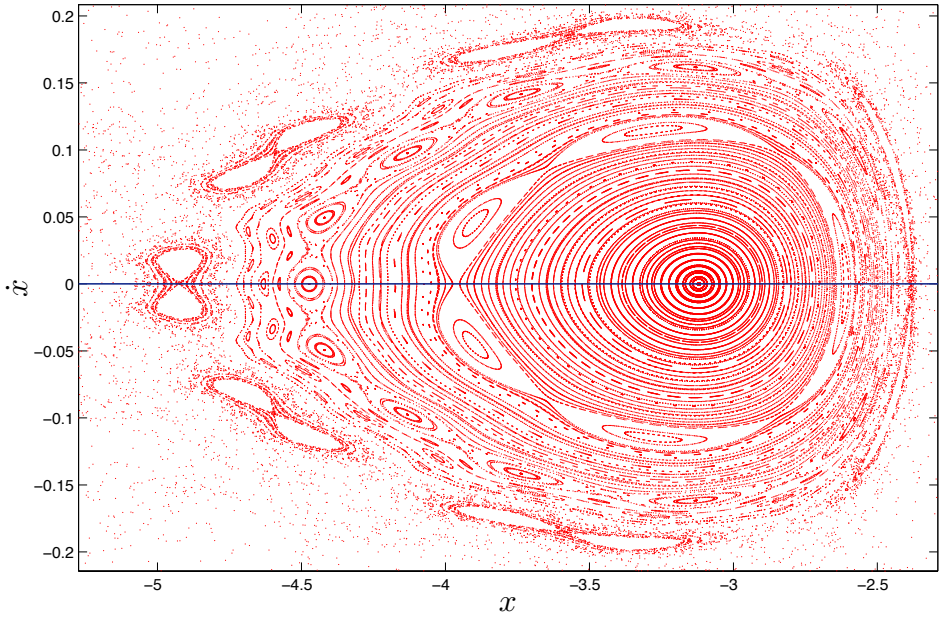

Figure 5.10. Poincaré map at $C = 3.880149584125780$, constructed using a $y = 0$ section, localized to the exterior region in the CR3BP.

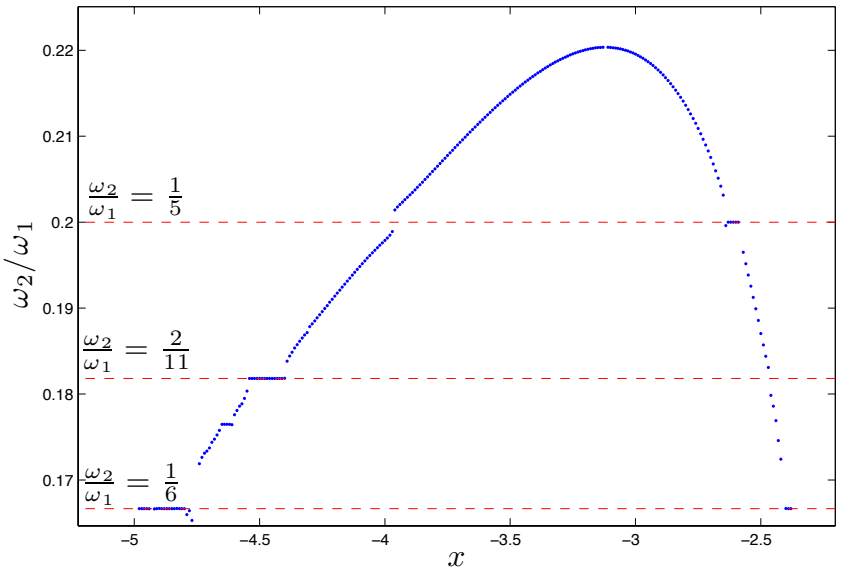

Figure 5.11. Frequency representation of retrograde periodic and quasi-periodic orbits in the vicinity of the stable period-1 orbit in the exterior region for $C = 3.880149584125780$.

steep, yet discontinuous change in the frequency ratio, while the frequency ratio at the location of the stable orbit lies at the center of a discontinuous plateau formed by the frequency ratios of its surrounding quasi-periodic orbits. These frequency ratio curves are only discontinuous at the location of a periodic orbit, where two fundamental frequencies do not exist; the periodic orbit can be stable or unstable. Extending these observations, any stable or unstable period-q orbit is identified and located on the frequency ratio curve when the previously described features are centered about the integer ratio, p/q for $q > 1$ and $p < q$. As demonstrated in this example, the denominator equals the q map crossings of a retrograde period-q orbit in the exterior region. If q is an even number, the two intersections of the frequency ratio curve with $\omega_2/\omega_1 = p/q$ correspond to two crossings of a single stable or unstable orbit in the period-q island chain. A value of q that is odd, however, reveals both the stable and unstable period-q orbits contained within the island chain. In addition, the sum $p + q$ is approximately equal to the ratio of the orbital period to the period of the primaries; this property is apparent using any differentially corrected period-q orbit.

Frequency representation of the structures present over a range of energy levels introduces a third parameter identifying each orbit: its energy level. A single orbit is, therefore, described by the tuple $(x_0, \omega_2/\omega_1, C)$. Accordingly, periodic and quasi-periodic orbits that exist within a specified range of energy levels form a two parameter surface when represented using frequency ratios. This surface can be approximated by overlaying each of the frequency ratio curves, computed at various discretely sampled energy levels. To reduce the complexity in visualizing the resulting surface approximation, simple two-dimensional representations of this three-dimensional information are constructed. Due to the inherent loss of information, the specific configuration must be tailored to the immediate goal.

If the form and stability of ordered motion are the focus of the analysis, the frequency ratio can be plotted for each value of x_0 that identifies an orbit at any energy level. An example of this concept is depicted in Figure 5.12 for retrograde periodic and quasi-periodic orbits in the exterior region in the CR3BP and for energy levels between

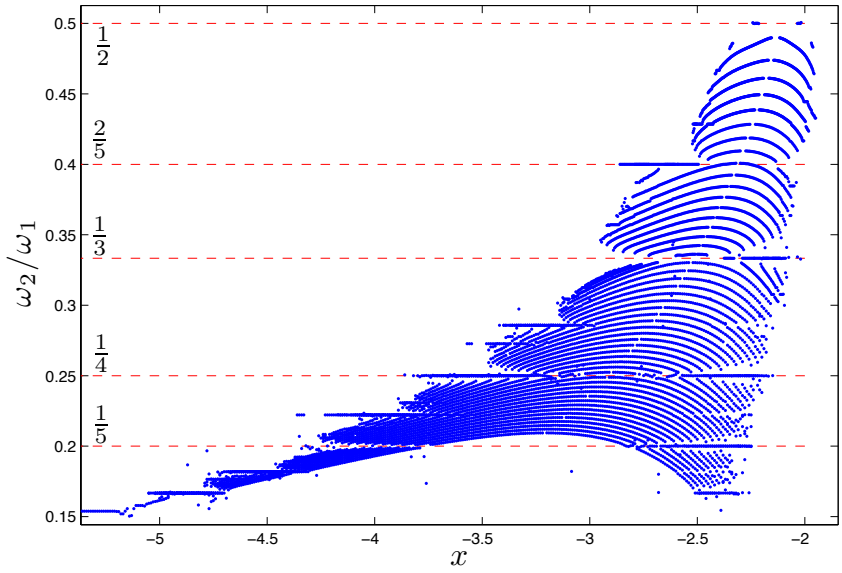

Figure 5.12. Composite representation of the frequency ratios of retrograde periodic and quasi-periodic orbits in the exterior region in the CR3BP for energy levels between $C(L_1)$ and $C(L_3)$.

$C(L_1)$ and $C(L_3)$. Overlaid on this plot are red dashed lines indicating the integer ratios corresponding to selected low-order period-q orbits. Although the energy level is a quantity that is not represented in this plot, each frequency ratio curve 'connects' periodic and quasi-periodic orbits at the same energy level. Analysis of this figure reveals that the frequency ratio passes through integer ratios, m/q, reflecting various period-q orbits, signaling the existence of the corresponding orbits within the specified energy range. In addition, the stability of these orbits can also be determined. Recall that unstable orbits are identified from steep changes in the frequency ratio, while stable orbits are located within a frequency ratio plateau. These observations are extended to aid in the interpretation of the composite frequency representation in Figure 5.12. Consider the curves intersecting the integer ratio $\omega_2/\omega_1 = 1/3$. The lack of data points on the left half of this intersection reveals the location of the unstable orbit within a period-3 chain, while the horizontal accumulation of points on the right side indicates the stable period-3 orbit and its surrounding quasi-periodic motion.

To determine the boundaries of a structure within the phase space and the energy levels at which it exists, a two-dimensional representation is constructed using selected level sets of the frequency ratio. Given a period-q orbit that possesses the frequency ratio p/q, its corresponding level set in the frequency ratio is approximated by processing the discretely sampled tuples $(x_0, \omega_2/\omega_1, C)$. If the period-$q$ orbit is stable, its associated quasi-periodic orbits are represented by plotting the (x_0, C) coordinates of orbits with frequency ratios in the range $(p/q-\epsilon) < \omega_2/\omega_1 < (p/q+\epsilon)$, for a reasonably small, positively-valued ϵ. An example of this representation is plotted in Figure 5.13 for selected retrograde period-q orbits located in the exterior region in the CR3BP; these orbits possess a frequency ratio that is sufficiently close to the integer ratio $1/q$, for $q > 1$, and are labeled as "P-q". On the vertical axis, the energy constant computed for each orbit is scaled by the difference $C(L_2) - C(L_3)$. The energy levels corresponding to L_2 and L_3 are used as a reference because these two Lagrange points bound motion between the interior and exterior regions. To represent the unstable periodic orbits present in a period-q chain, the energy and appropriate x-crossing of the unstable orbit are obtained using continuation. This composite frequency representation in Figure 5.13 depicts the extent of the periodic orbits in a period-q island chain within the phase space, for various values of the energy. In addition, the regions about each curve, representing a family of periodic orbits, are populated by quasi-periodic orbits; the spread of points from the curve represents the extent of quasi-periodic motion that persists within the phase space.

Together, the two composite frequency representations in Figures 5.12 and 5.13 offer information about ordered motion in the exterior region in the CR3BP at energy constants between $C(L_1)$ and $C(L_3)$. As plotted in Figure 5.12, each frequency ratio curve, computed for quasi-periodic orbits at a single energy level, features an undefined maximum frequency ratio corresponding to the period-1 orbit at the center of the stable island. The frequency ratio is undefined at this location because periodic orbits are only described by one frequency. A quasi-periodic orbit that exists further from the central period-1 orbit exhibits a lower frequency ratio. Furthermore,

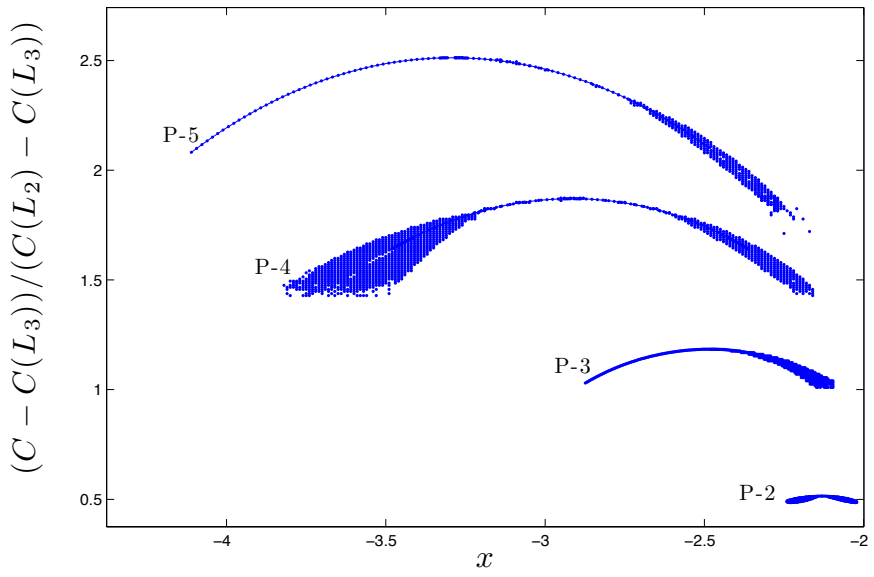

Figure 5.13. Composite representation of the energy levels of selected retrograde period-q orbits and their surrounding quasi-periodic orbits. These orbits are located in the exterior region in the CR3BP.

decreasing the energy constant results in each curve encompassing higher frequency ratios. Since a period-2 orbit, for example, possesses a frequency ratio equal to 1/2, it is, therefore, accessible at a lower value of the energy constant than a period-5 orbit with the frequency ratio 1/5. In fact, over the range of energy constants that are examined, a variety of low-order period-q orbits exist. Recall Figure 5.13, which features a selection of these orbits with the frequency ratio $1/q$; each orbit family is formed at an energy constant equal to the highest energy constant of the period-q family in this frequency representation. The stable orbits in the resulting island chain are surrounded by quasi-periodic orbits, which extend further into the phase space with decreasing energy constant, until a critical value of the energy constant is reached. Then, the stable islands rapidly decrease in size as the period-q orbits approach a fold bifurcation. For period-q orbits with an even number of maps crossings, it is clear in Figure 5.13 that the size of the two stable islands captured during this process is not consistent: the stable island closest to the two primaries encompasses a

smaller range in the x-coordinate, or, equivalently, a larger range of velocities in the y-direction, than the leftmost island. Combining the two composite frequency representations, therefore, allows for the description and characterization of the range of dynamics present in the exterior region in the CR3BP. Similar analyses may also be performed in the MCR3BP for various values of the three-body potential coefficient, k, elucidating the effects of the additional interaction on the solution space.

6. CHARACTERISTICS OF THE THREE-BODY INTERACTION

By combining techniques developed in dynamical systems theory and frequency analysis, a subset of the underlying dynamical structures in the MCR3BP are examined over a range of values of the three-body potential coefficient, limited to $k = [-0.2, 0.8]$. The existence and location of five potential equilibrium points are determined for values of k within the aforementioned range. Using the energy constant evaluated at these equilibrium points, the zero velocity curves are also constructed. A frequency analysis is completed on retrograde periodic and quasi-periodic solutions that exist in the exterior region of the MCR3BP. To explore the influence of the three-body potential term, these results are compared to the frequency analysis of ordered motion in the CR3BP. Additionally, a stability analysis on selected families of period-q orbits yields changes in stability due to the presence of the additional three-body interaction in the MCR3BP.

6.1 Equilibrium Points

The existence and location of equilibrium points offer preliminary insight into the impact of a three-body interaction, for various values of the coefficient k, on the dynamical environment in the MCR3BP. Using the process from Section 2.6 for solving the equations of motion when the accelerations and velocities are set equal to zero, the equilibrium points of the MCR3BP are located for various values of k. The five equilibrium points that exist in the range $k = [-0.2, 0.8]$ are plotted in Figure 6.1. In this figure, the green dots indicate the location of the five equilibrium points in the CR3BP for a mass ratio $\mu = 0.3$. The equilibrium points for positive values of k in the specified interval appear as blue dots in the figure, while red dots locate

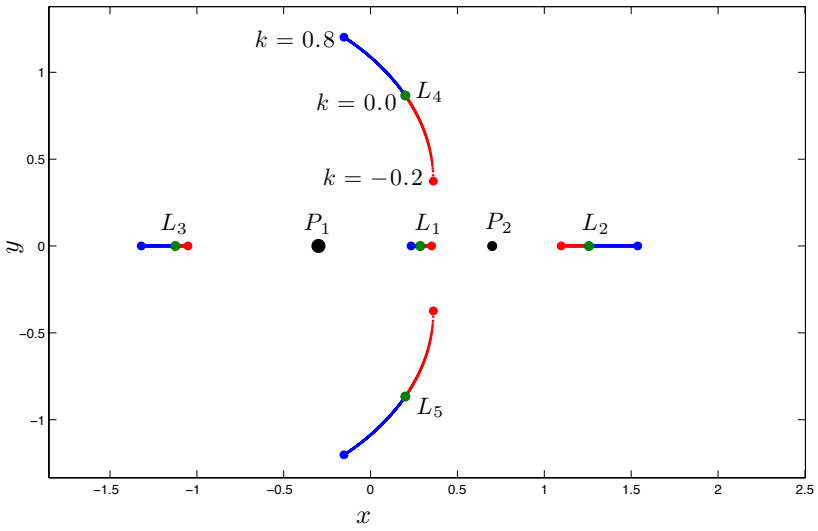

Figure 6.1. Location of equilibrium points for values of the three-body potential coefficient in the range $k = [-0.2, 0.8]$.

the equilibrium points corresponding to negative values of k. Since the MCR3BP is formulated to reduce to the CR3BP as the coefficient k approaches zero, equilibrium points computed for increasing magnitudes of the three-body potential coefficient exist further from the equilibrium points in the CR3BP. As an example, the location of L_4 is labeled in Figure 6.1 for $k = -0.2, 0.0, 0.8$. Analysis of this figure reveals that, for increasingly positive values of the three-body potential coefficient, the collinear equilibrium points are located further from P_2. The location of L_1 varies less for positive values of k than the locations of L_2 and L_3 since L_1 exists between the two primaries, where the inverse-square gravitational forces act in opposing directions. Furthermore, in the MCR3BP, the triangular equilibrium points, L_4 and L_5, are no longer located at the vertices of an equilateral triangle; instead, they exist further from the primaries. For negative values of k, the equilibrium points are all located closer to P_2 than the equilibrium points in the CR3BP. In addition, the locations of the triangular equilibrium points appear most sensitive to negative values of k, when the three-body interaction opposes the gravitational forces.

Another effect of the three-body interaction emerges when the energy constant is evaluated at each equilibrium point for various values of the constant, k, that scales the additional term. These energy constants, $C(L_i)$, are plotted in Figure 6.2 and colored as indicated in the legend. Note that, due to symmetry, the value of the energy constant at the triangular equilibrium points are the same, that is, $C(L_4)$ is equivalent to $C(L_5)$. For increasingly positive values of k within the specified range, the energy constant evaluated at each equilibrium point increases. Notably, $C(L_1)$ increases rapidly with increasing k, presenting a challenge in using the energy constant to compare the dynamical structures under the influence of various scaling factors for the three-body interaction. For increasingly negative values of k, however, the values of the energy constants $C(L_i)$ in the MCR3BP do not maintain an order, by magnitude, that is consistent with the order of the $C(L_i)$ values in the CR3BP. Physically, this change in the order of the values of the energy constants $C(L_i)$ translates to the L_i gateways opening in a different order for a decreasing energy constant, or, equivalently, increasing energy. For example, consider the MCR3BP when $k = -0.1$: comparison of the energy constant at the three collinear equilibrium points reveals that the L_2 gateway will open at the lowest energy, or highest energy constant. Although P_3 can travel between the exterior and P_2 regions, it cannot cross into the P_1 region. Within the context of the CR3BP, this scenario is not possible, indicating that a three-body interaction opposing the two inverse-square gravitational forces can modify the regions that a single, natural trajectory may traverse.

6.2 Zero Velocity Curves

The regions of allowable motion in the MCR3BP, for various values of k, are straightforwardly visualized using zero-velocity curves, as developed in Section 2.7. For a specified value of the three-body coefficient, the shape and location of the ZVCs depend upon the energy constant; however, insight into the possible motion in the planar MCR3BP is obtained by analyzing the ZVCs at the values of the energy

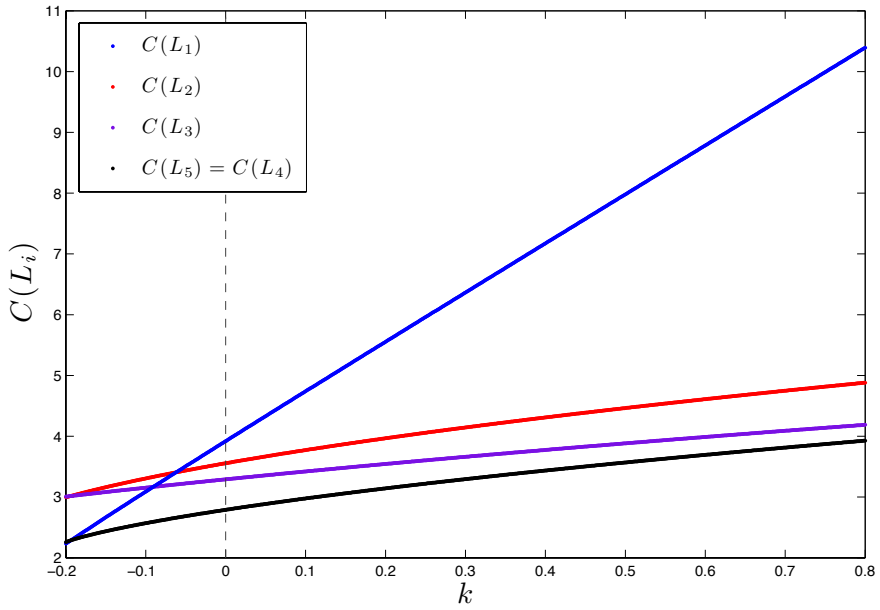

Figure 6.2. Energy constant evaluated at the equilibrium points for the range $k = [-0.2, 0.8]$.

constant corresponding to the three collinear equilibrium points. The ZVCs at these three distinct energy levels are plotted in Figure 6.3 for the following values of the three-body coefficient: (a) $k = 0.0$, (b) $k = -0.1$, and (c) $k = 0.4$. To aid in visual clarity, the ZVCs at $C(L_1)$, $C(L_2)$, and $C(L_3)$ are colored blue, red, and purple, respectively. Additionally, the equilibrium points are represented as black diamonds and the primaries are indicated by black filled circles.

The ZVCs plotted for $k = -0.1$ reveal that for an energy constant equal to $C(L_1)$, P_3 can travel through the L_2 and L_3 gateways, allowing motion between the vicinity of a primary and the exterior region. However, a natural trajectory cannot move directly between P_1 and P_2 without traversing the exterior region; such a dynamical constraint is not known to exist in the planar CR3BP. As described in Section 6.1, this shape for the ZVC boundaries corresponds to the energy constant evaluated at L_1 having a lower value than the energy constants $C(L_2)$ and $C(L_3)$. For the ZVCs plotted at these two larger values of the energy constant, the forbidden regions encompass less of the exterior region than the ZVCs at a comparable energy level in the CR3BP.

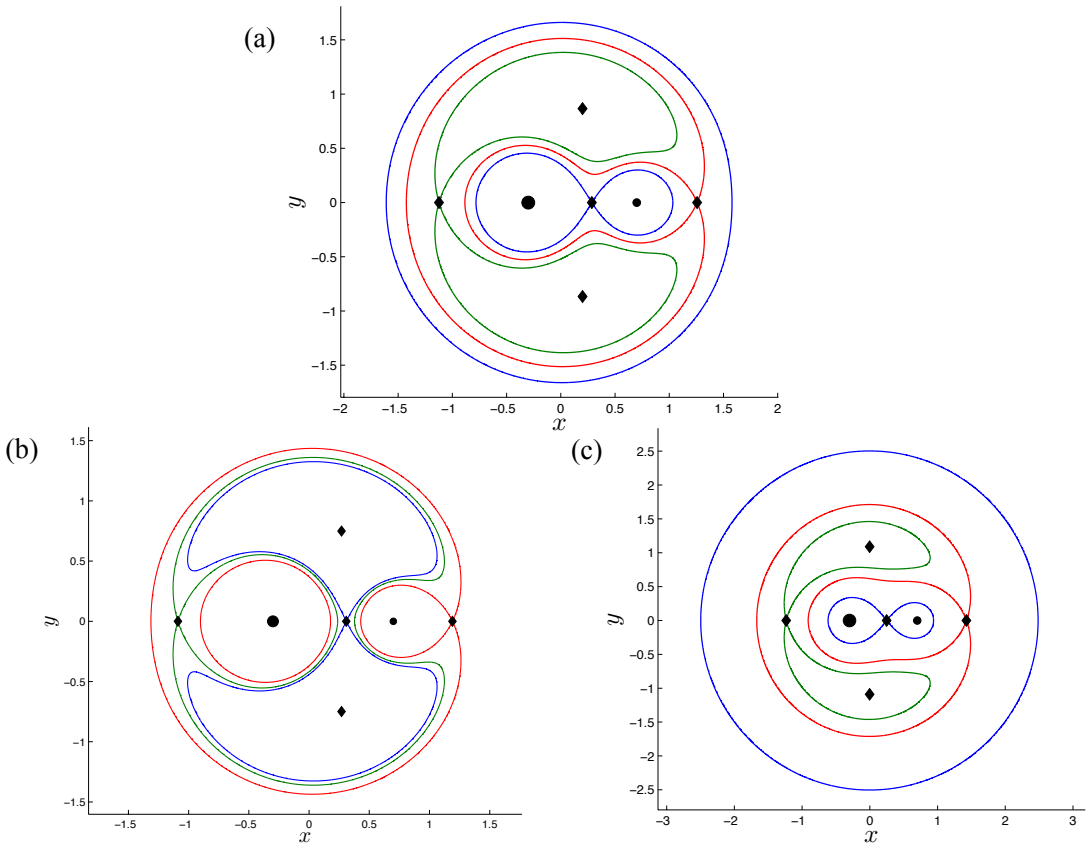

Figure 6.3. Zero velocity curves at the values of $C(L_1)$ (blue), $C(L_2)$ (red), and $C(L_3)$ (purple) corresponding to the three collinear equilibrium points for (a) $k = 0$, (b) $k = -0.1$, and (c) $k = 0.4$ in the MCR3BP.

For a positive three-body potential coefficient, $k = 0.4$, the ZVCs loosely resemble those in the CR3BP, with some small differences. One example is that the ZVCs at $C(L_1)$, evaluated in the MCR3BP, extend further into the interior and exterior regions. However, decreasing the energy constant reveals that more of the interior region is accessible to P_3 at higher energies. Consequently, at an energy constant equal to $C(L_2)$, the increased size of the L_1 gateway results in a larger range of trajectories transferring between the vicinities of both primaries than in the CR3BP.

This increase in the size of the L_1 gateway may impact the properties and the types of periodic solutions that are available within the interior region in the MCR3BP.

6.3 Periodic and Quasi-Periodic Structures in the Exterior Region

The composite frequency representations developed in Section 5.5 are employed to compare periodic and quasi-periodic orbits in the MCR3BP. Given that a three-body interaction may be attractive or repulsive, the MCR3BP is analyzed for selected positive and negative values of the three-body potential coefficient. In particular, this investigation focuses on three properties of the dynamical characteristics that are observed in the exterior region: the form of stable structures, the energy levels at which these structures are available, and their extent within the phase space.

For positive three-body potential coefficients below a critical value, period-q orbits that are present in the CR3BP also exist in the MCR3BP. In Figure 6.4, the

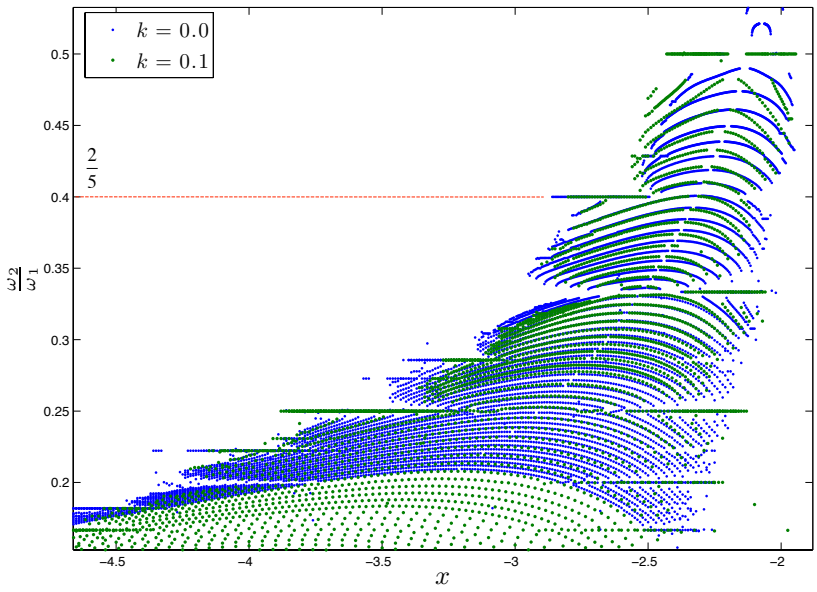

Figure 6.4. Composite representation of the frequency ratios of retrograde orbits over various energy levels in the range $C = [C(L_3, C(L_1)]$, for $k = 0.0$ (blue) and $k = 0.1$ (green).

frequency ratios corresponding to orbits within the central stable island are plotted for various energy levels in the range $C = [C(L_3), C(L_1)]$ in the CR3BP (blue) and in the MCR3BP for $k = 0.1$ (green). Analyzing this figure, the frequency ratios of the orbits that exist when $k = 0.1$ encompass a larger range of integer ratios than in the CR3BP. Thus, periodic orbits existing within this specific range of energy constants in the CR3BP are also present over a comparable range of energy levels in the MCR3BP for $k = 0.1$. The low-order period-q orbits in both models appear similarly in the frequency domain. Consider the intersections of the frequency ratio curves with the integer ratio 2/5, indicated by the red dotted line. These intersections appear as a horizontal plateau on the left of the central period-1 orbit and a steep change occurs on the right. Since these features are consistent between the MCR3BP for $k = 0.1$ and the CR3BP, the frequency analysis process reveals a similar configuration for the stable and unstable orbits within the period-5 island chain. Extending this observation to other integer ratios, various families of period-q orbits in the MCR3BP, over the range of positive coefficients examined in this investigation, appear qualitatively similar to the CR3BP when represented in the frequency domain.

The phase space representations of stable, low-order period-q orbits do not exhibit any structural differences between the CR3BP and the MCR3BP, for positive values of the three-body coefficient. Selected period-3 and period-6 orbits, for $k = 0.1$, are plotted in Figures 6.5 and 6.6, respectively, in the (a) rotating frame and (b) inertial frame for five periods. In the inertial views, the orbits of P_1 and P_2 are plotted in blue and red, respectively, while the primaries are located using blue circles in the rotating frame. These orbits, which are periodic in the rotating frame, are not periodic in the inertial frame because the periods are not equal to an exact integer multiple of the period of the primaries. In fact, the orbits appear to precess in the inertial frame, remaining bounded with respect to the two primaries.

Assume positive values of the three-body coefficient for the model in the MCR3BP: under these conditions, quasi-periodic orbits exist at lower energy constants than in the CR3BP and extend further into the phase space. This information is extracted

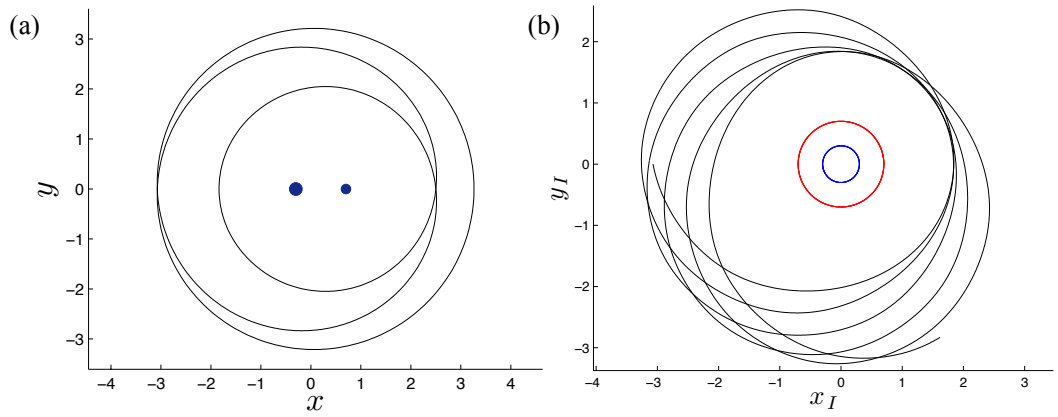

Figure 6.5. Period-3 orbit in the MCR3BP for $k = 0.1$ represented in the (a) rotating frame and (b) inertial frame.

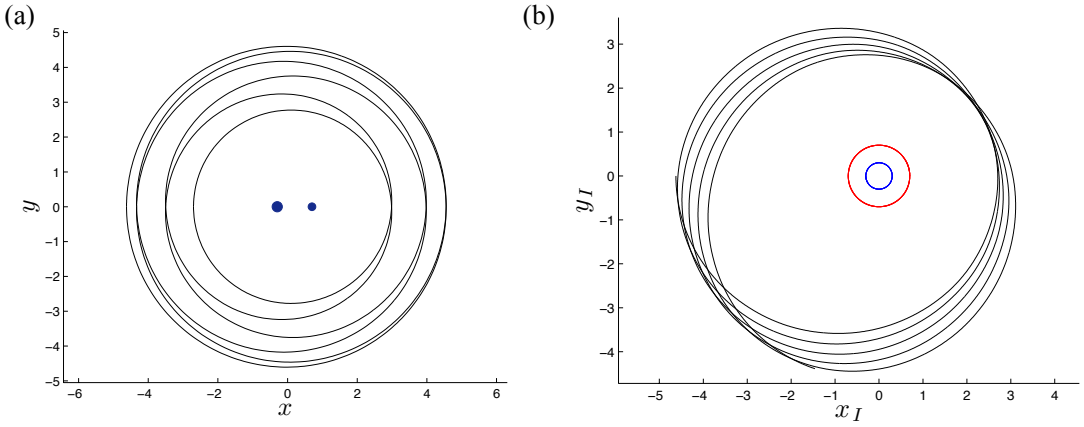

Figure 6.6. Period-6 orbit in the MCR3BP for $k = 0.1$ represented in the (a) rotating frame and (b) inertial frame.

by considering the energy levels and locations of a selected set of period-q orbits with frequency ratios $1/q$, as plotted in Figure 6.7 for $k = 0.1$ (green) and $k = 0$ (blue). Analysis of this figure reveals that, incorporating an attractive three-body interaction, each of the selected, stable period-q structures is accessible over a smaller range of energy values that are lower in magnitude relative to the difference $C(L_2) - C(L_3)$. Additionally, for increasingly positive values of the three-body coefficient, up to a critical value, the stable islands extend further within the phase space, that is, over a greater interval in x. Consider the frequency domain representation of the period-

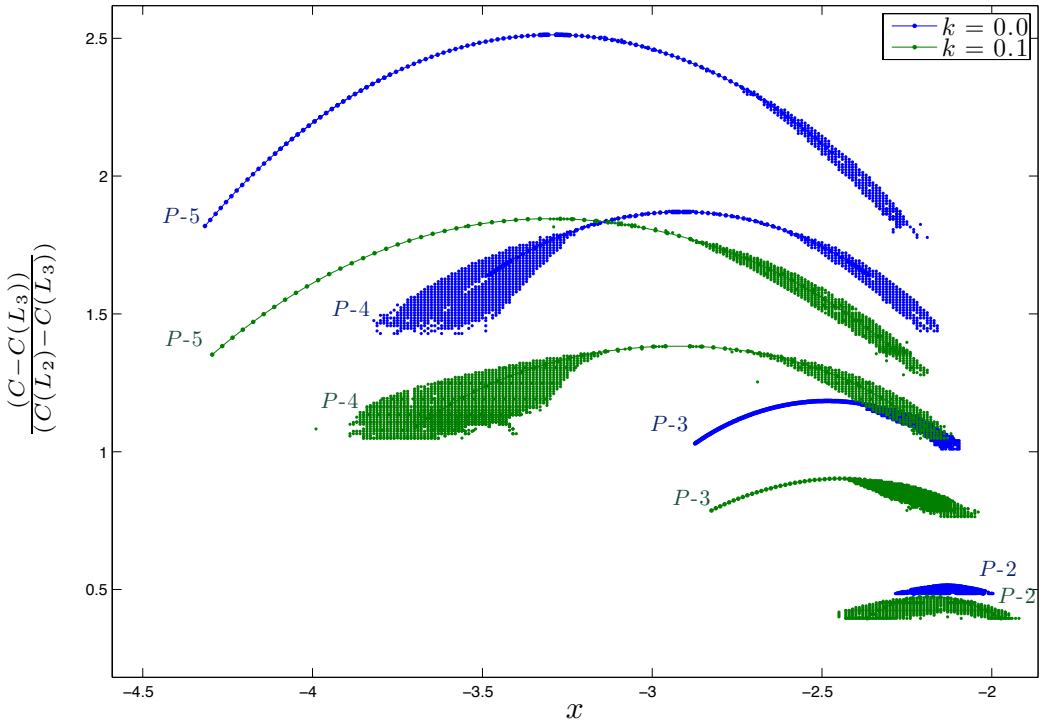

Figure 6.7. Composite representation of the energy levels of selected retrograde period-q orbits (with frequency ratio $1/q$) and their surrounding quasi-periodic orbits, for $k = 0.0$ (blue) and $k = 0.1$ (green).

4 stable island in the MCR3BP with the coefficient $k = 0.1$, as plotted in Figure 6.7; the map crossings for the surrounding quasi-periodic motion are clearly wider in the x-direction than in the CR3BP. The bounds on the quasi-periodic motion about resonant orbits, therefore, exist further from the corresponding period-q orbit. These larger islands can appear either within a sea of chaos or embedded between quasi-periodic orbits about the central period-1 stable orbit.

Beyond a critical positive value of the three-body potential coefficient, period-multiplying bifurcations influence the underlying periodic orbits in the MCR3BP and, therefore, the surrounding quasi-periodic motion. In Figure 6.8, the level sets corresponding to selected period-q orbits for $k = 0.6$ are overlaid on the level sets depicted in Figure 6.7. For this larger value of the three-body potential coefficient, the quasi-periodic orbits exhibit behavior that is not consistent with the CR3BP.

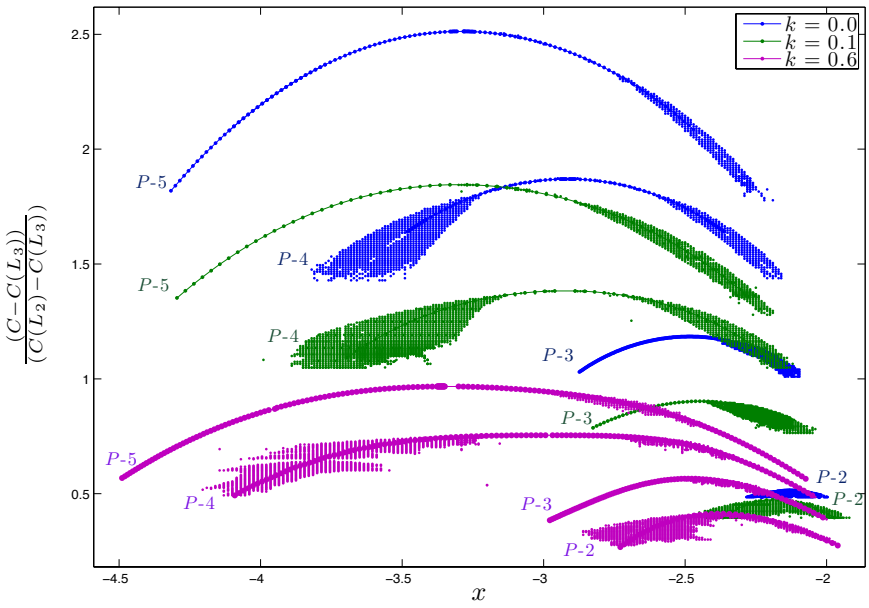

Figure 6.8. Composite representation of the energy levels of selected retrograde period-q orbits (with frequency ratio $1/q$) and their surrounding quasi-periodic orbits, for $k = 0.0$ (blue), $k = 0.1$ (green) and $k = 0.6$ (magenta).

Consider, for example, the leftmost island surrounding a stable period-4 orbit in Figure 6.8: a zoomed-in view appears in Figure 6.9. The location of the outermost quasi-periodic orbit in the stable island clearly fluctuates over the range of energy levels where a stable period-4 orbit exists. An explanation for this behavior emerges from a stability analysis of the underlying family of periodic orbits. The stability index, s, for this family of planar orbits is plotted in Figure 6.10 as a function of the energy value. Overlaid on the stability index curve are several dotted lines. The two red lines are located at the critical stability indices $s = -2$ and $s = +2$, the former also corresponds to a period-doubling bifurcation. Additionally, the black lines represent selected, labeled period-multiplying bifurcations. Analyzing this figure, the family of period-4 orbits undergoes successive period-multiplying bifurcations for multiplicative factors greater than 2. Since the stability index does not graze or pass through the value $s = -2$, a period-doubling bifurcation does not occur along this

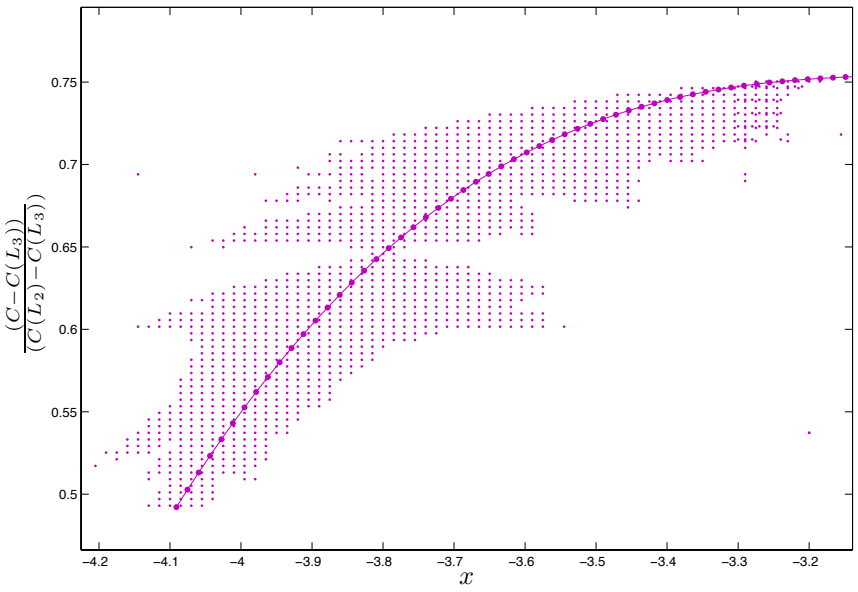

Figure 6.9. Zoomed-in view of Figure 6.8, focused on the leftmost crossings of the period-4 stable island for $k = 0.6$.

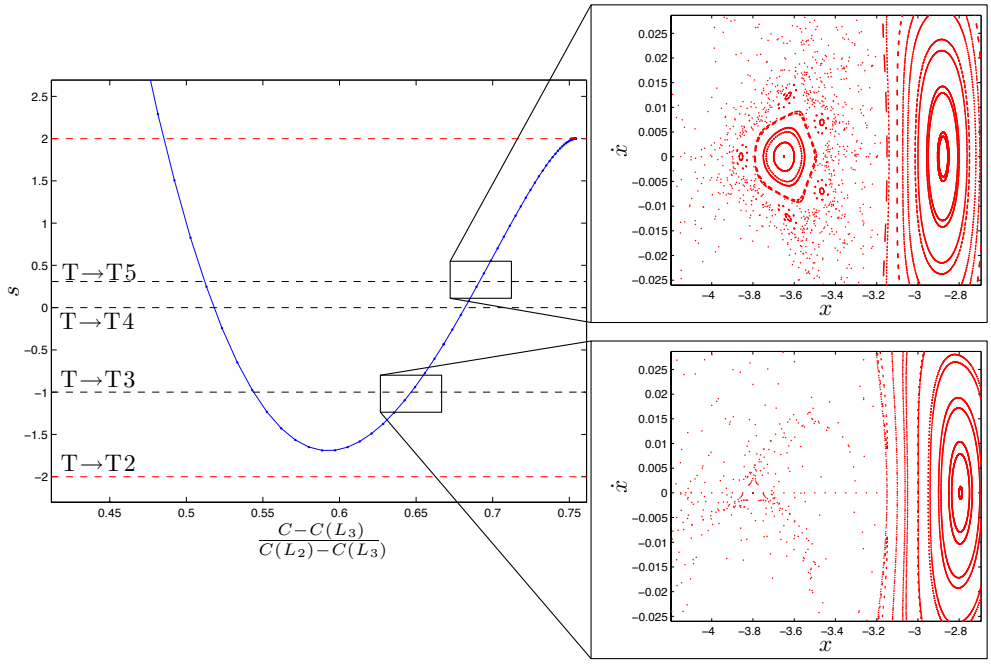

Figure 6.10. Stability index for stable period-4 orbits in the MCR3BP for $k = 0.6$, with dotted lines at the stability indices corresponding to selected bifurcations. In the insets, zoomed-in views of the Poincaré map near highlighted period-multiplying bifurcations.

family. The top and bottom insets of Figure 6.10 depict Poincaré maps constructed at energy levels below those corresponding to period-multiplying bifurcations for the multiplicative factors 5 and 3, respectively. Each map is zoomed-in to the vicinity of one of the period-4 stable islands. Considering the top inset, a period-4 orbit family has created a family of period-20 orbits at a nearby energy level. Given that this new family of orbits also has a frequency ratio equal to 1/4, the period-multiplying bifurcation is not detectable on the frequency representations. Instead, the presence of these bifurcations is reflected in the shape of the level sets in Figure 6.8. Since this dynamical behavior is not observed in this region in the CR3BP for a mass ratio of $\mu = 0.3$, significantly large positive values of the three-body potential coefficient apparently induce period-multiplying bifurcations along families of period-q orbits.

The critical positive value of k at which certain period-multiplying bifurcations occur depends upon the family of period-q orbits. This observation is straightforwardly supported by an analysis of the stability index of various orbit families at a single value of the three-body coefficient. As an example, consider the stability index over some interval of the period-2 to period-5 orbit families plotted in Figure 6.11 for $k = 0.6$. The frequency ratio along these families is equal to $\omega_2/\omega_1 = 1/q$. In contrast to the CR3BP, the stability indices of the plotted intervals of the period-q families pass through a wide range of values of s, with the minimum values along these curves varying between each family. The period-5 family passes through $s = -2$, undergoing a period-doubling bifurcation at two values of the energy constant. Between these bifurcations, the members of the family are unstable. The minimum along the curve reflecting the stability index for part of the period-3 family, however, does not pass through $s = -2$ or $s = -1$. This observation suggests that for a three-body potential coefficient of $k = 0.6$, the period-3 family does not undergo period-tripling or period-doubling bifurcations. Extending this analysis to periodic orbits in the MCR3BP for different values of k reveals that these bifurcations do occur in the period-3 family for larger values of the three-body coefficient. Thus, the value of the positive coefficient k

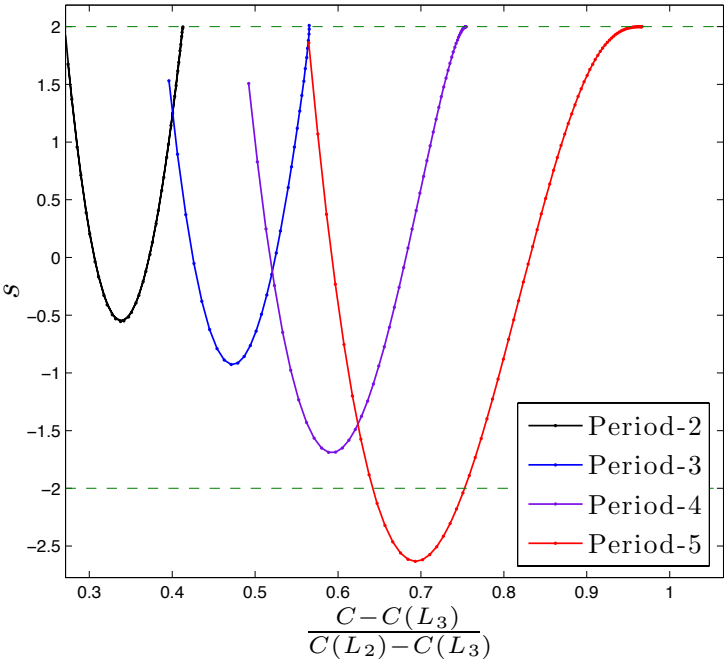

Figure 6.11. Stability index curves for period-2 to period-5 orbits in the MCR3BP for $k = 0.1$.

for which period-multiplying bifurcations are present along families of period-q orbits, where $q > 1$, depends upon the family.

Negative three-body potential coefficients, smaller in magnitude than a critical value, influence the dynamics in the MCR3BP by reducing the size of the regions of stable motion and the energy levels at which they exist. The composite frequency representation in Figure 6.12 depicts the level sets of selected period-q orbits and their associated quasi-periodic motion for $k = 0.0$ (blue), $k = -0.01$ (black) and $k = -0.1$ (grey). The stable period-q orbits, for negative values of k, are available at higher energy constants, and over a smaller range. In addition, the regions of stable motion surrounding the selected families of periodic orbits contract in the x-direction for $k = -0.01$. This observation is clear from the level sets in Figure 6.12, which do not deviate as far from the period-q orbits as those in the CR3BP.

For a negative value of the three-body potential coefficient greater in magnitude than a critical value, the dynamical structure in the exterior region do not resemble

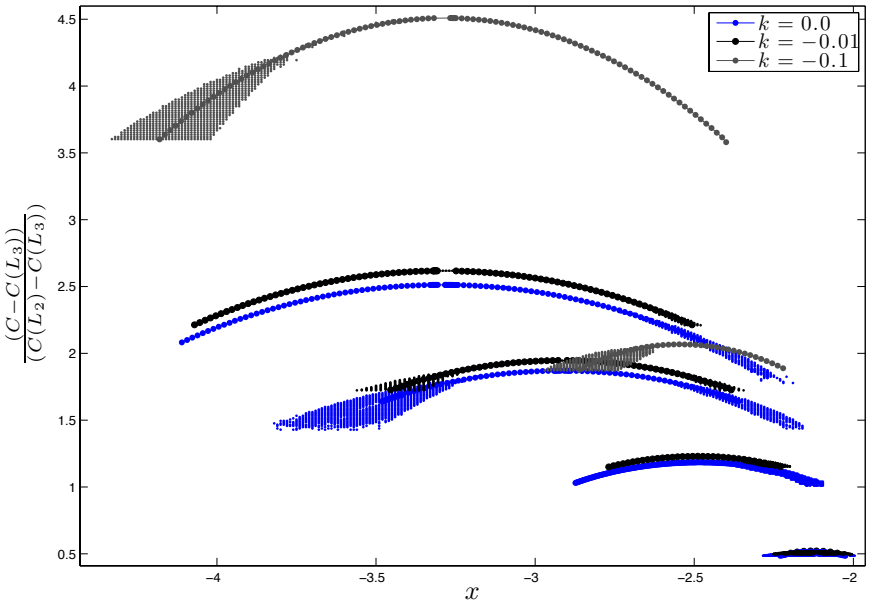

Figure 6.12. Composite representation of the energy levels of selected retrograde period-q orbits (with frequency ratio $1/q$) and their surrounding quasi-periodic orbits, for $k = 0.0$ (blue), $k = -0.01$ (black) and $k = -0.1$ (grey).

those in the CR3BP. The frequency analysis process employed in this investigation only retains the stable orbits in the period-3 and period-5 island chains for $k = -0.1$. Thus, the process only captures stable islands for period-q island chains with an odd value of q. In contrast to the CR3BP, each of these families exhibits a change in the location of the stable and unstable period-q orbits within the corresponding island chain. This observation is illustrated by the period-5 island chains in the Poincaré maps plotted in Figure 6.13 for (a) the CR3BP and (b) the MCR3BP with $k = -0.1$. For even values of q, however, the change in the stability of the orbits in a period-q island chain results in the frequency analysis process retaining only the two crossings of the unstable orbit. To analyze the corresponding stable orbits within the island chain, an alternative approach for representing the frequency decomposition of orbits within an island is appropriate for further investigation of the influence of a three-body potential term.

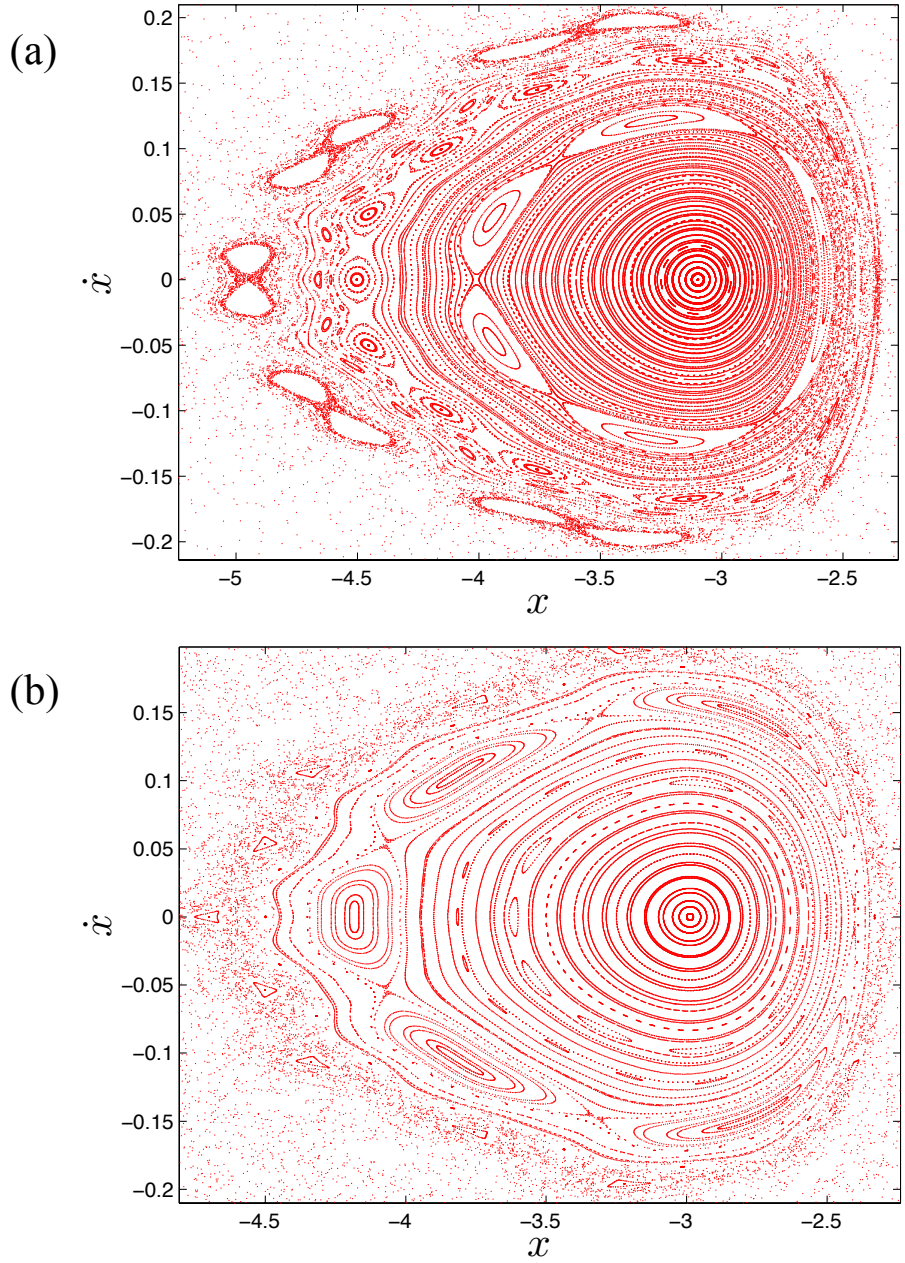

Figure 6.13. Poincaré maps depicting period-5 island chains in the MCR3P for (a) $k = 0.0$ and (b) $k = -0.1$.

7. SUMMARY AND RECOMMENDATIONS

7.1 Summary

Augmenting the pairwise gravitational potential in the CR3BP with a three-body interaction, scaled by the coefficient k, impacts the stable solutions available to a particle orbiting in the exterior region. The influence of this additional interaction on the dynamical structures in the MCR3BP, for a mass ratio of $\mu = 0.3$, is explored using techniques developed within the context of both dynamical systems theory and frequency analysis.

Investigation of particular solutions in the form of equilibrium points and zero velocity curves reveals a change in the bounds on the motion of P_3. Modeling the MCR3BP with a positive three-body coefficient, k, the size of the regions of allowable motion differs from the bounded regions in the CR3BP. For a large negative coefficient, however, the zero velocity curves can exhibit significantly different features as the L_i gateways open in a different order for $i = 1, 2, 3$. This change in the shape of the zero velocity curves may impact the orbits available in the MCR3BP.

Poincaré maps and frequency decomposition are used to locate and represent the periodic and quasi-periodic orbits that form the underlying structure of the dynamical environment in the augmented model. Over a specified interval of values for the three-body potential coefficient, the period-q orbits present in the CR3BP are also available in the MCR3BP. The value of the three-body potential coefficient affects the energy levels at which these orbit families are accessible. In addition, the three-body interaction affects the size of the stable regions within the phase space. For sufficiently large values of k, period-multiplying bifurcations occur along families of period-q orbits, as apparent in the frequency representations and confirmed using Poincaré maps. Selecting a large negative value of k, however, impacts the location of

stable and unstable orbits within a period-q island chain, suggesting a change in the formation of the two period-q orbit families. These changes in the dynamical environment suggest that the three-body interaction influences the underlying structure of the MCR3BP with an effect that may not be reproducible by appropriate selection of the energy constant in the CR3BP; qualification of such a hypothesis, however, requires further investigation.

7.2 Recommendations

Extending this analysis may yield additional insight into the motion of a small companion about a binary system, with a large mass ratio, under the influence of a three-body interaction. Recommendations for extending this investigation include:

- Frequency analysis of the dynamics in the CR3BP for mass ratios not equal to $\mu = 0.3$ may aid in separating the effects of the three-body interaction from those caused by varying natural parameters.

- Analyzing orbits that are located closer to the primaries may amplify the effects of the three-body interaction. This expansion of the subset of studied orbits may reveal structures that are not available in the CR3BP.

- The subset of orbits that are decomposed into their fundamental frequencies may be extended to include those that do not perpendicularly cross the $y = 0$ surface of section at any time. Accordingly, further development of the representations of these frequencies is required.

- The range of three-body potential coefficients that are studied may be expanded to incorporate those which result in more significant changes to the dynamical environment in the vicinity of the binary.

- The two primaries comprising the binary may be modeled to follow elliptical orbits. Subsequently, a new model may be derived by augmenting the potential

function in the elliptic restricted three-body problem with a three-body interaction that incorporates a time-varying distance between the two primaries.

Investigating these new aspects of the problem and developing additional computational techniques will aid in further exploring the influence of a three-body interaction. Such additional analysis may result in the identification of a characteristic signature of three-body gravitational interactions that may be observable in the timing measurements of the pulse emitted from the pulsar.

LIST OF REFERENCES

LIST OF REFERENCES

[1] E. Fischbach,"Long-Range Forces and Neutrino Mass", *Annals of Physics*, vol. 247, pp. 213-291, 1996.

[2] R. D. Mattuck, *A Guide to Feynman Diagrams in the Many-Body Problem: Second Edition*. New York: Dover Publications, Inc., 1976.

[3] S. Braibant, G. Giacomelli, M. Spurio, *Particles and Fundamental Interactions: An Introduction to Particle Physics*. Springer, 2012.

[4] P. Maris, J.P. Vary, P. Navratil, W. E. Ormand, H. Nam, D. J. Dean, "Origin of the anomalous long lifetime of C^{14}", *Physical Review Letters*, vol. 106, issue 20, 2011.

[5] J. Barrow-Green, *Poincaré and the Three Body Problem, History of Mathematics Vol. 11*. American Mathematical Society, 1997.

[6] V. Szebehely, *Theory of Orbits: The Restricted Problem of Three Bodies*. London, UK: Academic Press, 1967.

[7] G. W. Hill, "Researches into the lunar theory," *American Journal of Mathematics*, vol. 1, no. 1, pp. 5-26, 1878.

[8] J. H. Poincaré, *Les Méthodes Nouvelles de la Mécanique Céleste*, vol. 1-3. Gauthier-Villars et fils, 1899.

[9] A. N. Kolmogorov,"On Conservation of Conditionally Periodic Motions for a Small Change in Hamilton's Function", *Dokl. Akad. Nauk SSSR (N.S.)*, vol. 98, pp. 527-530, 1954

[10] V. I. Arnol'd, "Proof of a Theorem of A. N. Kolmogorov on the Preservation of Conditionally Periodic Motions under a Small Perturbation of the Hamiltonian", *Uspekhi Matematicheskikh Nauk*, vol. 18, pp. 13-40, 1963.

[11] J. Moser, "On Invariant Curves of Area-Preserving Mappings of an Annulus", *Nachrichten der Akademie der Wissenschaften zu Gttingen. II. Mathematisch-Physikalische Klasse*, 1-20, 1962.

[12] R. Ramirez, *The FFT, Fundamentals and Concepts*. Englewood Cliffs, New Jersey: Prentice Hall, 1985.

[13] J. W. Cooley, J. W. Tukey, "An algorithm for the machine calculation of complex Fourier series", Mathematics of Computation, vol. 19, no. 90, pp. 297301, 1965.

[14] J. Laskar, "Frequency Map Analysis of an Hamiltonian System", *American Institute of Physics Conference Proceedings*, 1995.

[15] M. Valluri, D. Merritt, "Regular and Chaotic Dynamics in Triaxial Stellar Systems", *The Astrophysical Journal*, vol. 506, no. 2, pp. 686-711, 1998.

[16] Y. Papaphillippou, J. Laskar, "Global dynamics of triaxial galactic models through frequency map analysis", *Astronomy and Astrophysics*, vol. 329, pp. 451-481, 1998.

[17] D. Merritt, "Non-integrable Galactic Dynamics" *Scottish Universities Summer School in Physics and Institute of Physics Publishing*, Bristol, UK, 2001

[18] E. B. Ford, K. J. Joshi, F. A. Rasio, B. Zbarsky, "Theoretical Implications of the PSR B1620-26 Triple System and its Planet", *Astrophysical Journal*, Vol. 528, pp. 336-350, 2000.

[19] M. H. van Kerkwijk, C. G. Bassa, B. A. Jacoby, P. G. Jonker, "Optical Studies of Companions to Millisecond Pulsars", *Astronomical Society of the Pacific Conference Series*, Vol. 328, pp. 357-369, 2005.

[20] T.S. Parker, L.O Chua, *Practical Numerical Algorithms for Chaotic Systems*. New York: Springer-Verlag, 1989.

[21] G. Contopoulos, *Order and Chaos in Dynamical Astronomy*. Germany: Springer-Verlag, 2002.

[22] L. Perko, *Differential Equations and Dynamical Systems*. Third Edition, New York: Springer, 2000.

[23] G. Gomez, J. M. Mondelo, C. Simo, "Refined Fourier Analysis: Procedures, Error Estimates and Applications", Preprint, 2001.

[24] W. S. Koon, M. W. Lo, J. E. Marsden, S. D. Ross, *Dynamical Systems, the Three Body Problem and Space Mission Design*. 2006.

[25] R. H. Abraham, C. D. Shaw, *Dynamics - The Geometry of Behavior. Part Two: Chaotic Behavior* Santa Cruz, CA: Fourth Edition, Aerial Press, 1990.

[26] R. Seydel, *Practical Bifurcation and Stability Analysis: From Equilibrium to Chaos*. New York: Springer-Verlag, 1994.

[27] E. Campbell, "Bifurcations from Families of Periodic Solutions in the Circular Restricted Problem with Application to Trajectory Design", Ph.D. Dissertation, School of Aeronautics and Astronautics, Purdue University, West Lafayette, Indiana, August 1999.

[28] W. Press, S. Teukolsky, W. Vetterling, B. Flannery, *Numerical Recipes: The Art of Scientific Computing*, Third Edition, New York: Cambridge University Press, 2007.

[29] B. Bradie, *A Friendly Introduction to Numerical Analysis*, Pearson Prentice Hall, 2006.

[30] T. A. Pavlak, "Mission Design Applications in the Earth-Moon System: Transfer Trajectories and Stationkeeping", M.S. Thesis, School of Aeronautics and Astronautics, Purdue University, West Lafayette, Indiana, May 2010.

[31] A. Jorba, "A Methodology for the Numerical Computation of Normal Forms, Centre Manifolds and First Integrals of Hamiltonian Systems", *Experimental Mathematics*, vol. 8, pp. 155-195, 1999.

[32] A. Oppenheim, A. Willsky, S. Nawab, *Signals and Systems: Second Edition*. Upper Saddle River, New Jersey: Prentice Hall, 1997.